Multimodal Neuroimaging with Simultaneous Electroencephalogram and High-Field Functional Magnetic Resonance Imaging

by

Patrick L. Purdon

S.M., Electrical Engineering and Computer Science
Massachusetts Institute of Technology, 1998

A.B., Engineering Sciences
Harvard College, 1996

SUBMITTED TO THE HARVARD-MIT DIVISION OF HEALTH SCIENCES AND TECHNOLOGY IN PARTIAL FULFILLMENT OF THE REQUIREMENTS OF THE DEGREE OF

DOCTOR OF PHILOSOPHY IN BIOMEDICAL ENGINEERING
AT THE
MASSACHUSETTS INSTITUTE OF TECHNOLOGY

JUNE 2005

Signature of Author: _____
Harvard-MIT Division of Health Sciences and Technology
May 16, 2005

Certified by: _____
Emery N. Brown, M.D., Ph.D.
Associate Professor, Anesthesia and Health Sciences and Technology
Massachusetts General Hospital, Harvard Medical School
Thesis Supervisor

Accepted by: _____
Martha L. Gray, Ph.D.
Edward Hood Taplin Professor of Medical and Electrical Engineering
Director, Harvard-MIT Division of Health Sciences and Technology

Multimodal Neuroimaging with Simultaneous Electroencephalogram and High-Field Functional Magnetic Resonance Imaging

by

Patrick L. Purdon

Submitted to the Harvard-M.I.T. Division of Health Sciences and Technology on May 16, 2005 in partial fulfillment of the requirements for the degree of Doctor of Philosophy in Biomedical Engineering

Abstract

Simultaneous recording of electroencephalogram (EEG) and functional magnetic resonance imaging (fMRI) is an important emerging tool in functional neuroimaging with the potential to reveal new mechanisms for brain function by combining the high spatial resolution of fMRI with the high temporal resolution of EEG. Applications for this technique include studies of sleep, epilepsy, and anesthesia, as well as basic sensory, perceptual, and cognitive processes. Unlike methods that combine these modalities from separate recordings, simultaneous recordings can reveal temporal correlations between EEG and fMRI. Simultaneous recordings also eliminate environmental confounds inherent with separate recordings. MRI systems produce electromagnetic interference that can corrupt sensitive electrophysiological recordings, making simultaneous recordings challenging. Gradient switching and RF pulses can saturate EEG amplifiers, and cardiac pulsation within the static magnetic field produces large artifact signals ("ballistocardiogram") that confound EEG analysis.

In this Ph.D. thesis, we develop an EEG acquisition system compatible with fMRI at 3 and 7 Tesla, a method for eliminating the ballistocardiogram artifact using adaptive filtering, and use these methods to study the 40-Hz auditory steady-state response (ASSR). The adaptive filtering method outperforms existing standard methods by up to 600%. The ASSR is a sub-microvolt level auditory evoked potential related to sleep, consciousness, and anesthesia. Simultaneous recordings of ASSR and fMRI reveal that spontaneous fluctuations in the amplitude of the ASSR are represented throughout the auditory system, from cortex to brainstem, suggesting that brainstem structures play an important role in generating the 40-Hz ASSR and that integration of sensory information across multiple hierarchical scales, including the earliest portions of the central nervous system, may constitute an important component of awareness or arousal.

Thesis Supervisor:
Emery N. Brown, M.D., Ph.D.
Associate Professor, Anesthesia and Health Sciences and Technology, MGH/HMS

Acknowledgments

Throughout my graduate studies I have had the privilege of working with the most outstanding mentors and role models that any student could ask for. First and foremost is my thesis advisor, Emery Brown, from whom I have learned so much. His deep expertise in statistics, signal processing, and physiological modeling has been an inspiration. I have benefited tremendously from the rich intellectual environment that he has fostered within the lab. His thoughtful, even-tempered leadership style, and his work ethic and resolve in times of adversity have set a great example for me to follow. I am grateful for the confidence he has shown in my abilities, allowing me to take on many diverse responsibilities within our research program with the freedom to make decisions and take initiative on my own. This responsibility and freedom has no doubt contributed to my rapid maturation as an investigator. Whenever I have needed anything, be it words of wisdom or resources to complete an objective, Emery has always been there. Giorgio Bonmassar has been my other great teacher. Giorgio's energy and enthusiasm are infectious and his expertise in electronics and system design have greatly enriched my graduate education. During the chaos of an experiment, there is no one I know who is better at debugging. From Giorgio I have learned the tenacity necessary to succeed as a scientist. Robert Weisskoff and Victor Solo have made a tremendous impact on my intellectual development. I initially joined the Martinos Center (then the MGH-NMR Center) to work with Robert on fMRI signal processing. Robert's knowledge and skill spanned many disciplines from imaging physics to physiology, and set a high standard for me to follow early in my graduate career. Victor Solo's depth of knowledge in signal processing, statistics, and control theory is unique in the world and it has been a privilege to learn from him. The guidance of my thesis committee members Jennifer Melcher, Steve Massaquoi, and Bruce Rosen has helped tremendously to refine the direction of this research, particularly in the initial stages when were just beginning to formulate hypotheses on anesthetic mechanisms.

The data presented in this thesis are the result of a team effort from investigators spanning several research groups within the MGH-HST Martinos Center, and I am grateful to them for their time, energy, and insight. Giorgio Bonmassar, Leonardo Angelone, Sunao Iwaki, Chris Vasios, and Jyrki Ahvenien represent the core EEG-fMRI team that spent countless early-morning and weekend hours working together to help run these studies, particularly those at 7 T (Tough guys!:). Iiro Jaaskelainen provided important advice in the initial design of the auditory EEG-fMRI paradigm. I appreciate the experience and perspective on hardware development provided by Hernan Millan

towards the end of this process. I would also like to thank Jack Belliveau for helping to assemble the fantastic cast of characters mentioned above.

The auditory studies presented here were inspired by outstanding research conducted by Mike Harms and Jennifer Melcher on the time course of auditory fMRI responses. I am greatly indebted to them for their excellent work and guidance in establishing my own protocols. I thank Irina Sigalovsky and Tom Talavage for their guidance in these matters as well.

I am very grateful to Larry Wald, Chris Wiggins, and Graham Wiggins for their help in establishing the 7 T imaging studies, and for granting us unparalleled access to the 3 and 7 T imaging facilities at the Martinos Center. Mary Foley and Lawrence White also deserve special thanks for their helpful nature and for the countless times they have rescued us when MRI system has gone awry.

While it is not obvious from inspection, the intellectual inspiration for this research has been to understand the neural mechanisms for loss of consciousness under anesthesia. I am grateful for the effort and generosity of our amazing anesthesia research team, consisting of Catherine Mullaly, John Walsh, Grace Harrell, Jean Kwo, and Margaret Barlow. For many years now, we have worked together to establish a research paradigm for studying anesthesia using functional imaging, and are ever closer to completing this monumental goal. I would also like to thank Warren Zapol, Chair of the Department of Anesthesia and Critical Care at the Massachusetts General Hospital, for his ardent support of these research efforts since their inception.

I would like to thank Randy Gollub, Steve Stufflebeam, and Betsy Tarlin for their help in securing funding for these studies. Your time and effort, and the confidence you have shown in me are greatly appreciated. I would also like to thank Allan and Luanne Reed for their generous contributions to this research effort.

The administrative staff of the Martinos Center, especially Dee Dee Corriea and Janice White, have been great to work with.

I have been fortunate to make many friends during my studies and I would like to thank them for all the good times we have shared together. Steve Nagle and Vitaly Napadow have been my go-to-guys all through grad school. Without them who knows what kind of trouble I would have gotten myself into (or missed out on)? And how fun would it have been if 13 Valentine Street had lasted more than a month (shout out to Judy Faberman! :)? Aaron Moment is a great friend who encouraged my early musical development as a jazz vocalist, and I'm indebted to him for fostering that very cool component of my life. Alex Barnett and John Capello have been fantastic musical collaborators and good friends, forming the core of my most recent band. Your musical excellence and adventurous spirit are much appreciated; Too bad we all had to go and get "real" jobs and lives. Vitaly, Alex, Diana Baquero, Liz Canner, Phil Steigman, Mason Sand, Reuven Singer, Gretchen Iversen, John Iversen and Tara Ahmed were part of a crew of Bohemian misfits residing in and around 23a Howard Street that formed a vibrant

part of my social life. One day we will write a play or book or song about those times, complete with bunny rabbit ears. The crew of circa-1996/7 Ashdown House and EECS will be remembered, always: Eric Stuckey, Mike Gordon, Evan Chen, Erik Deutsch, Ritwik Chatterjee, Michael Qin, Sham Sokka, Kinu Masaki, Ankur Garg. Did we really used to say "@#$!%-Yo" at the start of every sentence? Can I ride around in an "A-Team" van for my bachelor's party too? As Ritwik used to say, "Good times, good times..." :) Cameron Foley and Keith Foley have been wonderful friends for so many years. Your North End pad was always a fun place to hide-out, and Cameron, you always knew exactly when to call to say "Hello!" Without my salsa dancing buddies, I might never have left the house, thanks so much for your energy and enthusiasm: Mark Finlayson, Ayse Guler, Tracey Mellor, Tracie Robinson, Morgan Stockmayer, Maurice Maclau. Claire Salomon, I must hear you sing, and you must teach me what you know! :). Olya Veselova, your energy, warmth, intelligence, beauty, and charisma will always make me smile; I will never forget the great times we spent together :). The crew of the Brown Lab has made work a wonderful place to show up every day: Uri Eden, Mike Prerau, Sam Mukherji, Ram Srinivasan, Julie Scott, Loren Frank, David Nguyen, Chris Long, Supratim Saha, Ricardo Barbieri, Anne Smith, Murat Okatan, Catherine Mullaly, James Williams, Yumi Ishizawa, Brenda Marshall, Tyler Gibson, Camilo Lamus, Danielle Dray, Esosa Omanoba, Neil Desai. Uri, you now inherit all of my Red Bull and Doubleshot-expresso drinks, as well as all the remaining granola bars, and we will continue to run fly-routes, end-zone fades, and boot-leg options until you finish your thesis. Mike, I believe we are due for a road trip :). Sam, we're headed to Newport in August. Ram, you are my wingman after you finish boards. Julie, where would our lab be without you to look out for us (Go Sox!)? Chris, thank you for your encouragement all throughout this process. Supra, thank you for the astrological reports indicating that April and May 2005 would be "a very productive time." To my friends at the MGH Martinos Center, thank you for making it a wonderful place to work and learn: Leonardo Angelone, Chris Vasios, Jyrki Ahveninen, Sunao Iwaki, Dave Tuch, Tamara Knutsen, Steve Stufflebeam, Fa-Hsuan Lin. Dave, had I not run into you in E-25 in spring of 1999 to learn of Christof Koch's BCS colloquium presentation, I might never have discovered my thesis topic. Thank you to my HST-MEMP classmates, you guys are the best: Thomas Heldt, Nina Menezes, Mark Price, Sham Sokka, Chris Hartemink, Ngon Dao. Tommy-boy, what's for dinner? RIBS! Mark Price, thank you for lobbying with Emery in the OR to let me graduate. :)

To Leo Castro, Jason Norton, Wes Hawk and Chang Lee, my boys from Chula Vista: You have been my best friends since high school and I thank you for all your support over the years. Finally, I have enough experience points to become a Level-20 Magic User. Hopefully one of us will be inducted into the Chula Vista High School Hall of Fame before Donnie Edwards is. I look forward to singing at all your weddings, please start rehearsing now so you can sing at mine.

Finally, and most importantly, I would like to thank my wonderful loving family for their support through these many challenging years of study filled with both hardship and triumph. With her energy, insight, and enthusiasm, my little sister Alfreda Mei Purdon has been a constant source of inspiration and support and I am grateful and

thrilled that we have been able to spend the last several years living together in the same city. From my earliest years in grade school, my mother, Morna Purdon, and my father, Charles Purdon, encouraged me to pursue my dream of being a scientist, investing time and energy without limit to help make that dream a reality. Who knew that the countless hours of building model rockets and entering science fairs would lead to all this? In the most difficult moments of this thesis work, the lessons learned at 1264 Dixon Way made the biggest difference. I dedicate this work, and everything that follows from it, to my mother, my father, and my sister.

Patrick L. Purdon
May 16, 2005

Support

These studies have been supported by the generous contributions of the Whitaker Foundation for Biomedical Engineering, the Allan and Luanne Reed Scholarship in Health Sciences and Technology, the National Institutes of Health Neuroimaging Training Program, a grant from the National Institute for Biomedical Imaging and Bioengineering (R01 EB00522), and a grant from the National Center for Research Resources (P41 RR14075).

Table of Contents

Chapter 3: Design and Implementation of Hardware and Software Systems for EEG-fMRI

Chapter 5: Simultaneous EEG-fMRI of the 40-Hz Auditory Steady State Response at 3 and 7 Tesla

Chapter 6: Conclusions and Directions for Future Research

Chapter 1
Introduction

1.1. Multimodal Functional Neuroimaging

The search for noninvasive methods for visualizing brain dynamics has fueled the imagination of scientists, physicians, and engineers ever since the first recording of human electroencephalogram in the early 20^{th} century. Much of what is currently known in neuroscience comes from ex-vivo anatomy and lesion studies. However, questions relating to the mechanisms for consciousness, cognition, memory, and emotion require that we observe neural dynamics as they unfold in living beings in both normal and disease states. For the vast majority of human research, this implies that studies must be done non-invasively, particularly if the goal is to produce methods with future clinical diagnostic utility.

The noninvasive imaging techniques available to neuroscientists today span a broad range of spatio-temporal scaless and biophysical coupling mechanisms, as depicted in **Figure 1.1** (adapted from (Nunez, 1995b)). Nuclear medicine techniques such as positron emission tomography (PET) and single photon emission computed tomography

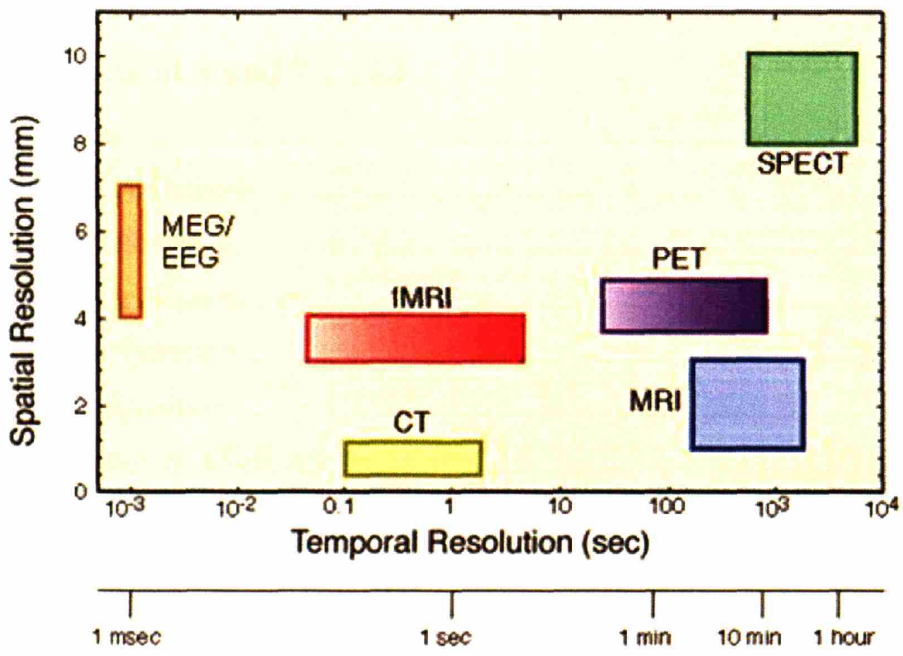

Figure 1. 1. Spatio-temporal characteristics of different imaging techniques.

(SPECT) provide spatial resolution in the centimeter range and temporal resolution ranging from minutes to 10's of minutes, but can also provide metabolic specificity with appropriate choice of radiopharmaceutical (Bronzino, 1999). Functional magnetic resonance imaging (fMRI) provides spatial resolution down to the millimeter range, but its temporal resolution is limited by the dynamics of the neurovascular response, which is capable of following changes in neural activity on the order of seconds (Buxton, 2001;Nunez and Silberstein, 2000). Electroencephalography (EEG) and magnetoencephalography (MEG) offer temporal resolution in the millisecond to 10's of milliseconds range, but solutions to the ill-conditioned current-source localization problem are accurate only to the centimeter range, and may be strongly biased towards the cortex due to the distance scaling relationship of the magnetic and electric lead fields describing volume conduction within the brain (Hamalainen et al., 2005). Optical brain

imaging methods pose an ill-conditioned inverse problem similar to that of EEG or MEG, and are observed through neurovascular coupling like fMRI, but are able to separately quantify levels of oxy- and deoxy-hemoglobin, and thus offer the potential for much higher temporal resolution by observing small perturbations in hemoglobin prior to onset of the slower neurovascular response (Franceschini and Boas, 2004;Culver et al., 2003).

With this vast assortment of imaging tools, a natural thought is to combine information from different imaging modalities to improve upon the information provided by any single imaging modality alone. Co-registration of functional information from lower resolution PET or fMRI images to higher resolution anatomic MRI, either to a standard reference brain (Talairach and Tourneau, 1988), or within and across subjects (Fischl et al., 1999;Jenkinson and Smith, 2001), represents the most basic form of multimodal integration, and allows for precise localization of functional activity to specific brain regions. Anatomic and functional MRI have also been used as a constraint for the ill-conditioned EEG and MEG source localization problem, first as a constraint on the tissue layer (cortex) and orientation of sources based on cortical surface reconstructions from high-resolution anatomic MRI (Dale and Sereno, 1993), and then later as a position constraint phrased in terms of a Bayesian prior distribution formed from functional MRI activation maps (Liu et al., 1998), constituting a co-registration of anatomic, functional MRI, and electrophysiological information. Investigators have also adopted simpler forms of co-registration of EEG/MEG with functional MRI, where single or multiple dipoles are seeded in locations corresponding to fMRI response peaks, and fitted for strength and orientation (e.g., (Vanni et al., 2004a;Vanni et al., 2004b)). Anisotropy of brain tissue conductivity has also been incorporated into the forward model

for EEG and MEG, and has been shown to improve source strength estimation for single dipole models (Haueisen et al., 2002).

1.2. Biophysical Constraints of Multimodal Integration of EEG, MEG, and fMRI

While the intuition behind co-registration of functional MRI and EEG/MEG solutions is very appealing— i.e., that these disparate imaging modalities are somehow measuring "the same thing"— a closer examination of the biophysical mechanisms for generating each imaging modality reveals a more complicated situation. EEG and MEG signals are believed to come from post-synaptic potentials and currents (Hamalainen et al., 2005). They are heavily influenced by the geometry of local neural cyto-architecture, favoring highly parallelized current sources, such as pyramidal layer of the cortex, over "closed-field" cells and structures, such as radially-symmetric stellate cells, which are thought to generate minimal extra-cellular currents outside their immediate vicinity (Hamalainen et al., 2005). Meanwhile, the blood-oxygen level dependent (BOLD) contrast mechanism used in functional MRI relies upon the neurovascular response to task-related changes in oxygen consumption and metabolic demand. Temporally-varying image contrast is produced by flow-induced washout of paramagnetic deoxyhemoglobin, which increases T2* and results in a brighter MRI signal (Kwong et al., 1992;Ogawa et al., 1992;Ogawa et al., 1990).

Table 1.1 provides a comparison of many of the differences in the physiological coupling mechanisms for EEG/MEG vs. fMRI. Based on these differences, Nunez and

Silberstein (Nunez and Silberstein, 2000) suggested a number of cases where one imaging modality could produce a large signal, while the other might not:

1. The physics of current dipoles render certain source configurations difficult to observe with MEG or EEG: The Green's functions describing the electro- and bio-magnetic forward problems scale as $1/R^2$, where R is the distance from the current dipole, attenuating signals from deep sources. Source detection is also sensitive to dipole orientation: MEG is less sensitive to radial dipoles and more sensitive to tangential dipoles, while synchronized tangential dipoles on neighboring faces of a sulcus can have a self-canceling effect for both MEG and EEG (Nunez, 1995b). Brain structures and cells whose shape or cyto-architecture resemble "closed fields" (e.g., the cylindrically-shaped hippocampus, or the radially-symmetric stellate cell) are thought to generate negligible scalp signals. Meanwhile, in all these cases the metabolic response producing the BOLD fMRI signal could be quite large, resulting in a discrepancy: small EEG/MEG signals, but large fMRI responses.
2. Frequency Response: The frequency response of EEG/MEG allows for millisecond resolution observations, while the fMRI BOLD response evolves at frequencies below ~1 Hz. It is believed that brief neural events observable by EEG and MEG may not elicit a measurable hemodynamic or metabolic signature. In such cases one could observe large EEG/MEG signals, but small fMRI signals.
3. Oscillatory EEG/MEG dynamics (LARGE EEG/MEG, small fMRI): Oscillatory EEG/MEG dynamics (such as the alpha-rhythm) are thought to

rely upon neural synchrony over a broad expanse of cortex several square centimeters in size, made possible by cortico-cortico connections. Because of synchrony, the number density of neurons required to generate a measurable signal can be small, resulting in small changes in metabolic demand and a small fMRI signal. Here again, one might observe large EEG/MEG signals, but small fMRI responses.

To this list of biophysical ambiguities, we add two conceptual problems:

4. Inhibition versus Excitation: EEG and MEG are generated primarily by post-synaptic potentials (Hamalainen et al., 2005), so in principle the concepts of excitation and inhibition are still interpretable as positive or negative potentials, if only in the context of a net potential averaged over a large portion of tissue. But the changes in metabolism detected by fMRI have an ambiguous interpretation, as both excitation and inhibition are energetically active processes, so predominantly excitatory or inhibitory processes can both result in an increased BOLD signal, with the reverse being true for processes that elicit a decrease in either excitation or inhibition or both.
5. *Current* sources versus *Dynamical* sources: The biophysics problem of EEG/MEG source localization is concerned with identifying electrical *current* sources that produce observed scalp electric or magnetic fields. However, considering the multiple mechanisms for "missing sources" (point 2), even if all "visible" current sources are correctly estimated, there may be numerous *dynamical* components of the overall neural system that are hidden from view, some of which may be critical to the physiology under investigation.

Depending on the experiment in question, this may also be a concern for fMRI as well, given its signal-to-noise ratio and frequency response.

Modality	EEG/MEG	fMRI
Frequency response	• 0 to 100 Hz	• 0 to 1 Hz
"Hidden" sources	• "Closed field" structures (stellate cells, hippo-campus) • Sensitivity to tangential versus radial dipole orientation • Distance-scaling of Green's functions ($\sim 1/R^2$) diminish visibility of deep sources	• Susceptibility artifact near air-tissue boundaries • Masking by large-vein signals • Cardio-respiratory pulsation, particularly of brainstem structures
Exitation vs. Inhibition	• Generated primarily by post-synaptic potentials, in principle can distinguish between excitation and inhibition in volume-averaged sense	• Ambiguity: Increases in metabolic demand can manifest from increased excitation or increased inhibition, and vice-versa
SNR	• Dependent on the number density of synchronous neurons involved in process • N~O(100-1000) observations for event-related designs	• Field-strength and coil dependent; e.g., 2% signal changes at 1.5 Tesla, up to 10% at 7 Tesla, potentially higher with phased array systems • N~O(10-100) observations for event-related designs

Table 1.1: A Comparison of Coupling Mechanisms for EEG/MEG vs. fMRI

These concerns paint a fairly pessimistic picture of the conceptual validity of multi-modal integration or co-registration methods for MEG/EEG and fMRI, as there may not be much overlap in the neural processes that are observable by these techniques.

The best of the currently available methods attempt to represent these ambiguities in terms of prior distributions on spatial locations either showing or not showing activation from fMRI (Liu et al., 2002), but thus far do not directly engage the underlying conceptual problems outlined above. In the sections that follow, we review recent experimental evidence clarifying these concerns, illustrating that there is considerable overlap in the types of processes that can be observed in both MEG/EEG and fMRI. We then introduce a conceptual framework for multi-modal integration that treats the multiple imaging modalities as separate observations of an underlying common dynamical system. We make the case for simultaneous recording of EEG and fMRI as an important tool for carrying out this framework in neuroscience studies, and outline experimental design issues and technical priorities towards realizing this objective.

1.3. Deep Sources, Source Orientation, Closed Fields, and fMRI Frequency Response

As discussed in Section 1, it is generally believed that deep sources cannot be localized with EEG or MEG, however theoretical calculations by Lutkenhoner suggest that deep sources can in fact be localized, though with lower precision (Lutkenhoner, 1996). A study of EEG and MEG dipole localization in a realistic head phantom by Leahy and colleagues provided empirical evidence of this, demonstrating that deep orbito-frontal and frontal-temporal sources could still be localized to within 20 mm using EEG combined with a three-layer boundary element model (Leahy et al., 1998). While MEG is less sensitive to radially-oriented sources, the degree of error this poses for physiologically-realistic sources that span as little as a square centimeter or so appears to

be limited: A recent computational study by Hillebrand, using realistic head models with cortical surface reconstructions, showed that areas of cortex with poor resolvability due to radial orientation were limited to ~2 mm strips on the crests of gyri, and were flanked on either side by areas of high resolvability due to nominal tangential components and close proximity to the scalp surface (Hillebrand and Barnes, 2002). The concern that "closed-field" structures may be electromagnetically-invisible, while theoretically well-motivated, is difficult to address experimentally. We note, however, that no structures in the brain precisely obey the geometric constraints of a closed-field, and it is certainly possible that slight deviations from the ideal geometry could result in detectable signals. Furthermore, since neurons are highly interconnected, closed-field cells such as the stellate cell would likely be connected to other cell types in the nearby vicinity capable of generating an external field. Overall, these studies and observations illustrate that the geometrical constraints on sources, while important, do not preclude source localization and analysis (addressing concern 1 from Section 2).

The fact that the fMRI BOLD response is limited to less than ~1 Hz does not imply that stimuli presented or neural events occurring at a faster rate cannot be detected. For instance, a study by Burock, et al., showed that randomized event-related designs featuring inter-stimulus intervals as short as 500 milliseconds could be resolved using functional MRI (Burock et al., 1998). More recently, temporal correlations have been found between the BOLD signal and EEG alpha and beta rhythms from simultaneously recorded EEG and fMRI (Goldman et al., 2002;Laufs et al., 2003b;Laufs et al., 2003a), between BOLD and LFPs (Logothetis et al., 2001), and between optically-measured hemoglobin changes and both LFPs and MUA (Devor et al., 2003). These studies, to be

discussed in greater detail below, demonstrate that, despite its slow frequency response, changes in the BOLD signal can in fact be related to electrophysiological signals (addressing concern 2 from Section 2).

1.4. Oscillatory EEG dynamics and fMRI: Fluctuations in Alpha and Beta-2 Power are Temporally Correlated with BOLD fMRI in Distributed Cortical Networks

The alpha rhythm is an oscillatory rhythm observable in both EEG and MEG with a frequency range between 8 and 13 Hz (Nunez, 1995a). It is most readily observed in awake resting subjects with eyes closed, and disappears in the early stages of sleep. Given the slow frequency response of BOLD fMRI, one would not expect to see a relationship between the alpha rhythm and fMRI, but recent investigators have observed a temporal correlation between BOLD fMRI and alpha rhythms recorded from simultaneous EEG (Goldman et al., 2002;Laufs et al., 2003b;Laufs et al., 2003a). Goldman and colleagues recorded EEG interleaved with fMRI in awake subjects with eyes closed, estimated the alpha power from each interleaved EEG segment, and related the temporal fluctuations in alpha power to the fMRI BOLD signal by voxel-wise correlation (Goldman et al., 2002). This temporal correlation is possible because, apparently, the natural temporal modulation in alpha power is slow and within the frequency response of the fMRI BOLD response. A negative correlation was found between the BOLD signal and alpha power fluctuations (i.e., BOLD signal goes down as alpha power goes up) in several areas, including bilateral occipital, superior temporal, and inferior frontal cortices, as well as anterior cingulate gyrus. A positive correlation

between BOLD and alpha power was found in the thalamus and insula. A similar study by Laufs (Laufs et al., 2003a)used both interleaved and continuous EEG recordings during fMRI (with EPI artifact subtraction (Allen et al., 2000)) to correlate alpha power with the BOLD signal, and found negative correlations in large bilateral sections of parietal and frontal cortex. Positive correlations in this study were less consistent, and did not include the thalamus. A later study by Laufs (Laufs et al., 2003b)used a similar analysis on both alpha and beta-2 (17-23 Hz) power, revealing a positive correlation between beta-2 power and BOLD in posterior cingulate and adjacent precuneus, as well as the temporo-parietal junction and dorsomedial prefrontal cortex. Furthermore, significant cross-correlation between BOLD time-courses within these regions were noted, suggesting that previously studied resting-state spatiotemporal correlations are related to electrophysiological oscillations in alpha and beta-2 (Lowe et al., 1998;Biswal et al., 1995;Greicius et al., 2003).

A consistent theme in these studies is that increases in alpha power correspond to decreases in BOLD signal throughout distributed cortical networks spanning the occipital, parietal, and frontal regions. There are differences in the regions revealed by these two studies, however: Occipital activity was not identified in the Laufs paper, while parietal activity was absent in the work by Goldman. Furthermore, thalamic activity was noted by Goldman and colleagues, but not by Laufs. Some of these discrepancies may be related to differences in EEG/fMRI acquisition and processing methods. In Goldman's work, EEG was interleaved with fMRI in a slice-wise fashion, rather than with clustered volumes: Each six-slice volume was acquired over a 2.5-second TR, requiring 90-milliseconds acquisition time for each slice, with slice

acquisitions spread uniformly over the 2.5-second TR. This interleaving scheme introduces a slice-dependent time-delay between each alpha power estimate and the observed BOLD response, which was not accounted for in the analysis, and could explain some of the brain regions missing from this study but present in Laufs. In both Laufs papers fMRI were acquired at 1.5 Tesla field strength, compared to 3 Tesla in the Goldman paper, which could have an impact since the signal-to-noise of the BOLD response is generally smaller at 1.5 T compared to 3 T. Furthermore, the pulse artifact and EPI artifact correction algorithms used in the Laufs papers could have influenced the estimated alpha power. These discrepancies highlight the need for improved acquisition methods, artifact removal, and the need to operate at higher field strengths to increase BOLD SNR.

Setting aside these methodological differences, Goldman points out that there are three possible interpretations for the observed correlation between BOLD and EEG oscillatory power (Goldman et al., 2002): 1) The identified brain regions represent the current sources responsible for the scalp potentials, 2) The identified regions represent part of the dynamical system generating the observed rhythms, but are not among the current sources responsible for the scalp potentials, or 3) The identified brain regions are correlated to the observed oscillatory signal, but not causally related (for instance, since alpha fluctuations are related to drowsiness, brain regions involved in drowsiness might show correlation, even if they do not generate the alpha rhythm dynamically or electrically). These interpretations apply equally well to the work by Laufs due to the similarity in study design. The first two possibilities taken together immediately offer an insight that is far more powerful than stand-alone current-source localization analysis

done with EEG or MEG: While it is of interest to localize current-source generating regions, it is far more important to identify the larger neurophysiologic system responsible for generating the observed dynamics. The combined EEG/fMRI studies by Goldman and Laufs would appear to provide this, even if their results are not in complete agreement. The third possibility, that observed correlations may not be causative in their association, is a problem that is inherent to all empirical observations at some level, and can only be resolved by using prior knowledge of the systems being studied and with careful experimental design. In total, these studies emphasize that oscillatory EEG dynamics can be observed in BOLD fMRI through power modulations or fluctuations within the BOLD frequency response (addressing concern 3 in the previous section), and illustrate that the combination of EEG with fMRI provides greater insights in this case than either method alone by revealing a dynamic functional network, not just the electrical current generators (addressing concern 5 from the previous section).

1.5. The Neurovascular Response and Local Field Potentials are Correlated in Stimulus-Driven Experiments

The EEG and MEG signals recorded at the scalp are believed to originate from post-synaptic potentials (PSPs) (Hamalainen et al., 2005) , which at larger spatial scales sum to produce local field potentials (LFPs) (Logothetis, 2004). Spiking activity, due to axonal firing, is less likely to produce a measurable scalp signal, since the radially-opposing axonal currents from a propagating action potential most closely resemble a quadrupole current source whose fields diminish as $1/R^3$ in distance, compared to $1/R^2$ for dipoles (Hamalainen et al., 2005). Furthermore, the bandwidth of LFPs is typically

below 300 Hz, similar to that of EEG and MEG signals, while action potential trains have a frequency response in the kilohertz range. Given the plausible relationship between EEG/MEG and LFPs, if one is interested in developing a paradigm for integrating EEG or MEG with fMRI, it is essential to consider how the LFP and the BOLD signal are related.

Studies by Logothetis suggest that the BOLD signal is more closely related to LFPs than multi-unit activity (MUA) (Logothetis et al., 2001). Simultaneous fMRI and microelectrode recordings were made from the primary visual cortex of macaque monkeys during visual stimulation with rotating checkerboards of varying durations and contrast levels. LFPs (10-130 Hz) and MUA (300- 3000 Hz) were derived through band separation of the microelectrode recordings, and were related to the BOLD signal from a region of interest (ROI) in the immediate vicinity of the electrode (7.1 x 2.3 mm) by comparing the power in each signal to the BOLD signal as a function of time. For all stimulus durations, the LFP power was found to persist throughout the stimulation period, producing substantial temporal overlap with the BOLD signal, while MUA power decreased rapidly after stimulus onset. A linear transfer function analysis between LFP or MUA power and the BOLD time course revealed that the LFP was a better predictor of the BOLD response. A similar study by Devor and colleagues used simultaneous microelectrode recordings and spectroscopic optical measurements to examine the correlation between LFPs, MUA, and oxy-, deoxy-, and total hemoglobin in rat barrel cortex during somatosensory stimulation over a wide dynamic range of stimulus intensities (Devor et al., 2003). Strong correlations were found between all hemodynamic quantities and both LFPs and MUA. A nonlinear power law relationship

between changes in LFP/MUA and both total and oxy-hemoglobin was also observed: increasing stimulus intensities resulted in approximately linear increases in hemodynamic responses, while LFP/MUA response levels tended to saturate as stimulus intensity increased. Together, these studies suggest that there is a strong correlation between LFP power and the BOLD response.

EEG and MEG appear to be a macroscopic manifestation of the LFP, which results from the spatial summation of post-synaptic potentials within a millimeter-range neighborhood. The fMRI BOLD response, on the other hand, largely reflects energy consumption from synaptic neurotransmitter re-cycling (Sibson et al., 1998), and is therefore also connected to the magnitude of post-synaptic potentials. These studies support the idea that EEG and fMRI share a common physiological source, providing evidence for the validity of multimodal integration of EEG/MEG and fMRI.

1.6. A State-Observation Model For Multimodal Imaging

Having established that multimodal integration of EEG/MEG and fMRI is physiologically plausible, how do we design experiments to best take advantage of their complementary capabilities? At this juncture it is helpful to reconsider the models that underlie our view of multimodal imaging. In previous work, fMRI has been thought of as a "prior" for EEG/MEG source localization, and used either explicitly in the context of a linear Gaussian estimation procedure (Bonmassar et al., 2001;Liu et al., 1998;Dale et al., 2000;Ahlfors et al., 1999), or as a means of seeding current source dipoles (e.g., (Vanni et al., 2004a;Vanni et al., 2004b)). An alternative view, however, is to view EEG/MEG and fMRI as separate observations of the same underlying neural dynamical

system (**Figure 1.2**). This agrees with our intuition that, underneath the details of their biophysical coupling mechanisms, and given similar or identical experimental conditions, these imaging modalities should be measuring "the same thing." When the biophysical details are considered, this view is supported by the fact that both EEG/MEG and fMRI appear to be products of post-synaptic activity, as discussed earlier.

We propose here a state-observation model that has the following components: 1) A state evolution equation describing the dynamics of the underlying neural process, possibly driven by an external stimulus, 2) An observation equation for EEG/MEG, 3) A system of neuro-vascular coupling equations that links neural activity to changes in local vascular function, and 4) An fMRI observation equation. We specify and discuss each of these components below.

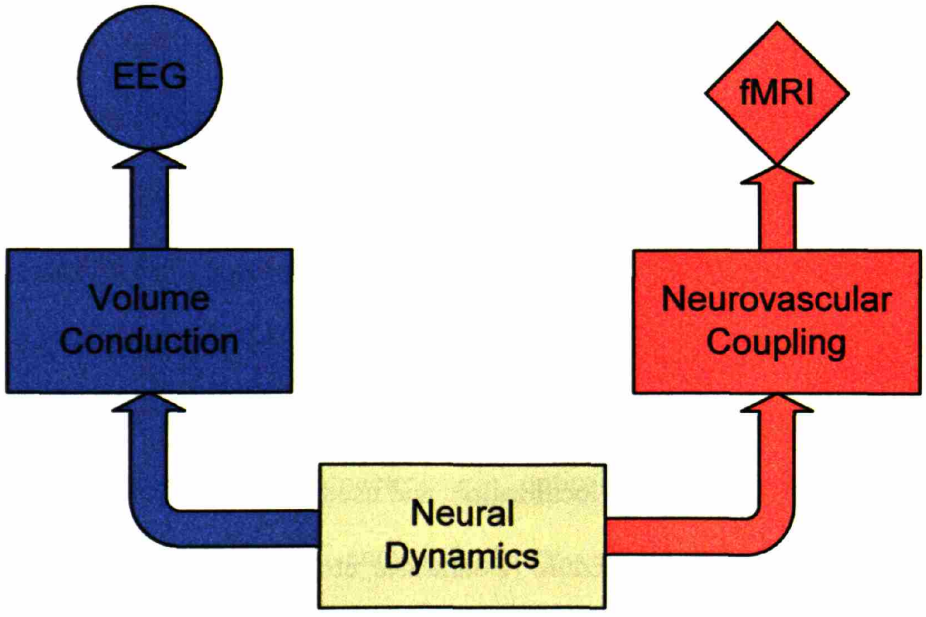

Figure 1. 2. EEG/MEG and fMRI represent separate observations of the same underlying process.

1.6.1. State evolution for underlying neural process $x_p(t)$

We represent the underlying neural process $x_p(t)$ as a state-space system, whose general form is given by

$$x_p(t) = f\left(x_p(t-1),...,x_p(t-K),c(t),...,c(t-L)\right), \tag{1.1}$$

where p indexes the spatial location of the neural source, c represents the experimental stimulus, K is the state order, and L is the input order. Given that both EEG/MEG and fMRI appear to be related to post-synaptic or local field potentials, we will treat $x_p(t)$ as a mesoscopic current source on the resolution scale of fMRI. The specific state-space model chosen will depend on the experiment being modeled, and could consist of a random walk, a simple linear state-space model (such as an autoregressive process), or a more complicated nonlinear model, such as a second-order Volterra expansion coupled to a linear moving-average of the external stimulus,

$$x_p(t) = \sum_{k=1}^{K} h_{1,p}(k)x_p(t-k) + \sum_{j=1}^{K}\sum_{k=1}^{K} h_{1,p}(k,j)x_p(t-k)x_p(t-j) + \sum_{k=0}^{L} b(k)c(t-k) \tag{1.2}$$

where $h_{1,p}(t)$ and $h_{1,p}(t,\tau)$ represent the first and second order Volterra kernels, respectively, and $b(k)$ the moving average filter. If the number of independent processes $x_p(t)$ is known to be small, linear or nonlinear input-output relationships between spatial locations could be considered as well.

1.6.2. EEG observation $\mathbf{y}_E(t)$

We use a realistic forward model for the EEG observation, whose lead field is represented by the matrix $\mathbf{A}$, with each component of the neural process current $x_p(t)$ and assemble it into a vector $\mathbf{x}(t)$, with observation noise $\mathbf{v}_1(t)$:

$$\mathbf{y}_E(t) = \mathbf{A}\mathbf{x}(t) + \mathbf{v}_1(t) \tag{1.3}$$

Note that $\mathbf{A}$ produces a change in spatial coordinates from locations within the brain with activity $x_p(t)$ to scalp locations where $\mathbf{y}_E(t)$ is recorded.

1.6.3. Neuro-vascular coupling for BOLD fMRI response $s_r(t)$

We present a neurovascular coupling equation relating the neural process $x_p(t)$ to the BOLD fMRI response $s_r(t)$ that models the local metabolic demand produced by neural activity, its spatial point-spread within the brain due to capillary beds with meso-scale spatial extent, and the temporal characteristics of the BOLD response.

1.6.3.a. Local metabolic demand due to neural activity

Numerous authors have used time-varying estimates of EEG, LFP, or MUA *power* (Logothetis et al., 2001;Goldman et al., 2002;Laufs et al., 2003b;Laufs et al., 2003a) or event-related potential (ERP) *amplitudes* (Liebenthal et al., 2003) as temporal covariates for fMRI analysis, successfully detecting fMRI activity in physiologically plausible locations within the brain. These studies used the time-varying power or amplitude time series as inputs or driving terms to a hemodynamic response kernel whose output was used for fMRI analysis. Recent work by Devor, et al., have identified a nonlinear relationship between hemodynamic response amplitude and both LFP and MUA power (Devor et al., 2003). Together, these studies suggest that the link between

local electrical activity and BOLD responses may include linear, quadratic, or higher-order powers of the neural process amplitude $|x_p(t)|$. We postulate the existence of an instantaneous (on the time-scale of EEG) local metabolic demand $z_p(t)$ that drives the BOLD neurovascular response. We represent $z_p(t)$ as a power series on $|x_p(t)|$,

$$z_p(t) = \sum_{m=1}^{M} a_m |x_p(t)|^m , \tag{1.4}$$

which includes first, second, and perhaps higher-order powers of $x_p(t)$.

1.6.3.b. Spatial point-spread due to capillary network

The instantaneous metabolic demand $z_p(t)$ at each spatial location indexed by p is subserved by a local capillary network whose volume-averaged flow is distributed over a spatial region in the vicinity of the active neurons. We represent this spatial point-spread as a spatial convolution with a finite impulse response spatial kernel K_p, resulting in a spatially-distributed BOLD input function $b_r(t)$:

$$b_r(t) = \sum_p z_p(t) K_{r-p} . \tag{1.5}$$

1.6.3.c. BOLD signal dynamics

The BOLD response $s_r(t)$ is modeled as the convolution $*$ of the input function $b_r(t)$ with a series of hemodynamic response kernels $g_k(t)$, each representing different time-scales of the BOLD response:

$$s_r(t) = b_r(t) * \sum_k g_k(t). \tag{1.6}$$

1.6.4. BOLD fMRI observation $y_{B,r}(t)$

We define a drift term $d_r(t)$ consisting of either low-order polynomials or low frequency sinusoids, and an ARMA(1,1) noise term $w_r(t)$ as in (Purdon et al., 2001;Purdon and Weisskoff, 1998), and combine these components to yield an fMRI observation $y_{B,r}(t)$:

$$y_{B,r}(t) = s_r(t) + d_r(t) + w_r(t). \tag{1.7}$$

In the next section, we use this model and its conceptual basis to gain insights into experimental design for multimodal imaging.

1.7. Insights for Experimental Design: Making the Case for Simultaneous Recordings of EEG and fMRI

By combining equations 1.4 through 1.6, we see that the BOLD signal, as represented by this model, is the smoothed response of a linear combination of the m-th powers of the time-course of the underlying neural system:

$$s_r(t) = \sum_k g_k(t) * \left(\sum_p K_{r-p} \sum_{m=1}^{M} a_m \left| x_p(t) \right|^m \right). \tag{1.8}$$

From equation 1.8, we can see that dynamics in the m-th powers of the neural system can only be seen within the frequency response of the neurovascular system.

One approach to this dilemma is to simply ignore the temporal evolution in fMRI and take it as static spatial information. The "fMRI-prior" or source-seeding strategies discussed earlier do this. Following the conceptual framework laid out by event-related potential research, such studies essentially assume that the dynamical system represented in equation 1.1 is *time-invariant*, thereby allowing one to average response waveforms across many trials in both EEG/MEG and fMRI, only to combine them later. Such time-invariant EEG/MEG, static fMRI approaches have the advantage that either EEG or MEG can be recorded separately from the fMRI experiment and later combined.

Another approach is to acknowledge the limits of fMRI's temporal resolution, but then design studies that can reveal interesting *time-varying* dynamics within these limits. Studies of this type naturally require simultaneous EEG and fMRI measurements, since simultaneous recordings of EEG and fMRI obey the "unities of place and time." Simultaneous recordings eliminate any cognitive or perceptual variability between measurements, since the recording environment is identical ("unity of place"). Furthermore, simultaneous recordings exploit the temporal correlations between EEG and fMRI that are brought about because simultaneous recordings measure the same realization of the underlying process ("unity of time"). This temporal correlation, in an appropriately designed experiment, could allow for the localization of dynamical sources that would not be observable in stand-alone EEG/MEG source localization due to "missing sources" (e.g., deep, radial, or closed-field sources). Despite the technical challenges involved, there are numerous examples of studies that take advantage of these

properties to study EEG oscillations (Goldman et al., 2002;Laufs et al., 2003b;Laufs et al., 2003a), epilepsy (Lemieux et al., 2001), sleep (Portas et al., 2000;Tanaka et al., 2003), and arousal (Matsuda et al., 2002).

Each of these studies share a common feature: They make use of large EEG signals with high signal-to-noise such as oscillations, sleep spindles, or epileptic spikes to track time-varying changes in the physiology of interest. Measuring time-varying changes in *stimulus-driven ERPs* is equally important, in order to study sensory and perceptual coupling as a function of awareness, sleep, anesthesia, pain, epilepsy, neurologically active drugs, or learning. Studies of this nature pose a significant methodological challenge, however, due to the extremely low signal to noise in ERP measurements. Traditionally, several hundred observations are required to estimate ERPs from EEG due to low signal-to-noise, leading to long observation times for a given estimate (Regan, 1989). For instance, a visual-evoked potential (VEP) estimated from 200 observations at an inter-stimulus interval of 500 milliseconds would require data spanning at least 100 seconds, assuming all "epochs" are within the noise rejection threshold. So while the temporal response of the neurovascular system poses limits on the time scales of observable neural dynamics, the signal-to-noise and estimation of ERPs would seem to pose a much larger restriction due to the large number of repetitions required for estimation. This motivates one of the central questions for this thesis: *Is it possible to estimate components of event-related potentials simultaneously with functional MRI in a time-varying manner to relate temporal correlations between ERP and fMRI dynamics?*

The 40-Hz auditory steady state response (ASSR) is an event related potential to a periodic stimulus, usually a train of clicks or tones, that has been related to sleep and loss of consciousness under general anesthesia. During sleep, the ASSR has been observed to decrease by approximately 50% compared to awake levels (Linden et al., 1985), and is completely abolished by loss of consciousness under general anesthesia (Plourde, 1996;Meuret et al., 2000;Plourde, 1999;Plourde et al., 1998). Because the ASSR is a periodic response, it can be estimated with frequency domain methods that vastly improve signal to noise, particularly on short segments of data, allowing the possibility of time-varying estimation. Furthermore, changes in level of arousal, sleep, and loss of consciousness under general anesthesia are all phenomena that evolve over seconds, tens of seconds, and minutes, and are therefore within the bandwidth of the fMRI BOLD response. Consequently, *the 40-Hz ASSR is an ideal candidate for time-varying estimation in conjunction with fMRI.*

If the SNR of event-related potentials is a concern, so is that of fMRI. The SNR of the BOLD response can be enhanced through coil design using phased array systems (Frederick et al., 1999), but also increases dramatically with increased static field strength. While the majority of EEG/fMRI studies have been conducted at 1.5 Tesla, stand-alone fMRI studies are more commonly done at higher field strengths such as 3 or 4 Tesla. Several sites throughout the world have developed whole-body human scanners at 7 Tesla. Higher field strengths pose a tremendous challenge for simultaneous EEG recordings because the larger static field enhances electromechanical noise coupling due to study subject head motion and cardio-respiratory pulsation, and also increases the risk of electrode heating, since the radio-frequency pulses used at higher field strengths

typically deposit more energy into the body. Despite these challenges, when one considers the state-observation paradigm presented here, enhanced BOLD SNR increases the likelihood that subtle temporal correlations can be observed between EEG and BOLD. Accordingly, *establishing EEG/fMRI methods that are able to handle the unique challenges of fMRI at 3 and 7 Tesla is a high priority.*

1.8. Specific Aims

We present the following specific aims, to be developed in the remainder of the thesis:

Aim 1: Develop and construct acquisition hardware, electrode sets, and auditory stimulus delivery systems for recording simultaneous EEG and fMRI at 3 and 7 Tesla (Chapters 2 and 3).

Aim 2: Develop adaptive filtering methods for removing the ballistocardiogram artifact from EEG recorded during fMRI (Chapter 4).

Aim 3: Record 40-Hz auditory steady-state potentials (ASSRs) simultaneously with fMRI to establish a paradigm for studying correlations between time-varying changes in ERP amplitudes and fMRI BOLD responses (Chapter 5).

1.9. References

1. Ahlfors SP, Simpson GV, Dale AM, Belliveau JW, Liu AK, Korvenoja A, Virtanen J, Huotilainen M, Tootell RB, Aronen HJ, Ilmoniemi RJ (1999) Spatiotemporal activity of a cortical network for processing visual motion revealed by MEG and fMRI. J Neurophysiol 82: 2545-2555.

2. Allen PJ, Josephs O, Turner R (2000) A method for removing imaging artifact from continuous EEG recorded during functional MRI. Neuroimage 12: 230-239.

3. Biswal B, Yetkin FZ, Haughton VM, Hyde JS (1995) Functional connectivity in the motor cortex of resting human brain using echo-planar MRI. Magn Reson Med 34: 537-541.

4. Bonmassar G, Schwartz DP, Liu AK, Kwong KK, Dale AM, Belliveau JW (2001) Spatiotemporal brain imaging of visual-evoked activity using interleaved EEG and fMRI recordings. Neuroimage 13: 1035-1043.

5. Bronzino JD (1999) Biomedical Engineering Handbook. CRC Press.

6. Burock MA, Buckner RL, Woldorff MG, Rosen BR, Dale AM (1998) Randomized event-related experimental designs allow for extremely rapid presentation rates using functional MRI. Neuroreport 9: 3735-3739.

7. Buxton RB (2001) Biomedical Engineering Handbook. Cambridge University Press.

8. Culver JP, Siegel AM, Stott JJ, Boas DA (2003) Volumetric diffuse optical tomography of brain activity. Opt Lett 28: 2061-2063.

9. Dale AM, Liu AK, Fischl BR, Buckner RL, Belliveau JW, Lewine JD, Halgren E (2000) Dynamic statistical parametric mapping: combining fMRI and MEG for high-resolution imaging of cortical activity. Neuron 26: 55-67.

10. Dale AM, Sereno MI (1993) Improved localization of cortical activity by combining EEG and MEG with MRI cortical surface re-construction: A linear approach. J Cogn Neurosci 5: 55-67.

11. Devor A, Dunn AK, Andermann ML, Ulbert I, Boas DA, Dale AM (2003) Coupling of total hemoglobin concentration, oxygenation, and neural activity in rat somatosensory cortex. Neuron 39: 353-359.

12. Fischl B, Sereno MI, Tootell RB, Dale AM (1999) High-resolution intersubject averaging and a coordinate system for the cortical surface. Hum Brain Mapp 8: 272-284.

13. Franceschini MA, Boas DA (2004) Noninvasive measurement of neuronal activity with near-infrared optical imaging. Neuroimage 21: 372-386.

14. Frederick Bd, Wald LL, Maas LC, III, Renshaw PF (1999) A phased array echoplanar imaging system for fMRI. Magn Reson Imaging 17: 121-129.

15. Goldman RI, Stern JM, Engel J, Jr., Cohen MS (2002) Simultaneous EEG and fMRI of the alpha rhythm. Neuroreport 13: 2487-2492.

16. Greicius MD, Krasnow B, Reiss AL, Menon V (2003) Functional connectivity in the resting brain: a network analysis of the default mode hypothesis. Proc Natl Acad Sci U S A 100: 253-258.

17. Hamalainen M, Hari R, Ilmoniemi RJ, Knuutila J, Lounasmaa OV (2005) Magnetoencephalography-- theory, instrumentation, and applications to noninvasive studies of the working human brain. Reviews of Modern Physics 65: 413-497.

18. Haueisen J, Tuch DS, Ramon C, Schimpf PH, Wedeen VJ, George JS, Belliveau JW (2002) The influence of brain tissue anisotropy on human EEG and MEG. Neuroimage 15: 159-166.

19. Hillebrand A, Barnes GR (2002) A quantitative assessment of the sensitivity of whole-head MEG to activity in the adult human cortex. Neuroimage 16: 638-650.

20. Jenkinson M, Smith S (2001) A global optimisation method for robust affine registration of brain images. Med Image Anal 5: 143-156.

21. Kwong KK, Belliveau JW, Chesler DA, Goldberg IE, Weisskoff RM, Poncelet BP, Kennedy DN, Hoppel BE, Cohen MS, Turner R, Cheng HM, Brady TJ, Rosen BR (1992) Dynamic magnetic resonance imaging of human brain activity during primary sensory stimulation. Proc Natl Acad Sci U S A 89: 5675-5679.

22. Laufs H, Kleinschmidt A, Beyerle A, Eger E, Salek-Haddadi A, Preibisch C, Krakow K (2003a) EEG-correlated fMRI of human alpha activity. Neuroimage 19: 1463-1476.

23. Laufs H, Krakow K, Sterzer P, Eger E, Beyerle A, Salek-Haddadi A, Kleinschmidt A (2003b) Electroencephalographic signatures of attentional and cognitive default modes in spontaneous brain activity fluctuations at rest. Proc Natl Acad Sci U S A 100: 11053-11058.

24. Leahy RM, Mosher JC, Spencer ME, Huang MX, Lewine JD (1998) A study of dipole localization accuracy for MEG and EEG using a human skull phantom. Electroencephalogr Clin Neurophysiol 107: 159-173.

25. Lemieux L, Salek-Haddadi A, Josephs O, Allen P, Toms N, Scott C, Krakow K, Turner R, Fish DR (2001) Event-related fMRI with simultaneous and continuous EEG: description of the method and initial case report. Neuroimage 14: 780-787.

26. Liebenthal E, Ellingson ML, Spanaki MV, Prieto TE, Ropella KM, Binder JR (2003) Simultaneous ERP and fMRI of the auditory cortex in a passive oddball paradigm. Neuroimage 19: 1395-1404.

27. Linden RD, Campbell KB, Hamel G, Picton TW (1985) Human auditory steady state evoked potentials during sleep. Ear Hear 6: 167-174.

28. Liu AK, Belliveau JW, Dale AM (1998) Spatiotemporal imaging of human brain activity using functional MRI constrained magnetoencephalography data: Monte Carlo simulations. Proc Natl Acad Sci U S A 95: 8945-8950.

29. Liu AK, Dale AM, Belliveau JW (2002) Monte Carlo simulation studies of EEG and MEG localization accuracy. Hum Brain Mapp 16: 47-62.

30. Logothetis NK (2004) Functional MRI in monkeys: A bridge between human and animal brain research. In: The Cognitive Neurosciences (Gazzaniga MS, ed), pp 957-969. Cambridge, Massachusetts: MIT Press.

31. Logothetis NK, Pauls J, Augath M, Trinath T, Oeltermann A (2001) Neurophysiological investigation of the basis of the fMRI signal. Nature 412: 150-157.

32. Lowe MJ, Mock BJ, Sorenson JA (1998) Functional connectivity in single and multislice echoplanar imaging using resting-state fluctuations. Neuroimage 7: 119-132.

33. Lutkenhoner B (1996) Current dipole localization with an ideal magnetometer system. IEEE Trans Biomed Eng 43: 1049-1061.

34. Matsuda T, Matsuura M, Ohkubo T, Ohkubo H, Atsumi Y, Tamaki M, Takahashi K, Matsushima E, Kojima T (2002) Influence of arousal level for functional magnetic resonance imaging (fMRI) study: simultaneous recording of fMRI and electroencephalogram. Psychiatry Clin Neurosci 56: 289-290.

35. Meuret P, Backman SB, Bonhomme V, Plourde G, Fiset P (2000) Physostigmine reverses propofol-induced unconsciousness and attenuation of the auditory steady state response and bispectral index in human volunteers. Anesthesiology 93: 708-717.

36. Nunez PL (1995a) Neocortical dynamics and human EEG rhythms.New York: Oxford University Press.

37. Nunez PL (1995b) Quantitative states of neocortex. In: Neocortical dynamics and human EEG rhythms (Nunez PL, ed), pp 3-67. New York: Oxford University Press.

38. Nunez PL, Silberstein RB (2000) On the relationship of synaptic activity to macroscopic measurements: does co-registration of EEG with fMRI make sense? Brain Topogr 13: 79-96.

39. Ogawa S, Lee TM, Kay AR, Tank DW (1990) Brain magnetic resonance imaging with contrast dependent on blood oxygenation. Proc Natl Acad Sci U S A 87: 9868-9872.

40. Ogawa S, Tank DW, Menon R, Ellermann JM, Kim SG, Merkle H, Ugurbil K (1992) Intrinsic signal changes accompanying sensory stimulation: functional brain mapping with magnetic resonance imaging. Proc Natl Acad Sci U S A 89: 5951-5955.

41. Plourde G (1996) The effects of propofol on the 40-Hz auditory steady-state response and on the electroencephalogram in humans. Anesth Analg 82: 1015-1022.

42. Plourde G (1999) Auditory evoked potentials and 40-Hz oscillations. Anesthesiology 91: 1187-1189.

43. Plourde G, Villemure C, Fiset P, Bonhomme V, Backman SB (1998) Effect of isoflurane on the auditory steady-state response and on consciousness in human volunteers. Anesthesiology 89: 844-851.

44. Portas CM, Krakow K, Allen P, Josephs O, Armony JL, Frith CD (2000) Auditory processing across the sleep-wake cycle: simultaneous EEG and fMRI monitoring in humans. Neuron 28: 991-999.

45. Purdon PL, Solo V, Weisskoff RM, Brown EN (2001) Locally regularized spatiotemporal modeling and model comparison for functional MRI. Neuroimage 14: 912-923.

46. Purdon PL, Weisskoff RM (1998) Effect of temporal autocorrelation due to physiological noise and stimulus paradigm on voxel-level false-positive rates in fMRI. Hum Brain Mapp 6: 239-249.

47. Regan D (1989) Human brain electrophysiology : evoked potentials and evoked magnetic fields in science and medicine. New York: Elsevier.

48. Sibson NR, Dhankhar A, Mason GF, Rothman DL, Behar KL, Shulman RG (1998) Stoichiometric coupling of brain glucose metabolism and glutamatergic neuronal activity. Proc Natl Acad Sci U S A 95: 316-321.

49. Talairach J, Tourneau P (1988) Co-planar stereotaxic atlas of the human brain. Stuttgart: Georg Thieme Verlag.

50. Tanaka H, Fujita N, Takanashi M, Hirabuki N, Yoshimura H, Abe K, Nakamura H (2003) Effect of stage 1 sleep on auditory cortex during pure tone stimulation: evaluation by functional magnetic resonance imaging with simultaneous EEG monitoring. AJNR Am J Neuroradiol 24: 1982-1988.

51. Vanni S, Dojat M, Warnking J, Delon-Martin C, Segebarth C, Bullier J (2004a) Timing of interactions across the visual field in the human cortex. Neuroimage 21: 818-828.

52. Vanni S, Warnking J, Dojat M, Delon-Martin C, Bullier J, Segebarth C (2004b) Sequence of pattern onset responses in the human visual areas: an fMRI constrained VEP source analysis. Neuroimage 21: 801-817.

Chapter 2
Methodological Challenges For Electrophysiological Recording During Magnetic Resonance Imaging

Concurrent recording of electroencephaologram (EEG) during magnetic resonance imaging (MRI) holds promise for both basic neuroscience studies and clinical diagnostic and monitoring applications. However, in order to realize the full potential of this technique, a number of methodological challenges related to the physics of the MRI environment must first be solved. In this chapter, we review these challenges and identify design goals for EEG-fMRI hardware and software systems.

2.1. Noise Sources for Electrophysiological Recording in the MRI Environment

MRI systems present an electromagnetically hostile environment for electrophysiological recordings. In addition to the large static magnetic field B_0 (typically at 1.5 or 3 Tesla (T), but as large as 7 or 8 T), MRI systems produce radio-frequency (RF) interference from the B_1 field, as well as time-varying magnetic

gradients. These noise sources can severely compromise the quality of EEG recordings. One source of noise coupling comes from electromagnetic induction due to circuit-motion within the static field, illustrated in **Figure 2.1**. The amplitude of the induced noise is directly proportional to the loop size of the circuit, and the static field strength. Mechanical vibrations due to the MRI helium pump produce large, ~50 uV oscillatory artifacts located within the standard clinical EEG bandwidth of 0.5-50 Hz (Garreffa et al., 2004). As a point of reference, oscillatory EEG rhythms such as alpha (8-13 Hz) or delta (0.5-4 Hz) range from ~10-100 uV in amplitude, while event-related potentials (ERPs) vary in size from ~1 to 10 uV. Fortunately, this source of noise can be eliminated simply by turning off the helium pump during functional scanning. Physiological motion due to cardiac pulsation ("ballistocardiogram") or respiration poses a more challenging problem, since there is a limit to how much that motion can be attenuated from immobilization or controlled breathing. The ballistocardiogram artifact can exceed 10^2 uV at 1.5 T in many cases (Allen et al., 1998;Bonmassar et al., 2001a), and overlaps in frequency with important EEG bands such as delta, theta (4-8 Hz), and alpha, (Bonmassar et al., 2001a) as well as the event-related potentials which occupy those bands (e.g., (Makeig et al., 2002)). An example of the ballistocardiogram artifact is shown in **Figure 2.2**.

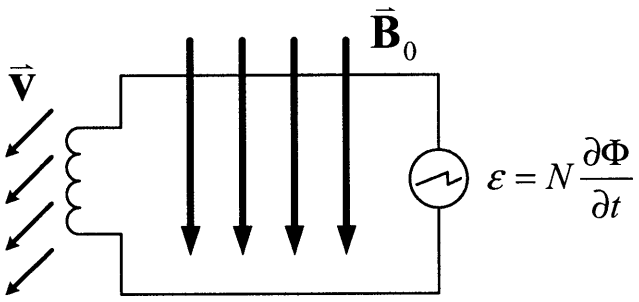

Figure 2. 1. Noise coupling (ε) from motion ($\vec{v}$) within the static magnetic field ($\vec{B}$).

Beyond the static field, the RF and gradient fields introduce noise and present difficulties for instrumentation design. RF pulses can produce artifacts on the order of 10^2 uV that arise from either demodulation within nonlinear portions of the amplifier/acquisition circuit, or due to aliasing (Anami et al., 2003). Amplifiers and acquisition units can be shielded from RF noise, but gradient switching noise cannot be shielded, since magnetic shielding requires ferromagnetic metals that are unsafe in the static magnetic field (Ott, 1988). The size of these artifacts is generally between 10^3 to 10^4 uV, and is proportional to the loop size of amplifier circuits and the gradient slew rate (Anami et al., 2003). This poses a particular problem for functional imaging at higher field strengths such as 3 or 7 T, since faster gradient read-outs (i.e., faster slew rates) are generally desired to reduce susceptibility-induced image warping during EPI. These large gradient artifacts can saturate the high-gain instrumentation amplifiers found in conventional EEG equipment (Ives et al., 1993;Huang-Hellinger et al., 1995). When combined with the standard practice of using low-frequency (~0.5 Hz) decoupling capacitors (~0.33 uF) at the input of EEG amplifiers (Ives et al., 1993;Mirsattari et al.,

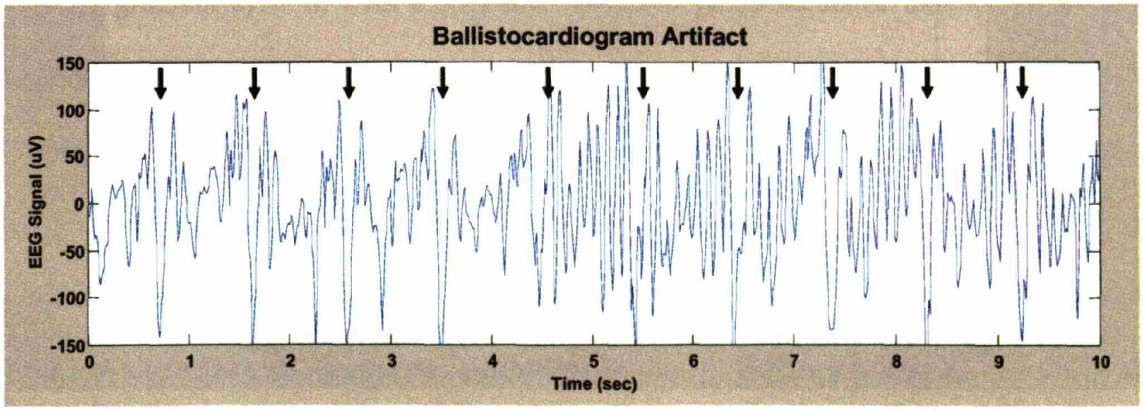

Figure 2.2. Ballistocardiogram artifact from 1.5 T EEG-fMRI recording. Artifact pulses are denoted by arrows

2005), these gradient artifacts can corrupt the EEG signal for several seconds after MRI acquisition (**Figure 2.3**).

A number of acquisition strategies exist for integrating EEG and MRI recordings in a way that minimizes the influence of this MRI-induced noise. The simplest acquisition strategy is to interleave RF/gradient "silent" periods between fMRI slice or volume acquisitions, as illustrated in **Figure 2.4** (Bonmassar et al., 1999;Bonmassar et al., 2001b;Goldman et al., 2000;Garreffa et al., 2004). With appropriate amplifier design to minimize post-EPI recovery time, this strategy results in excellent EEG SNR during the silent period, and is best suited for stimulus-driven experiments where ERP stimuli can be presented during the silent period, with volume acquisitions arranged relative to these stimuli to maximize the BOLD response (Liebenthal et al., 2003;Garreffa et al., 2004). Other applications such as epilepsy (Lemieux et al., 2001) or studies of

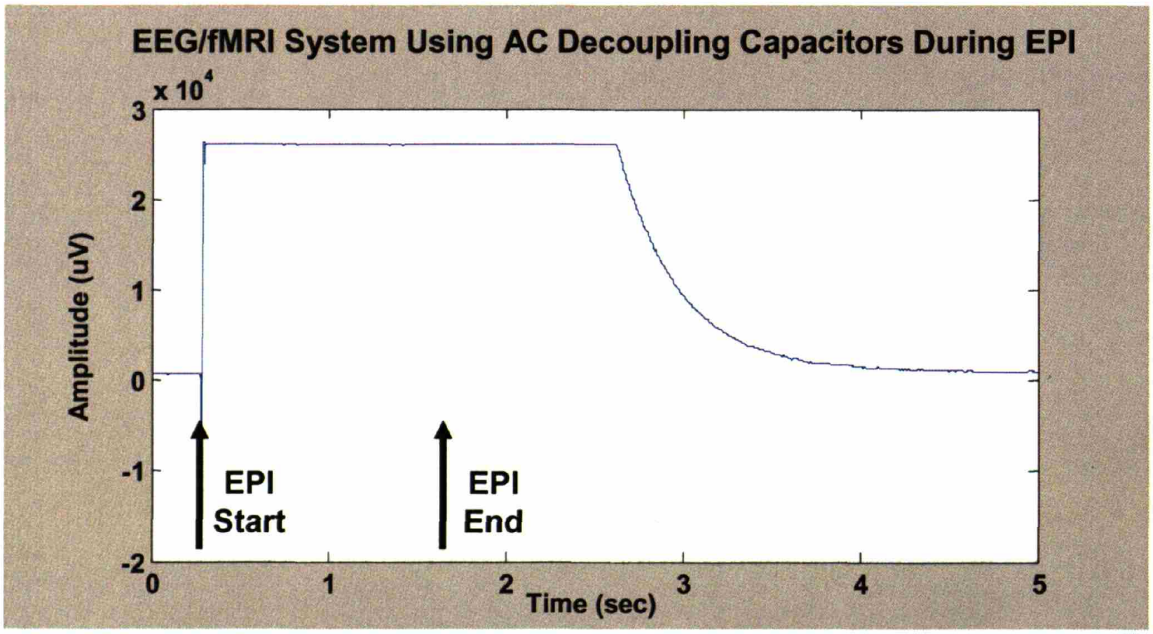

Figure 2.3. Saturation and recovery of high-gain EEG amplifier featuring low-frequency de-coupling capacitors. Approximately 2 seconds of data following EPI are lost due to saturation.

spontaneous oscillations (Laufs et al., 2003b;Laufs et al., 2003a), have employed fully continuous EEG during fMRI. In these studies, the neural events of interest occur at random intervals and cannot be constrained to occur within any particular time window. To remove the imaging artifact, a standard image artifact template from corrupted EEG is subtracted from the recordings (Allen et al., 2000). In these studies, a high sampling rate, dictated by the frequency of the gradient system, is required to minimize the presence of aliasing (Garreffa et al., 2003). Template subtraction methods rely on time-invariance of the imaging artifact waveform to achieve noise control, but this time-invariance is compromised if the waveform is undersampled and aliased (Vaidyanathan, 1993). In practice, the residual artifact after subtraction can be quite large (Mirsattari et al., 2005), rendering this technique less useful for ERP studies. This is particularly true when one considers the slow time constant of the fMRI BOLD response, since, beyond a certain point, higher temporal sampling of the BOLD response does not improve temporal resolution. A very clever hybrid of these two strategies has recently been proposed by Anami, et al. (Anami et al., 2003), where individual EEG samples are taken in synchrony with the gradient system, with a specially modified pulse-sequence that lengthens the duration of gradient plateaus to minimize induced signals. This system works well at 1.5 T, but may not work well at higher fields since, even with faster gradients, plateaus must be inserted into the gradient readout process, lengthening the readout time and introducing additional susceptibility warping. A similar, but alternative solution not requiring a special pulse sequence would be to simply synchronize the EEG ADC and scanner clocks in an attempt to preserve the time-invariance of the gradient artifact (Goldman et al., 2000).

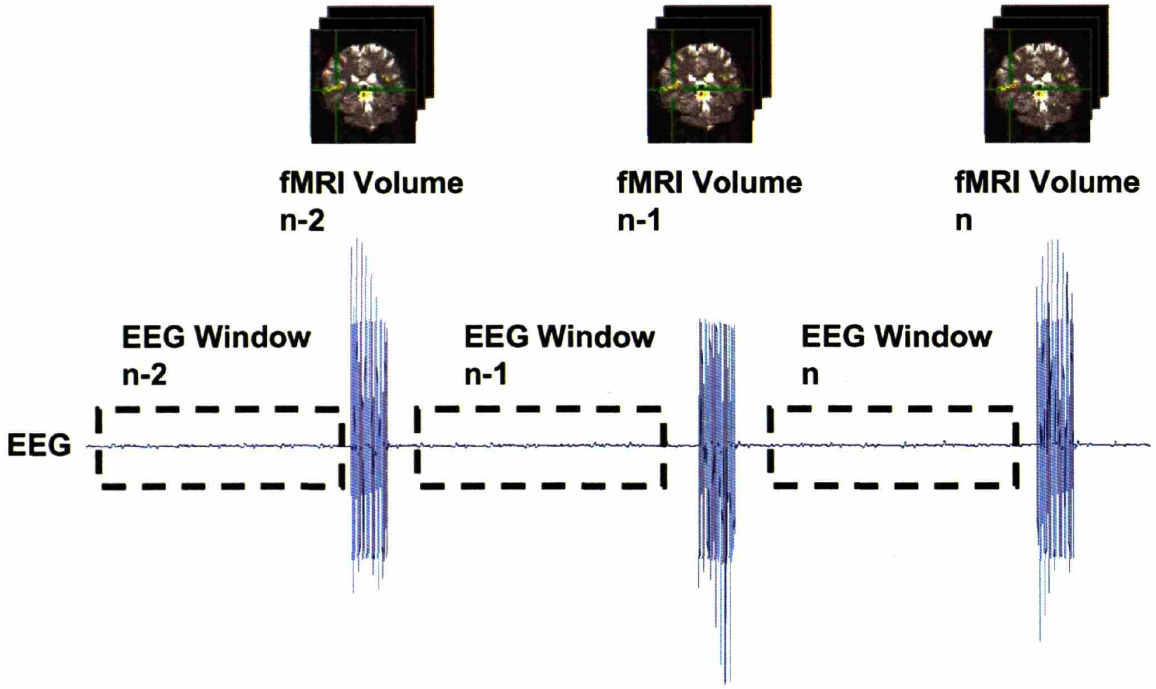

Figure 2.4. Example of interleaving EEG and fMRI acquisitions.

From this discussion, we can identify a number of important design features for EEG-fMRI hardware. EEG-fMRI acquisition hardware should be designed to have: *1) small loop sizes prior to analog-to-digital conversion (ADC), 2) high dynamic range, achieved through lower front-end amplifier gain and/or higher ADC bit-resolution, and 3) either high-rate EEG sampling or sampling that is synchronized to the acquisition clocks that control gradient switching.*

2.2. MRI Safety and Compatibility

Clinical devices for use in the MRI scanner are classified as either "MR-safe" or "MR-compatible." Devices that pose no additional risk to the patient or other individuals, but which may compromise the quality of diagnostic information, are deemed "MR-safe," whereas devices that are MR-safe yet preserve diagnostic

information are considered "MR-compatible" (Shellock and Crues, III, 2002). Special-purpose hardware for EEG-fMRI must meet the criteria for MR-safety, and to the extent that imaging-related EEG artifacts can be minimized or eliminated, should also meet the MR-compatible criterion as well.

At the most basic level, to meet the MR-safe criterion, construction materials for EEG-fMRI amplifiers and acquisition units must be non-ferromagnetic. For circuit boards and components, as well as chassis materials and cables, this is usually not difficult, since non-ferrous metals such as copper, aluminum, or brass can be used. Notable exceptions to this include mu-metals used for magnetic shielding, as well as ferrite-beads used for RF filtering. Connectors pose a more difficult problem. While plastic connectors can be used in many cases, metallic connectors are almost always preferred when electromagnetic interference (EMI, discussed below) is a concern, and non-ferrous metallic connectors are difficult to find. For instance, standard D-sub connectors used in personal computers (e.g., DB-9, 15, or 25) are unavailable in non-ferrous metals, leading some MR equipment manufacturers to employ standard ferrous-based connectors on the assumption that the connectors will be securely latched to a wall or penetration panel. Lapses in operator judgment or attention are always a possibility (e.g., (Colletti, 2004)). Since EEG-fMRI equipment is usually situated within or very close to the MRI bore, non-magnetic connectors such as the MIL-spec 83513 "micro-D" series should be used whenever a metallic connector is required.

As discussed in Section 2.1, circuit loops must be minimized to reduce noise coupling from both the static field, in the form of physiologic or environmental vibrations, or from the MRI gradient system. This implies that noise coupling can be

minimized by shortening the length of wires from electrode to pre-amplifier, and from amplifier to analog-to-digital conversion (ADC). Early commercially-available EEG-fMRI systems used amplifiers and ADC's located outside the MRI room, with a large cabling system connecting the electrodes to the amplifier and ADC's via the MRI penetration panel (e.g., the "Mag-link" system manufactured by Neuroscan-Compumedics, El Paso, TX). In addition to increasing environmental noise coupling, this system posed a potential subject safety risk since the long electrode wires had a potential to increase RF heating. This risk has only recently been recognized by researchers such as Angelone, et al., (Angelone et al., 2004), and will be discussed in Section 2.4. An alternative was to use analog optical circuits to multiplex and de-multiplex EEG signals after amplification (Ives et al., 1993;Mirsattari et al., 2005), but the high degree of nonlinearity present in these analog optical systems compromised EEG quality. More recently, a number of vendors (e.g., Brain Products GmbH, Munich, Germany; Schwarzer GmbH, Munich, Germany) have begun to offer EEG/fMRI acquisition units that perform both amplification and ADC within the MRI bore. With these systems, noise coupling from the static field and gradient is minimized, as is RF heating risk by way of shorter electrode wires, but RF noise coupling becomes a much larger problem, because the digital circuitry found within the ADC unit will both emit and receive RF energy to and from the MRI coil systems, potentially corrupting or disabling both.

Electromagnetic interference (EMI) between MRI and EEG systems can contaminate or disable measurements of both systems. We have already discussed how gradient and RF noise can corrupt EEG signals. In addition to this, digital EEG

acquisition hardware placed inside or in the vicinity of the MRI bore can transmit EMI to the MRI's RF coils. If the EMI has significant power at the MRI system's center (Larmor) frequency, the resulting image will be corrupted. Similarly, gradient and RF noise can disrupt the EEG system's circuitry: Analog instrumentation amplifiers can be disrupted by gradient-induced fluctuations in power, while RF noise can disrupt digital acquisition circuits. The noise sensitivity of analog circuits can be reduced by minimizing the size of the circuit, and by choosing amplifiers with a high "VCC rejection-ratio" (i.e., amplifier integrated circuits that minimize coupling of power fluctuations to output noise). Minimizing EMI emissions and susceptibility requires careful design of circuits, print-circuitboards (PCBs), shielding enclosures, and cabling harnesses. We briefly review these elements in the next section.

2.3. Design Principles for Electromagnetic Compatibility (EMC)

Electromagnetic compatibility (EMC) refers to the ability of an electronic system to function properly in its intended electromagnetic environment, without being a source of interference to that environment. Control of EMI requires a number of critical design elements including: 1) Suppression of EMI with proper circuit design and PCB layout, 2) A well-designed power and grounding system, 3) Containment of emissions with a shielded enclosure, and 4) Filtering of input-output lines (Matthews, 2004;Archambeault, 2002). Because MRI is both RF sensitive, requiring RF shielded rooms to prevent EMI from external sources, as well as RF intensive, producing considerable RF power during the imaging process, the EMC design challenge for EEG-fMRI equipment is considerable.

2.3.1. Circuit and PCB Design For EMC

Control of EMI should always begin at the circuit and PCB level, but rarely does in most development processes. A more typical development path is to complete circuit design and PCB layout first, leaving EMC as an afterthought to be handled with aggressive shielding and filtering, resulting in time and cost overruns upwards of 200-500% (Matthews, 2004;Archambeault, 2002). The overall solution may or may not require a complete re-design of the circuit and PCB with EMC principles in mind. By conservation of current, any current flowing within a signal trace must have a return current, as depicted in **Figure 2.5**. If this return current flows directly underneath the signal trace, the electromagnetic fields from the opposing "differential mode" currents have a tendency to cancel one another, minimizing EMI radiation (**Figure 2.5.a**). This effect is termed "flux-cancellation." However, if the return current takes a long circuitous return path due to poor routing choices, this self-cancellation effect will not occur, and EMI emissions will be high. RF return currents that flow over large portions of a PCB as

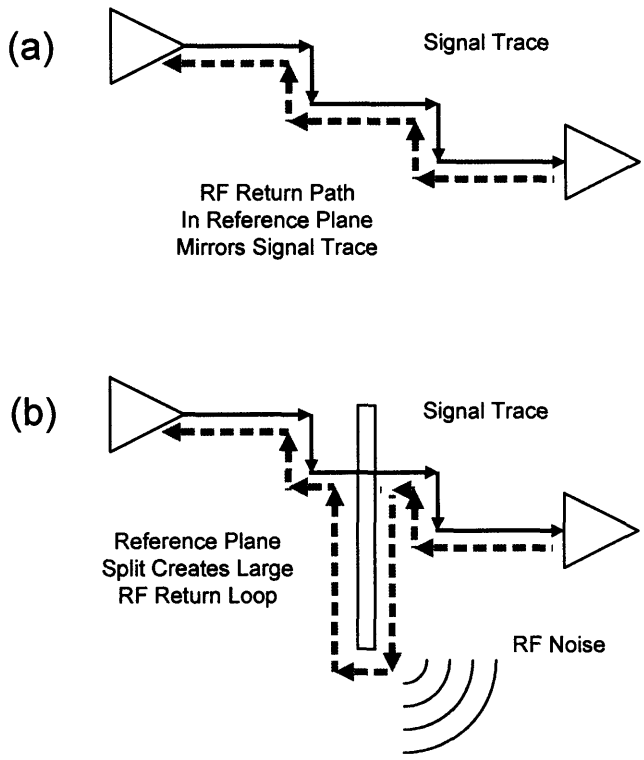

Figure 2.5. PCB return currents: (a) Correctly routed with return current directly under source current and (b) Incorrectly routed over reference plane partition, forcing return current to make a large loop, emitting RF interference.

in **Figure 2.5.b** are termed "common-mode" currents and are the major source of EMI (Montrose, 2000). Proper PCB design for EMC entails managing return currents to maximize flux-cancellation and minimize and common-mode RF currents: *Every signal trace must have an unobstructed return current path in close proximity to minimize EMI.*

Mis-management of traces and return currents for high-speed, fast rise-time signals is the most common source of EMI at the PCB level. Typical culprits include clock signals, memory signals, or address bus signals. For a given frequency or harmonic f with wavelength $\lambda = c/f$ (where c is the speed of light), a PCB trace will begin to behave like a transmission-line when the PCB trace reaches a critical length of $\lambda/20$ or greater (Montrose, 2000). Table 2.1 gives $\lambda/20$ for a few frequencies in the MHz range. While most microprocessor systems used for data acquisition applications run at modest frequencies in the neighborhood of 50-100 MHz, the sharp transitions present in fast slew-rate clocks produce large harmonics. The Fourier coefficients a_n of a square wave scale as $1/n$, for instance, meaning that harmonics far above the fundamental will be present in most high-speed clock signals. Hence, signal traces as short as a few centimeters can show transmission-line behavior, and PCB layouts must be designed to prevent this.

Frequency	$\lambda/20$ Distance
64 MHz	23.4
128 MHz	11.7 cm
300 MHz	5.0 cm
600 MHz	2.5 cm

Table 2.1. $\lambda/20$ at Various Frequencies

PCB traces on multi-layer boards featuring power and ground planes ("reference" planes) can be modeled as either microstrips or striplines, as depicted in **Figure 2.6.** Ideally, these reference planes provide a low-impedance conduit for

current return along a path directly beneath and/or above the signal currents, thereby minimizing current flux and RF emissions. The microstrip configuration describes most surface traces with a single reference plane beneath (**2.6.a**), while the stripline configuration describes traces that are embedded between two reference planes (**2.6.b**). As suggested in the figure, the stripline provides the greatest protection from radiated EMI. Hence, critical signal lines such as clocks must be embedded between reference planes. These critical signal lines should be treated as transmission lines with impedance matching and termination to prevent reflections or standing waves. The impedance of the stripline or microstrip, given the dielectric constant and thickness of the PCB material, can be adjusted by varying the width of the trace, and can be terminated with different discrete component configurations, depending on the source and load impedances. To minimize cross-talk between traces, they should be separated by a minimum distance, typically twice the width of a trace (the "3W" rule), to avoid cross-talk (Montrose, 2000).

Different multi-layer stack-up configurations have been suggested for 4, 6, 8, or 10-layer boards (Matthews, 2004;Archambeault, 2002). Usually, these configurations

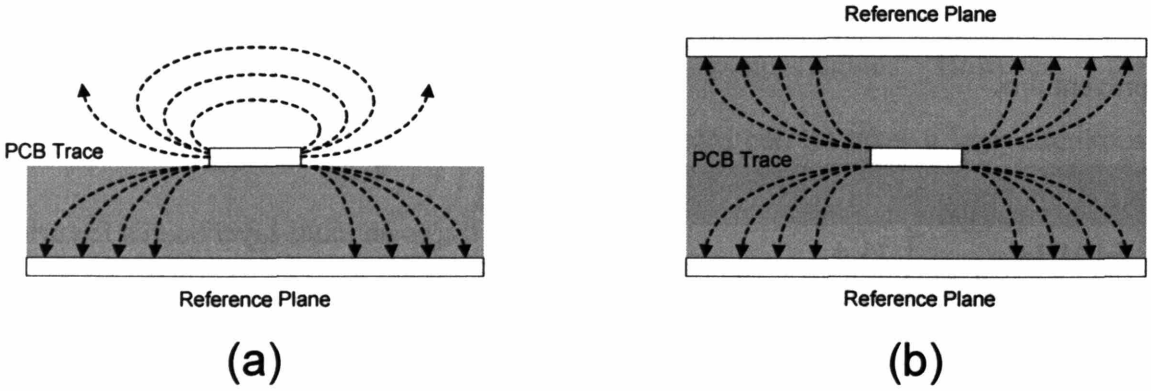

Figure 2.6. Stripline and microstrip configurations, showing electric field distribution. The stripline configuration provides superior flux cancellation and should be used for high-speed lines whenever possible.

embed critical signal layers between power and ground planes (**Figure 2.7**). Some authors have suggested that power planes provide inferior flux-cancellation performance due to transient power demands from digital circuits, indicating that only "ground" reference planes should be used for this purpose (Montrose, 2000), but this may provide an overly rigid constraint for trace routing and component placement. Other authors argue that the use of bulk capacitance, high-frequency ceramic capacitors, and the inherent capacitance of reference planes can minimize power plane voltage fluctuations to acceptable levels (Matthews, 2004;Archambeault, 2002).

EEG-fMRI amplifiers and acquisition systems require that both high-speed DAQ and low-noise analog amplification co-exist within the same circuit. This poses a challenging circuit design problem when combined with EMC requirements. In particular, noise from digital circuits must not couple with more sensitive analog circuits, both to prevent contamination of sensitive analog EEG data, as well as to limit EMI transmission along the PCB. This can be accomplished by introducing reference plane splits or "isolation zones" that prevent digital return currents from influencing more sensitive analog circuits. While establishing these isolation zones, care must be taken to provide return paths for signal traces that cross partitions by using "stitching capacitors" that provide high-frequency return paths (e.g., for digital control lines coming to or

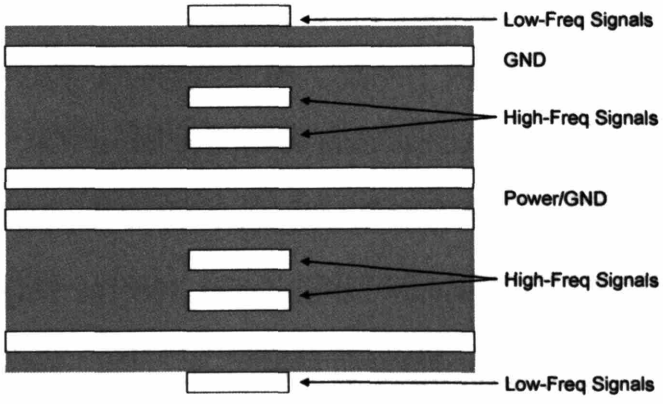

Figure 2.7. Example of a 10-layer PCB stack-up for EMI control, placing high-frequency signals between reference planes.

from ADC integrated circuits), as illustrated in **Figure 2.8**. Otherwise, return currents could be forced to take the "long way home," paradoxically worsening the EMI problem (Figure 2.5.b).

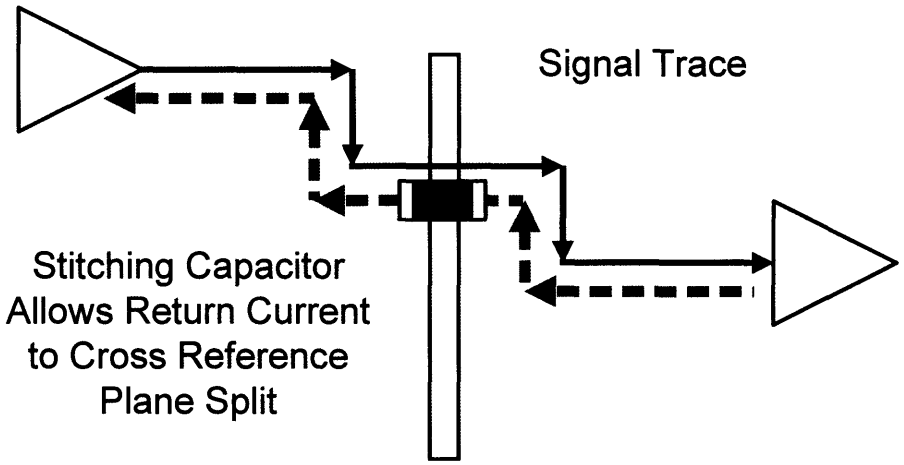

Figure 2.8. Stitching capacitors allow return currents to cross plane splits without taking "the long way home."

2.3.2. EMI Shielding

Shielded cables and enclosures must be used to prevent EMI transmission into the MRI environment, and to prevent MRI RF sequences from influencing EEG-fMRI hardware. Shielded cables and enclosures operate by either reflecting or absorbing electromagnetic energy. At frequencies above 10 MHz, the majority of shielding effectiveness comes from absorptive losses (Ott, 1988). When an electromagnetic wave passes through a conductive medium, its amplitude decreases exponentially as a function of the depth within that medium. The $1/e$ length constant is given by the skin depth $\delta = 2/\sqrt{\omega\mu\sigma}$, where ω is the frequency in radians/second, μ is the permeability of the metal, and σ is its conductivity (Ott, 1988). Approximately 9dB of attenuation are provided per skin-depth of shielding thickness (Ott, 1988), and since most enclosure

systems must protect against both incident (external) and emitted (internal) EMI, the shielding material must be thick enough to simultaneously absorb both without significant overlap in shield currents.

Apertures within shielding enclosures limit their effectiveness since apertures can act as slot-radiators. Particular attention should be paid to how shield apertures are positioned relative to internal cables and microstrip lines, as these have a tendency to couple strongly with nearby apertures (Matthews, 2004;Archambeault, 2002). As a general rule, the greatest linear dimension of an aperture should be limited to less than $\lambda/20$ of the offending EMI frequency (Ott, 1988). For large apertures created by input-output lines or cabling, capacitor arrays can be embedded within output connectors to create a filtered connector that essentially seals the aperture at RF frequencies.

Connections between shielded enclosures, shielded cables, and circuit ground must all be made properly to ensure adequate shielding performance. Shielded cables should terminate circumferentially onto the chassis shield, without gaps or "pig-tails," which degrade cable shield performance. The circuit ground must also be connected to the chassis shield to provide a return path for EMI radiated from components or traces. To ensure that the chassis shield is at the same potential as the circuit ground for frequencies greater than 1 MHz, the chassis shield must be connected to the circuit ground at multiple points, ideally spaced at less than $\lambda/20$ for the largest noise source (Montrose, 2000). Beyond these basic shield design principles, the shielding effectiveness obtained in practice is usually limited by leakage at seams or joints in the shielding chassis (Ott, 1988). Chassis elements must be tightly interlocking and highly conductive at seams and joints. Conductive gaskets can be used to seal joints with

surface irregularities, while sharp copper finger-stock can be used to cut past metal oxidation layers to improve contact. For laboratory research instruments with multiple modules interconnected by cables, checking the DC impedance between different points in the shielding system can help to identify poor connections between modules. As a general rule, the DC impedance measured with a voltmeter should be less than a few tenths of an ohm.

2.4. RF Safety: EEG Electrodes Influence the Specific Absorption Ratio

Tissue heating due to RF absorption during MRI presents a potential risk for patients and study subjects. The specific absorption rate (SAR) is a measure of tissue exposure to RF energy and is defined as the RF power absorbed per unit mass, in W/kg (NCRP, 1981). For an MRI study to be categorized as "non-significant risk," the FDA stipulates that SAR values must be less than 3 W/kg averaged over the entire head for a period of up to 10 minutes, and less than 8 W/kg within 1 gram of tissue for a period of up to 5 minutes. EEG electrodes have the potential to increase SAR and cause local heating or burning since the electrode wires could act as RF "antennas," channeling RF energy into the head or concentrating it into specific regions of the head or brain, as illustrated in **Figure 2.9**. Experience with electrocardiogram (ECG) recordings during clinical MRI support this concern: Since 1996 there have been numerous reports of MRI-related burns from ECG electrodes or wires used in clinical settings, usually during long-duration or high-power scanning with body-coils (FDA, 1991). Although gradient-echo fMRI sequences do not usually produce large SAR values, since the RF pulses are less powerful and less frequent compared to spin-echo sequences, many structural sequences

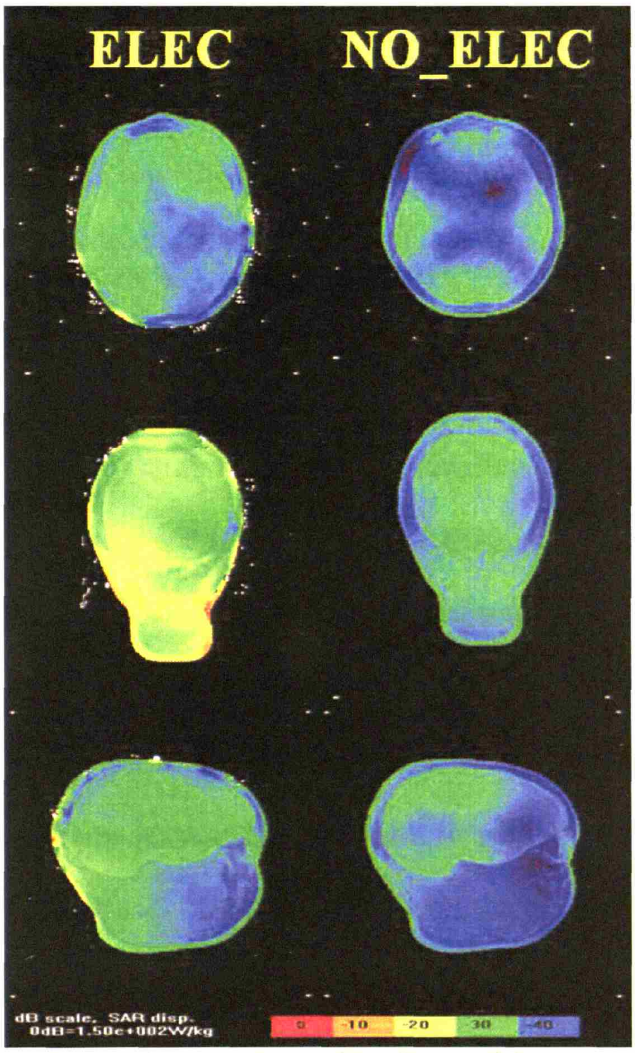

Figure 2.9. Standard (non-resistive) EEG electrodes increase SAR (left) over scans without EEG electrodes (right). (Angelone et al., 2004)

used in conjunction with fMRI do produce large SAR values. Functional MRI studies are being done at increasingly high field strengths, commonly with 3 or 4 T scanners, but with 7 and 8 T systems under development at many imaging centers throughout the world. At higher frequencies, the interaction between electrodes and SAR constitutes a greater risk, since the electrode wires are closer to the characteristic wavelength $\lambda/4$ for the system. If EEG-fMRI is to be used in clinical settings, electrode systems must be designed to withstand higher RF loads without increasing SAR, since it is difficult to predict the scanning requirements of any particular clinical case, particularly in patients with multiple medical problems. For these reasons, RF safety for EEG-fMRI is an important consideration, requiring modeling, experimental study, and design of electrode systems to limit increases in SAR.

Early work in EEG-fMRI RF-safety focused on establishing values for "current-limiting" resistors placed between the electrode body and electrode wire (Lemieux et al.,

1997) (**Figure 2.10.a**). These resistors were used to prevent RF-induced current flow from reaching the scalp for use primarily at 1.5 T, where the system frequency is approximately 64 MHz. Commercially-produced EEG-fMRI electrode caps, such as those sold by Neuroscan and Brain Products, employ these "current-limiting" resistors in the 10-20 KOhm range (Neuroscan-Compumedics, El Paso, TX; Brain Products GmbH, Munich, Germany). Unfortunately, at RF frequencies, discrete resistors behave differently than expected due to parasitic capacitances (**Figure 2.10.b**). A tiny parasitic capacitance of even 1 pF can create a short circuit at RF frequencies that can negate the effect of a current-limiting resistor. For instance, at 64 MHz (1.5 T), the impedance of a 1 pF parasitic capacitance is approximately 2.5 KOhm, but this impedance drops to 1.2 KOhm at 128 MHz (3 T) and a mere 530 Ohms at 300 MHz (7T).

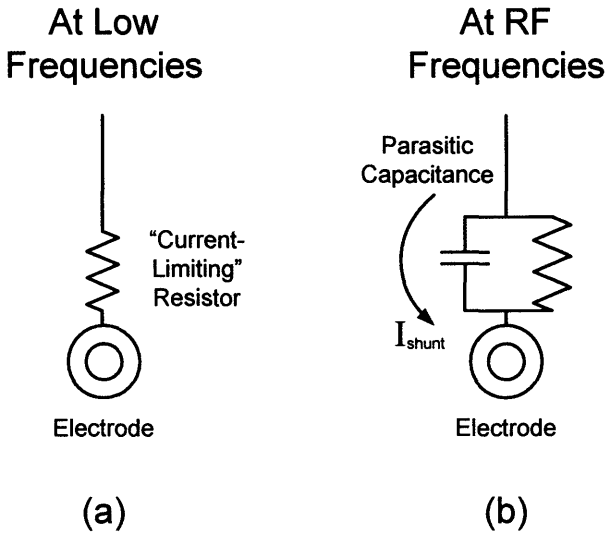

Figure 2.10. Current-limiting resistor: a) Ideal case, b) RF case. With a parasitic capacitance as low as 1 pF, the shunt impedance at 300 MHz (7T) is only 530 ohms.

While the back-of-the-envelope calculations performed above are suggestive, the RF characteristics of EEG wires and electrodes connected to the head cannot be adequately modeled with simple discrete components, since the head is an inhomogeneous conductor, with multiple tissues possessing different conductivities, and since the source and load impedances of different RF coils relative to EEG leads depend heavily upon the geometry and

layout of each component. Simulation methods are required to study this more complicated situation. The finite-difference time-domain (FDTD) method can be used to simulate electromagnetic fields from realistic computational models of the head, electrode wires, and RF coils. Angelone, et al., used this technique to estimate SAR increases due to high-density EEG montages at 3 and 7 T with both birdcage and surface coils (Angelone et al., 2004). For a 124-channel montage featuring perfectly conducting wires driven by a birdcage head coil, the peak 1 gram average SAR was found to increase by a factor of 61.62 at 3 T and 172.32 at 7 T. These increases were more modest when using a surface coil, with 15-fold increases for both 3 and 7 T. Fortunately, for both coils these increases were localized to hot spots on the skin, rather than the brain parenchyma, suggesting that heating and burning risk is greatest at the scalp. Lower-density EEG montages produced smaller SAR increases, but with a similar order of magnitude (e.g., a factor of 120 increase at 7 T with 31 electrodes).

Follow on studies using the same techniques suggest that discrete current-limiting resistors do not protect against SAR increases, while resistive wires whose resistance is distributed evenly across the length of EEG leads can bring SAR levels back to nominal levels (Angelone and Bonmassar, 2004;Vasios et al., 2005). A 31-channel EEG montage featuring 10 KOhm resistors at each electrode, driven by a surface coil at 7T, showed a 13.4-fold increase in peak 1-gram averaged SAR (Angelone and Bonmassar, 2004), slightly higher than EEG electrodes without the 10 KOhm resistors (Angelone et al., 2004). However, when resistive wires with a modest resistance of 166 Ohms/meter were used, equivalent to commercially-available carbon-fiber wires, the peak 1-gram averaged SAR increased only by a factor of 1.32. Use of discrete resistors in combination with

resistive leads did not influence the SAR. By using wires with higher levels of distributed resistance, the SAR observed under simulation could be brought down to nominal levels, as if the wires were not present at all (Vasios et al., 2005).

These studies highlight the need for careful attention to RF safety, particularly at higher field strengths such as 3 or 7 T. With use of appropriate materials, such as resistive carbon fiber wires, SAR levels can be brought close to nominal levels, and further research with simulation tools such as the FDTD methods described above could yield electrode montages with even better SAR performance. The use of discrete current-limiting resistors offers little or no protection against SAR increases. To provide an additional safety factor, high-power sequences should be avoided during EEG-fMRI studies.

2.5. Summary and Conclusions

1. EEG-fMRI acquisition hardware should be designed to have: 1) small loop sizes prior to analog-to-digital conversion (ADC), 2) high dynamic range, achieved through lower front-end amplifier gain and/or higher ADC bit-resolution, and 3) either high-rate EEG sampling or sampling that is synchronized to the acquisition clocks that control gradient switching.

2. EEG-fMRI hardware must be designed with electromagnetic compatibility in mind, starting at the circuit and PCB level, integrating digital circuits, analog circuits, and shielding systems to limit electromagnetic interference.

3. Standard EEG electrodes pose a safety risk by increasing the SAR of RF energy during imaging, particularly at higher field strengths such as 3 or 7 Tesla. The industry-

standard use of discrete current-limiting resistors offers little or no protection against SAR increases. EEG leads with distributed resistance can reduce the SAR to nominal levels, as if the EEG leads were not present at all.

2.6. References

1. Allen PJ, Josephs O, Turner R (2000) A method for removing imaging artifact from continuous EEG recorded during functional MRI. Neuroimage 12: 230-239.

2. Allen PJ, Polizzi G, Krakow K, Fish DR, Lemieux L (1998) Identification of EEG events in the MR scanner: the problem of pulse artifact and a method for its subtraction. Neuroimage 8: 229-239.

3. Anami K, Mori T, Tanaka F, Kawagoe Y, Okamoto J, Yarita M, Ohnishi T, Yumoto M, Matsuda H, Saitoh O (2003) Stepping stone sampling for retrieving artifact-free electroencephalogram during functional magnetic resonance imaging. Neuroimage 19: 281-295.

4. Angelone, L. M. and Bonmassar, G. Use of resistances and resistive leads: Implications on computed electric field and SAR values. Proc.12th ISMRM , 1652. 2004.

5. Angelone LM, Potthast A, Segonne F, Iwaki S, Belliveau JW, Bonmassar G (2004) Metallic electrodes and leads in simultaneous EEG-MRI: specific absorption rate (SAR) simulation studies. Bioelectromagnetics 25: 285-295.

6. Archambeault BR (2002) PCB Design for Real-World EMI Control. Boston: Kluwer Academic Publishers.

7. Bonmassar G, Anami K, Ives J, Belliveau JW (1999) Visual evoked potential (VEP) measured by simultaneous 64-channel EEG and 3T fMRI. Neuroreport 10: 1893-1897.

8. Bonmassar G, Purdon PL, Jaaskelainen IP, Solo V, Brown EN, Belliveau JW (2001a) Motion and ballistocardiogram artifact removal for interleaved recording of EEG and ERP during MRI. Neuroimage (in press).

9. Bonmassar G, Schwartz DP, Liu AK, Kwong KK, Dale AM, Belliveau JW (2001b) Spatiotemporal brain imaging of visual-evoked activity using interleaved EEG and fMRI recordings. Neuroimage 13: 1035-1043.

10. Colletti PM (2004) Size "H" oxygen cylinder: accidental MR projectile at 1.5 Tesla. J Magn Reson Imaging 19: 141-143.

11. FDA. Manufacturer and User Facility Device Experience Database - (MAUDE). 1991. U.S. Food and Drug Administration.

12. Garreffa G, Bianciardi M, Hagberg GE, Macaluso E, Marciani MG, Maraviglia B, Abbafati M, Carni M, Bruni I, Bianchi L (2004) Simultaneous EEG-fMRI acquisition: how far is it from being a standardized technique? Magn Reson Imaging 22: 1445-1455.

13. Garreffa G, Carni M, Gualniera G, Ricci GB, Bozzao L, De Carli D, Morasso P, Pantano P, Colonnese C, Roma V, Maraviglia B (2003) Real-time MR artifacts filtering during continuous EEG/fMRI acquisition. Magn Reson Imaging 21: 1175-1189.

14. Goldman RI, Stern JM, Engel J, Jr., Cohen MS (2000) Acquiring simultaneous EEG and functional MRI. Clin Neurophysiol 111: 1974-1980.

15. Huang-Hellinger FR, Breiter HC, McCormack G, Cohen MS, Kwong KK, Sutton JP, Savoy RL, Weisskoff RM, Davis TL, Baker JR, Belliveau JW, Rosen BR (1995) Simultaneous functional magnetic resonance imaging and electrophysiological recording. Hum Brain Mapp 3: 13-23.

16. Ives JR, Warach S, Schmitt F, Edelman RR, Schomer DL (1993) Monitoring the patient's EEG during echo planar MRI. Electroencephalogr Clin Neurophysiol 87: 417-420.

17. Laufs H, Kleinschmidt A, Beyerle A, Eger E, Salek-Haddadi A, Preibisch C, Krakow K (2003a) EEG-correlated fMRI of human alpha activity. Neuroimage 19: 1463-1476.

18. Laufs H, Krakow K, Sterzer P, Eger E, Beyerle A, Salek-Haddadi A, Kleinschmidt A (2003b) Electroencephalographic signatures of attentional and cognitive default modes in spontaneous brain activity fluctuations at rest. Proc Natl Acad Sci U S A 100: 11053-11058.

19. Lemieux L, Allen PJ, Franconi F, Symms MR, Fish DR (1997) Recording of EEG during fMRI experiments: patient safety. Magn Reson Med 38: 943-952.

20. Lemieux L, Salek-Haddadi A, Josephs O, Allen P, Toms N, Scott C, Krakow K, Turner R, Fish DR (2001) Event-related fMRI with simultaneous and continuous EEG: description of the method and initial case report. Neuroimage 14: 780-787.

21. Liebenthal E, Ellingson ML, Spanaki MV, Prieto TE, Ropella KM, Binder JR (2003) Simultaneous ERP and fMRI of the auditory cortex in a passive oddball paradigm. Neuroimage 19: 1395-1404.

22. Makeig S, Westerfield M, Jung TP, Enghoff S, Townsend J, Courchesne E, Sejnowski TJ (2002) Dynamic brain sources of visual evoked responses. Science 295: 690-694.

23. Matthews, R. PCB Design for the Mitigation of EMI. 2004. Noise Doctors, Inc.

24. Mirsattari SM, Ives JR, Bihari F, Leung LS, Menon RS, Bartha R (2005) Real-time display of artifact-free electroencephalography during functional magnetic resonance imaging and magnetic resonance spectroscopy in an animal model of epilepsy. Magn Reson Med 53: 456-464.

25. Montrose MI (2000) EMC and Printed Circuit Board Design. In: The Electronic Packaging Handbook (Blackwell GR, ed), Boca Raton: CRC Press.

26. NCRP. Radiofrequency Electromagnetic Fields: Properties, Quantities and Units, Biophysical Interaction, and Measurements. 67. 1981. Bethesda, MD, National Council for Radiation Protection and Measurement.

27. Ott HW (1988) Noise Reduction Techniques in Electronic Systems. New York: John Wiley and Sons.

28. Shellock FG, Crues JV, III (2002) MR Safety and the American College of Radiology White Paper. AJR Am J Roentgenol 178: 1349-1352.

29. Vaidyanathan PP (1993) Multirate Systems and Filter Banks. Englewood Cliffs: Prentice Hall.

30. Vasios, C. E., Angelone, L. M., Purdon, P., Belliveau, J. W., and Bonmassar, G. EEG measurements at 7T Tesla using the ink cap. 13th ISMRM (submitted) . 2005.

Chapter 3
Design and Implementation of Hardware and Software Systems for EEG-fMRI

3.1. Introduction

In this chapter we describe the design and implementation of a hardware and software system for recording EEG during fMRI. The elements of this system include: 1) An EEG amplification and analog-to-digital conversion system featuring low-noise and high-dyanamic range that is electromagnetically compatible for use within the MRI; 2) A computer hardware and software platform for EEG data acquisition that integrates EEG recordings with external signals such as event triggers and physiological monitoring, with a user-expandable software platform offering the capability to do real-time EEG signal processing; 3) An EEG electrode system that reduces MRI-related noise coupling and radio-frequency (RF) specific absorption rate (SAR) relative to conventional EEG electrodes; 4) A stimulus delivery system integrated with the EEG acquisition system featuring an MRI-compatible headphone system offering passive noise protection, high frequency response, and compatibility with ERP recordings. This system is fully compatible with 7 T MRI systems and can also be used for high-speed electrophysiological recordings with minor adjustments to the data acquisition software

and the addition of a pre-amplifier buffer system. We describe the design and implementation of each component below.

3.2. An EEG Amplification and Analog-to-Digital Conversion (ADC) System for Use during MRI

In this section we describe an amplification and analog-to-digital conversion system for EEG-fMRI. This system is designed to have *high dynamic range* to prevent saturation from gradient-induced artifacts during MRI, with a *frequency response down to DC* to allow for a fast recovery after MRI image acquisition. *ADC is performed in close proximity to the MRI bore* to limit the loop size of electrode leads and amplifier cables, reducing environmental noise coupling from the static and gradient magnetic fields as well as RF-related increases in SAR.

3.2.1. First Stage Amplification

The first-stage amplification system was built around the Linear Technology LT1167 instrumentation amplifier (Linear Technology Corporation, Milpitas, CA), which possess a number of features particularly appropriate for the EEG-fMRI application. Its low gain nonlinearity (<10ppm), high bandwidth (120 kHz with gain of 100), wide power supply range (V_S = +/-18V) and output range (within 1.3V of V_S), allow for a high dynamic range (Linear Technology Corporation, 1998). Its low input bias current of <320pA allows for direct coupling to the source without the use of input bias resistors that reduce input impedance, facilitating the use of higher-impedance EEG electrode systems designed to reduce SAR. The LT1167 is also well-suited for reducing RF and gradient-induced noise coupling with its high common-mode rejection-ratio (CMMR;

>120 dB for gain of 100) and power-supply rejection-ratio (PSRR; >131 dB for gain of 100). Its availability in a small-outline integrated circuit package (SOIC; 3.9 X 4.9 mm) facilitates a compact PCB layout with small loop sizes to reduce RF and gradient pickup.

The LT1167 was used to provide 32 channels of EEG amplification, with a gain of 50, a power supply of +/-10V, and output coupling resistor of 3.6 kOhm, to provide a 4-kHz first-order low-pass pole when coupled to the 70nF filter capacitors at the input to the ADC unit (to be discussed in Section 3.2.3), as illustrated in **Figure 3.1**. Traditional AC-coupling capacitors were omitted to provide frequency response down to DC, and DC-coupling bias resistors were omitted to make full use of the amplifier CMMR. The amplifiers were laid out as four 8-channel modules on a double-sided four-layer PCB. The amplifiers received input from EEG electrodes via a custom-made filtered 21-pin micro-D connector, and amplifier outputs were connected to the ADC unit using a

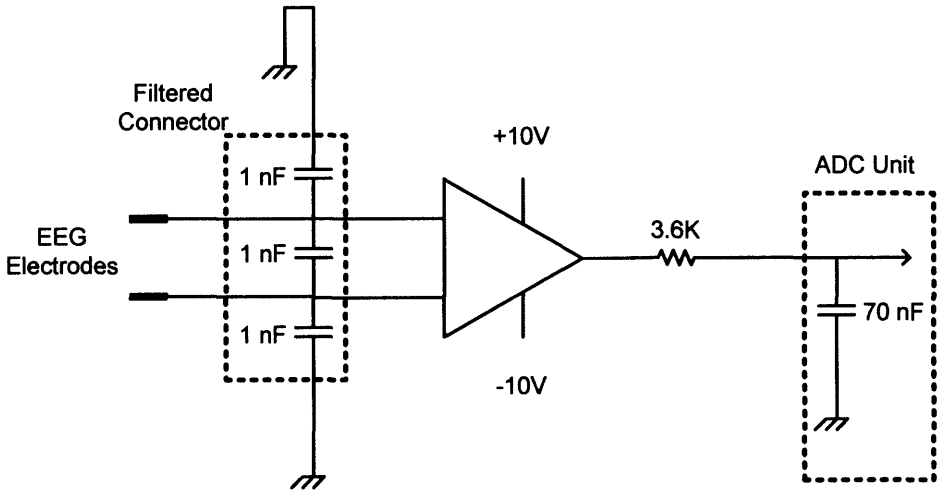

Figure 3.1. First-stage amplifier circuit, illustrating input filtered capacitor array, chassis connections, and output resistor interaction with feed-through capacitor in ADC unit.

double-shielded micro-D cable (to be described below in Section 3.2.3).

3.2.2. Analog-to-Digital Conversion

The analog-to-digital converter unit was designed to operate in close proximity to the MRI bore to reduce RF and gradient noise coupling, with high dynamic range to prevent saturation and facilitate removal of MRI-related EEG artifacts. While amplifier circuits possessing high CMRR and PSRR can function properly in the presence of RF and gradient-induced noise, ADC components contain sample-and-hold elements that behave as floating capacitors, rendering them sensitive to fluctuating magnetic fields that cannot be shielded. To balance the trade-off between low noise coupling from EEG/amplifier leads and ADC sensitivity to the gradients, we designed the ADC unit to operate just outside the MRI bore, connecting it to the amplifier system with a long shielded cable as described above. Communication and data transmission with external computers was accomplished by way of digital optical communications, which transmitted both EEG data and the scan clock used to sample the data. This scan clock ("SYNC") was used to synchronize EEG acquisition with external signals such as event triggers or physiological data. The ADC process was controlled by a digital signal processing (DSP) microcontroller, which manages the ADC timing and data transfer to the optical communications hardware. These elements are illustrated in **Figure 3.2**.

To achieve high dynamic range, we selected the Burr-Brown ADS1254 ADC, a low-power, low-noise, high-speed ADC with 24-bit resolution (Burr-Brown, a division of Texas instruments, Dallas, TX). Each ADS1254 chip has four differential inputs, which can be multiplexed at a rate of up to 1 kHz per channel when operated with a system clock rate of 8 MHz (Burr-Brown Products, 2001). Alternatively, a single channel can be

sampled at up to 20 kHz. To provide 32 channels of EEG, an architecture using 8 ADS1254's was chosen, each running with 4-channel multiplexing at 1 kHz. If higher-rate sampling were required, a single channel from each ADS1254 could be sampled, giving 8 channels at 20 kHz per channel. The ADS1254 chips were controlled by an SX48 DSP unit (Ubicom, Inc., Mountain View, CA) running at 48 MHz. To reduce RF noise coupling to the analog input stages of the ADC system, clock timing was provided by a single 48 MHz clock driving a programmable divide-by-six counter (DS1075; Dallas Semiconductor, a subsidiary of Maxim Integrated Products, Dallas, TX), which provided the 8 MHz clock for the ADS1254. The analog input to each ADS1254 unit was first anti-alias filtered and then re-scaled to a 0-to-5V reference range using an op-amp-based scaling and level-shift circuit recommended in the ADS1254 datasheet (Burr-Brown Products, 2001). Low-pass anti-aliasing filtration was provided by a one-pole RC divider

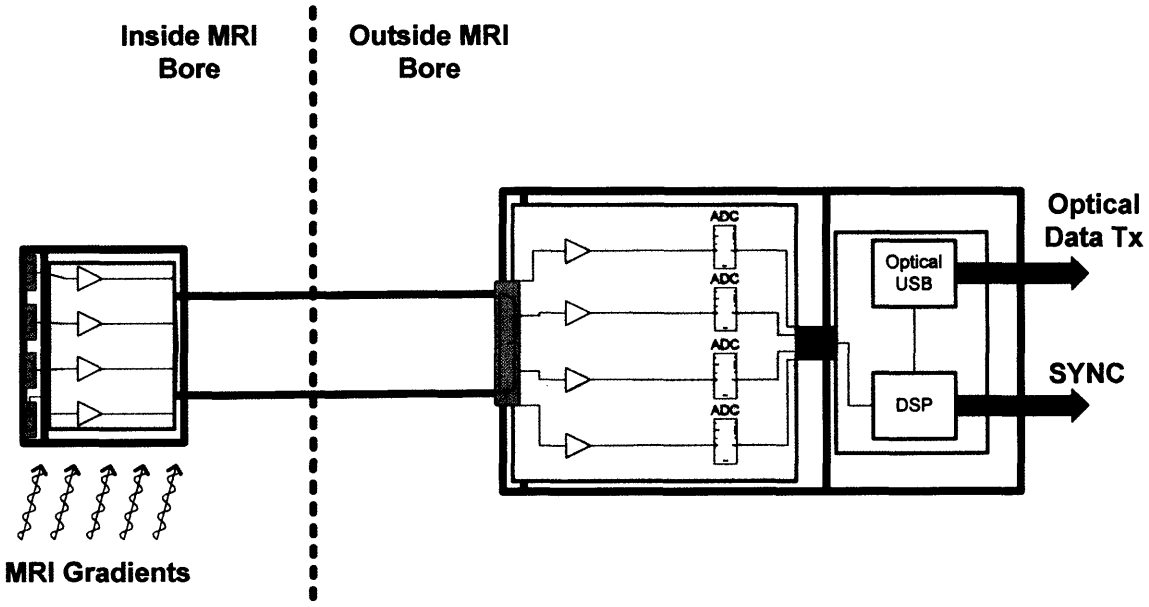

Figure 3.2. Layout of amplifier and ADC units relative to MRI bore. The amplifier is located within the bore, close to the head coil, to minimize inductive noise coupling through electrode lead wires. The ADC unit is located farther from the MRI bore to reduce the influence of the gradients on its more sensitive sample-and-hold elements.

whose capacitance was user-selectable via a transistor switch system controlled by the SX64 to provide a cutoff frequency of either 12 or 24 kHz. Two forms of optical communication are provided by the system. The first is a universal serial bus (USB) optical link that is used to control the acquisition device and to transmit the sampled EEG data. This is provided by the combination of a USB interface module (DLP-USB245M; DLP Design, Allen, TX) integrated into the ADC system circuit, which is then connected to an optical USB extension cable (Opticis M2-100; Opticis North America Ltd., Richmond Hill, Ontario, Canada). The second is a high-speed optical line (Agilent HFBR-1521; Agilent Technologies, Palo Alto, CA) that is driven by the channel selection portion of the SX48 processor, providing one clock pulse for every 8 channels sampled (4 kHz in 32 channel mode, 20 kHz in 8 channel mode), providing a synchronization (SYNC) signal for external signals such as event triggers and physiological recordings with the EEG. A block-diagram for these system components is provided in **Figure 3.3**.

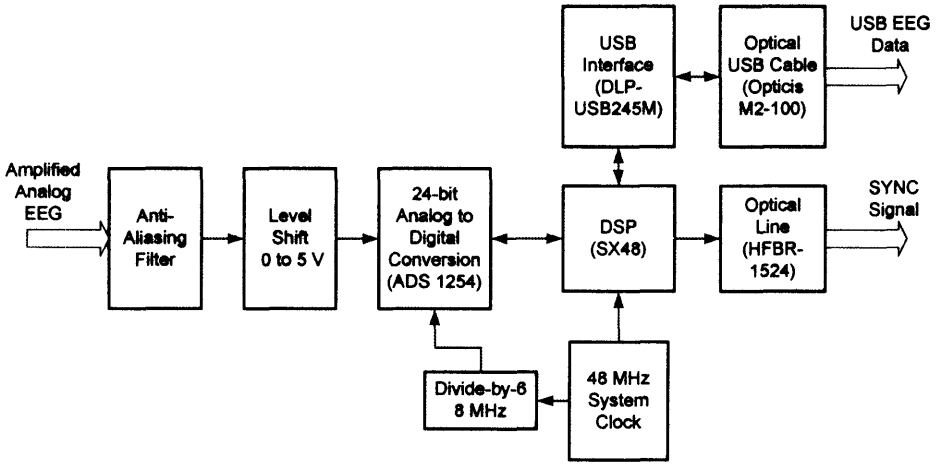

Figure 3.3. Detailed block diagram of ADC system components.

The PCB layout for the ADC unit is divided into three isolation zones organized according to power requirements and noise sensitivity (**Figure 3.4**): 1) A 5V digital zone

supporting the SX64, USB, Versatile Link, and digital clock modules; 2) A 3.3V digital zone supporting the ADS1254 ADC chips; and 3) A 5V analog zone supporting the scaling and level-shift modules, and supplying +/-10V power for the amplifier system. Power was provided by a pair of 18A-h 12-V lead acid batteries (TR18-12; Tempest Battery Manufacturing Company, Ltd., Campbell, CA) connected in series and center-tapped to provide +12V, GND (center tap), and -12V terminals. A pair of Schottky diodes were used to provide accidental reverse battery protection (International Rectifier 20L15TS, International Rectifier, El Segundo, CA). PCB layout, DSP programming, DLP interface programming, and board population were performed by TechEn, Inc. (Milton, MA).

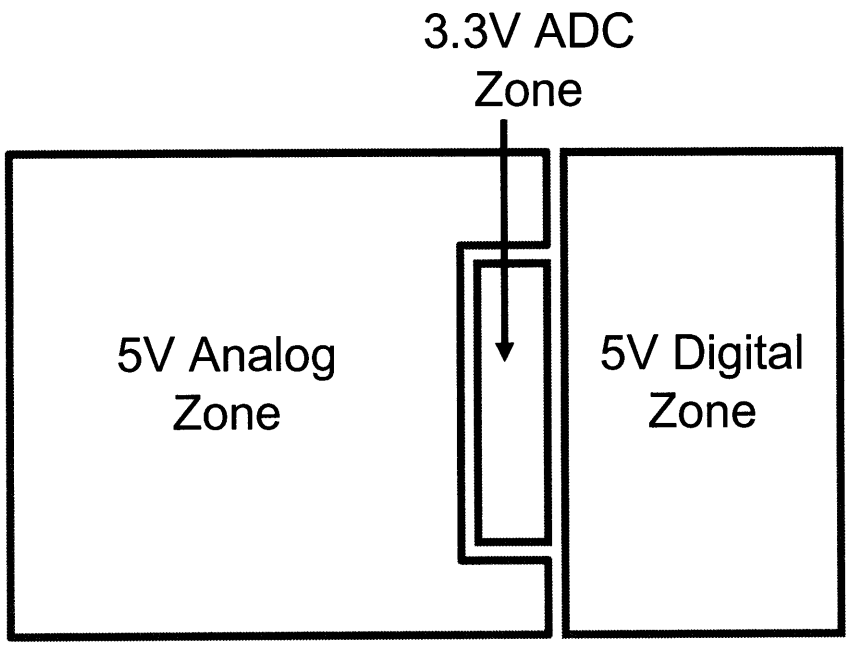

Figure 3.4. Isolation zones for PCB layout of ADC unit.

3.2.3. Shielding and Grounding for Electromagnetic Compatibility

A shielding and grounding system was constructed to achieve electromagnetic compatibility for MRI. The primary objectives were to: 1) Design and construct chassis

elements to provide circumferential contact and conductivity at all chassis seams or interconnects, in order to minimize slot radiators; 2) Use filtered interconnects to provide RF attenuation for all input-output lines; and 3) Make multiple low-impedance connections between the chassis and circuit "grounds," in order to provide low impedance return paths for RF currents radiated from digital components or PCB traces.

Plastic enclosures were chosen for the amplifier and ADC units to fit the required PCB and external connector dimensions (Pactec LH-64-130 for amplifier unit, CM-69-240 for ADC unit; Pactec, Inc., Concordville, PA). The internal surfaces of the enclosures were coated with aluminum using a vacuum deposition technique giving a coating thickness of approximately 100 microns (Vacuum Technologies Inc., Reedsburg, WI), with care taken to coat the interlocking flanges of each chassis piece to ensure electrical contact. An important mechanical feature of these enclosure models was the

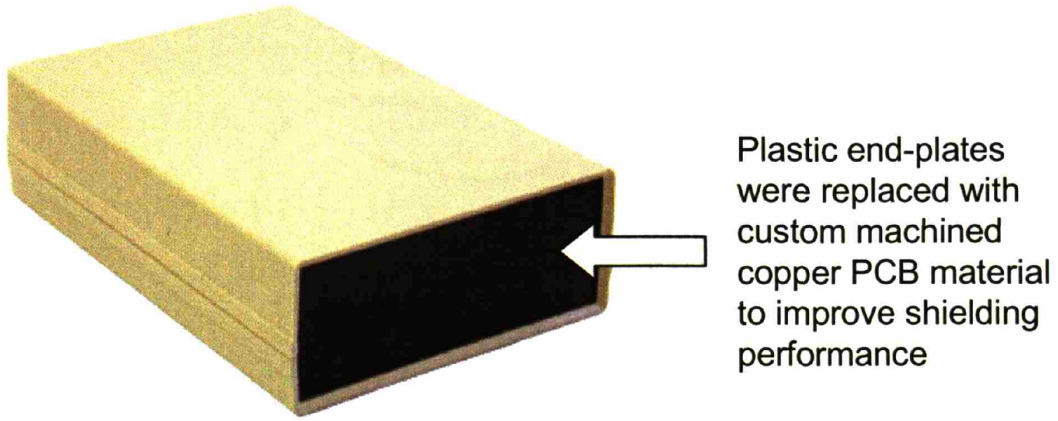

Figure 3.5. Plastic chassis for ADC unit, illustrating chassis end-plates that were replaced with precision-cut copper-clad plates described in Appendix 3A.1. The internal surfaces of both chassis were vacuum deposited with 100 micron aluminum (Vacuum Technologies Incorporated, Reedsburg, WI), with care taken to coat all interlocking surfaces to ensure good contact and eliminate slot radiators. The amplifier chassis was constructed using similar materials and methods.

use of flat "endplates" for input-output connector attachment (**Figure 3.5**). The supplied plastic endplates were replaced with custom-made endplates designed to improve electrical contact with the rest of the chassis shell, and to provide precise circumferential contact with input-output connectors. Construction details for these custom-made endplates are provided in **Appendix 3A.1.** The ADC unit's digital ground was connected to the chassis at the battery input terminal, while its analog ground was connected near the EEG input-output lines and the +/-10V regulators (**Figure 3A.1.c**). The shielded chassis for the amplifier unit was constructed using materials and methods identical to those used for the ADC unit, but with a different filtered interconnect system. In particular, each 8-channel amplifier module was coupled to EEG electrodes using hand-made 21-pin filtered micro-D connectors featuring 1nF capacitor arrays. The amplifier analog ground was terminated to the amplifier chassis at each of the filter-connector's ground pins. Construction details for the micro-D filtered connector are provided in **Appendix 3A.1**.

The 32-EEG channel outputs were connected to the ADC unit using a non-ferromagnetic 9-foot 37-pin micro-D double-shielded cable featuring circumferentially-conductive backshells and circumferential termination to cable shields (Glenair 177-225; Glenair, Glendale, CA). At 9-feet, this cable is long enough to reach from the head coil to the bore edge in most MRI systems, including the Siemens Allegra 3T, Siemens Trio 3T, and Siemens Magnetom 7T. Like the ADC unit, connector holes in the conductive panels of the amplifier chassis were precision cut using the T-Tech QuickCircuit-7000 (T-Tech, Norcross, GA) to provide circumferential contact and conductivity for each connector. Cable-to-chassis connections were made robust by using jackpost and screw

connections. In practice, DC impedance from the EEG connector shell to the ADC battery GND terminal was approximately 0.2 to 0.3 ohms when measured with a standard voltmeter.

3.2.4. System Performance

The LT1167-based amplifier system described above, with its gain of 50, its +/-10V power supply, and its output range of –VS+1.2 to VS-1.3 V, provides a dynamic range of -176 to +174 mV. The ADS1245 provides a 19-bit RMS effective resolution due to inherent noise within the integrated circuit, offering an effective resolution of 0.76uV in the least significant bit (LSB), given an amplifier gain of 50 and an amplifier output range of +/-10V. Typical traces are shown in both time and frequency domain, recorded in a shielded room with a 10Hz, ~10uV input signal provided by a function generator (**Figure 3.6.a**) and under quiescent conditions with all amplifier channels shorted to ground (**Figure 3.6.b**). The RMS noise calculated from the quiescent recordings was approximately 0.1517 $uV/Hz^{1/2}$ (bandwidth from 0 to 475 Hz, averaged across all channels). The recovery speed of the amplifier system during MRI is evident from **Figure 3.7**, which compares a traditional AC-coupled high-gain amplification system (Ives et al., 1993;Mirsattari et al., 2005) during EPI with the present system. **Figure 3.8** illustrates the effectiveness of the shielded enclosure system. During one recording session, the cover to the ADC chassis was removed during imaging (middle column of **Figure 3.8**), resulting in poor image quality compared to images without EEG (left column of **Figure 3.8**). In a separate imaging session, with the shielding system in place, image noise levels are at nominal levels (right column of **Figure 3.8.b**).

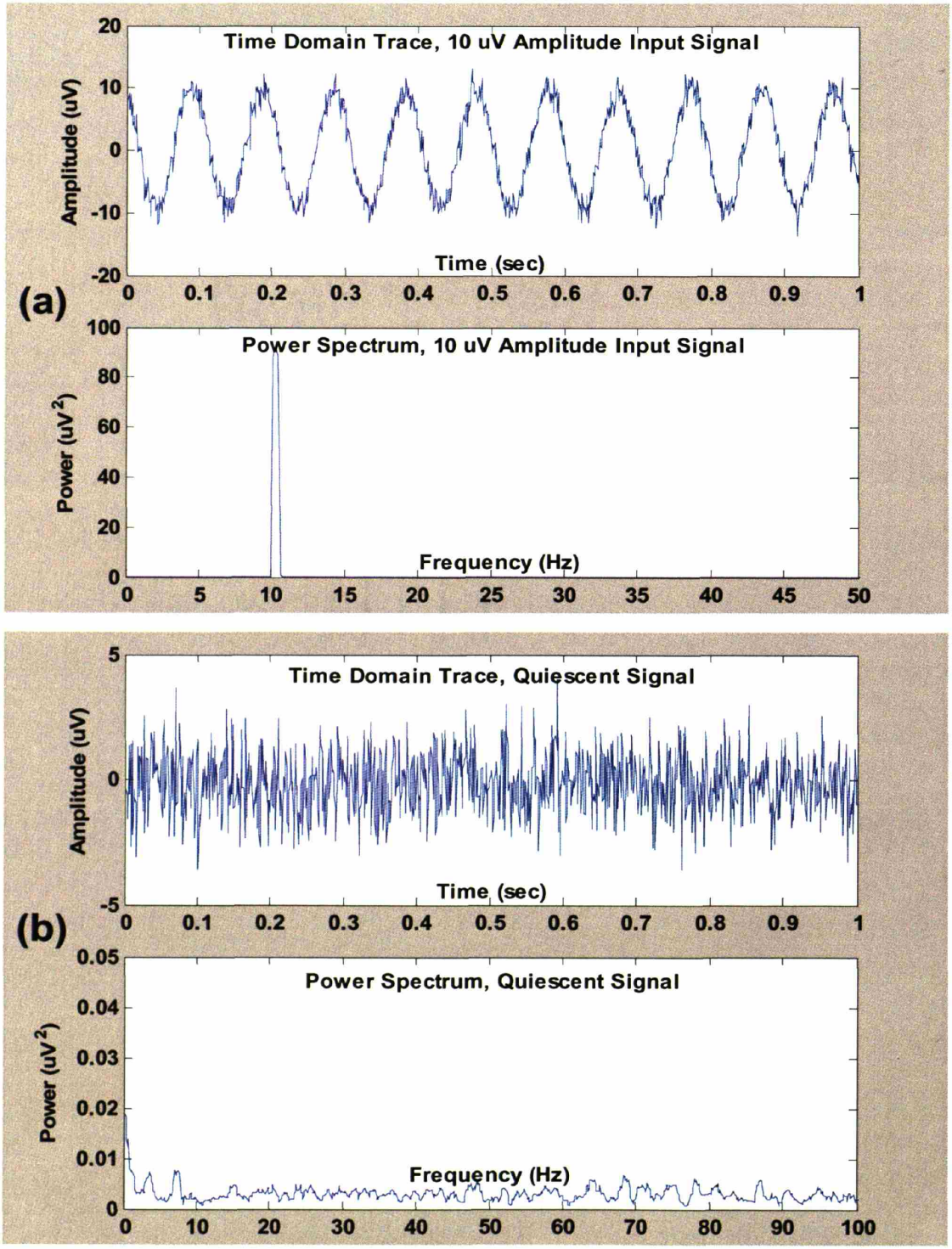

Figure 3.6. Typical recording traces for EEG-fMRI amplification and ADC units: (a) Driven by function generator with 10Hz, ~10uV signal; (b) Quiescent signals with input grounded.

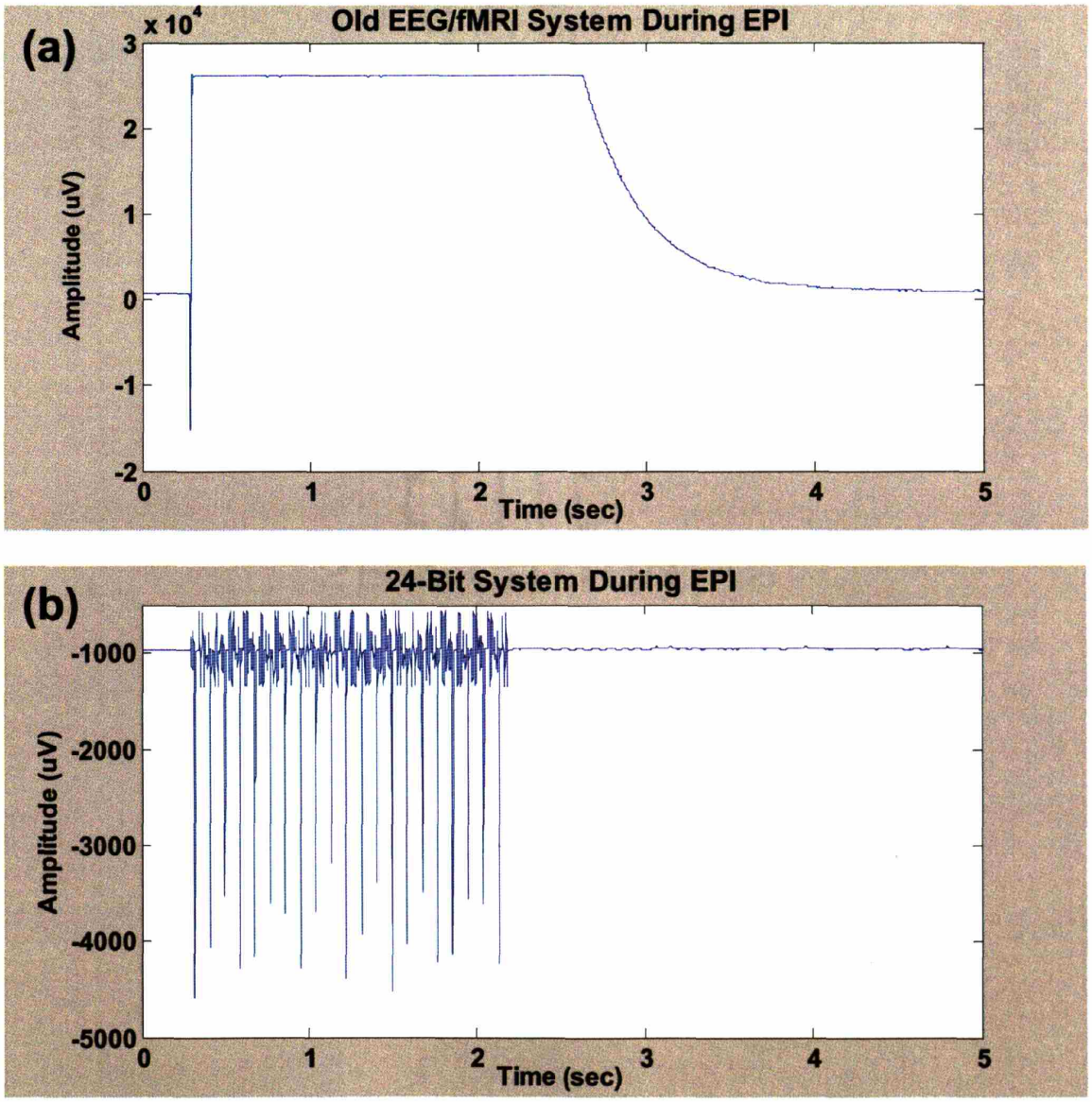

Figure 3.7. Amplifer recovery: (a) Traditional high-gain amplification system with AC-coupled input; (b) Low-gain DC amplifier.

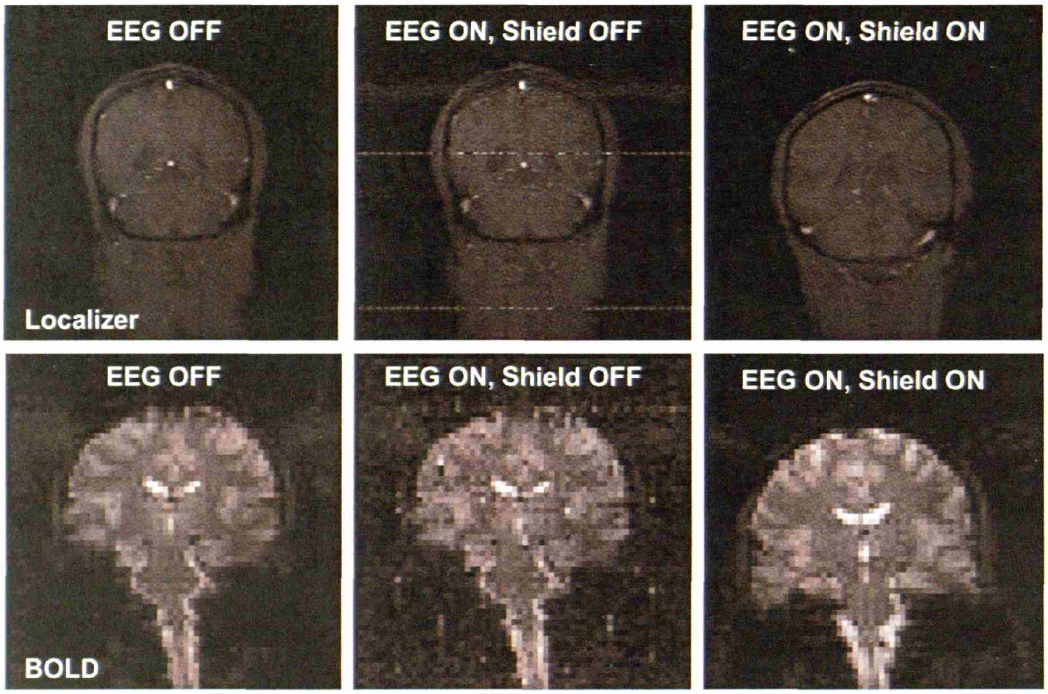

Figure 3.8. Image quality without (center) and with (right) RF shielding system.

3.3. Data Acquisition, External Signal Integration, and Real-Time Signal Processing

In this section we describe a computer hardware and software system for EEG acquisition, integration with external signals, graphical display, and real-time signal processing.

3.3.1. Acquisition and Integration of EEG with External Signals

In many EEG-fMRI applications, acquisition of external signals time-locked to the EEG signal is required. For instance, ERP studies require event triggers to mark when different stimuli are presented, while drug studies may require simultaneous physiological monitoring. We have devised a laptop-based data acquisition and integration architecture that draws EEG data from the USB interface, and either digital or

analog external signals from the PCMCIA bus, time-locked to the USB interface by way of the SYNC signal discussed in Section 3.2.2 (**Figure 3.9**). The USB EEG interface is based on the FTDI FT245BM chipset used in the DLP USB module (Future Technology Devices International, Ltd., Glasgow, Scotland, UK; DLP Design, Inc., Allen, TX). A National Instruments DAQCard 6533 high-speed 32-bit parallel digital I/O interface card is used for digital external signals such as event triggers, while a National Instruments DAQCard 6024E high-speed 12-bit analog acquisition card is used for analog acquisitions such as physiological monitoring (National Instruments, Austin, TX). Digital trigger information can be recorded on the 6024E interface by supplying individual trigger lines to one or more of the analog inputs. Acquisition of the external signals is clocked by the EEG-fMRI ADC unit's optical SYNC line through an Agilent Versatile Link receiver (Agilent HFBR-2521, Agilent, Palo Alto, CA). A detailed description of interconnects required for both setups is provided in **Appendix 3A.2**.

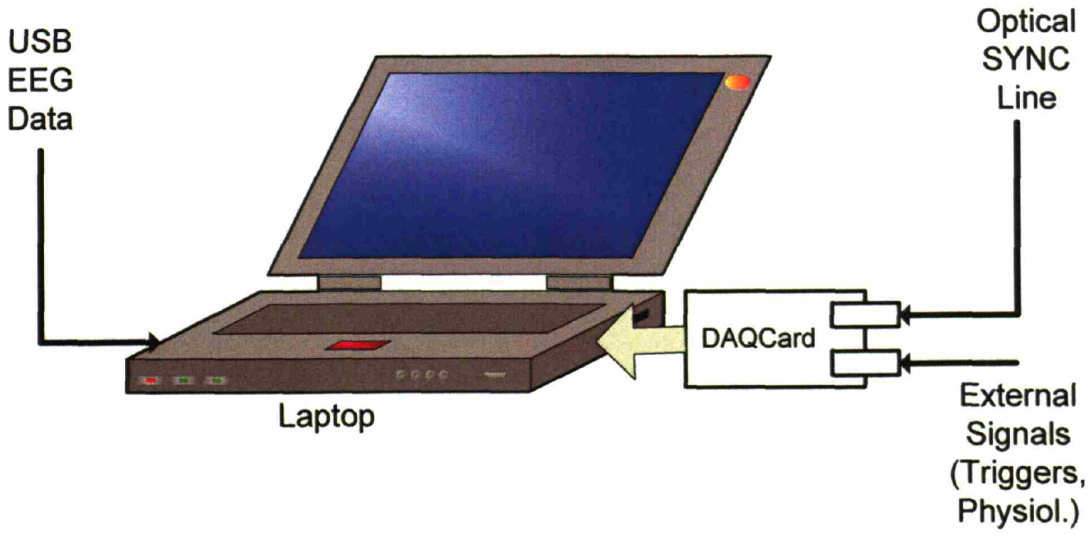

Figure 3.9. Block diagram of data acquisition and external signal integration architecture.

3.3.2. Data acquisition software for display, recording, and real-time signal processing

The National Instruments (NI) LabView software development platform (National Instruments, Austin, TX), running within the Microsoft Windows 2000 operating system (Microsoft, Richmond, WA), was used to develop the data acquisition (DAQ) software for this application. LabView is a high-level graphical programming language featuring a wide assortment of built-in data-acquisition, hardware interface, data display, and data analysis functions to speed software development. The LabView development environment offers seamless integration with DAQ devices, either with built-in interfaces for National Instruments data acquisition cards, or with user-programmed DLL's to interface with custom or 3rd party devices. Its modular graphical development system allows for rapid revision and inclusion of new functions, reducing software development cycles. DAQ programs are constructed as "virtual instruments" (VIs) controlled through an intuitive push-button graphical user interface, making the programs easily accessible to a wide range of end-users. Even with these graphical and hardware-integration conveniences, its features are sufficiently rich to retain the control, modularity, flexibility, and processing speed of traditional text-based languages.

DAQ applications in LabView can be constructed using a variety of interface functions spanning a range from high-level functions offering immediate implementation but minimal control, to low-level functions offering a high degree of control but greater development complexity. The data integration architecture described in Section 3.3.1 calls for two buffered data acquisition to run simultaneously: One buffered acquisition process for either the DAQCard 6533 or 6024E, and another for the USB-based EEG

ADC unit. In LabView Versions 6i through 7.1, buffered data acquisitions can be handled through a combination of built-in intermediate-level DAQ functions to configure, start, read, and clear the acquisition, arranged within a while-loop structure (Bishop, 2001). These intermediate-level DAQ functions offer control over acquisition timing, data size, trigger sources, and buffer sizes, among other details, but can be implemented easily within a single VI. **Figure 3.10** illustrates simple digital and analog buffered acquisitions using these intermediate-level DAQ functions. **Table 3.1** provides an overview of each of these intermediate-level DAQ functions. To integrate the USB EEG acquisition within this control structure, the USB DAQ commands were interfaced with LabView according to this intermediate-level VI formalism. In this way, the USB EEG acquisition could be run in parallel with the digital or analog acquisition using the

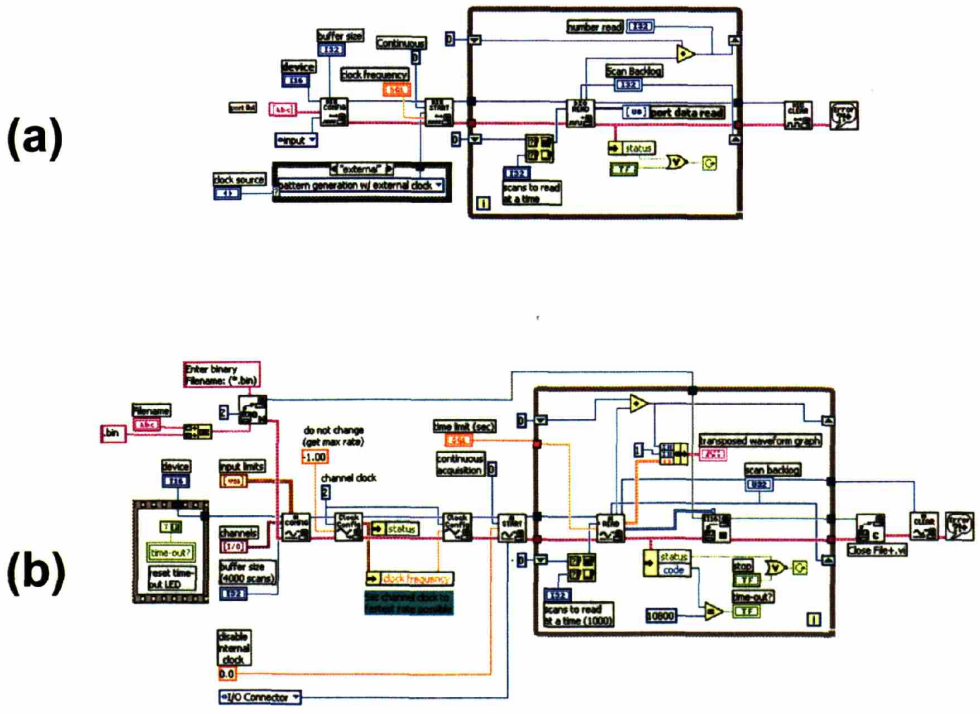

Figure 3.10. Block diagram for basic buffered acquisition LabView VI: (a) Digital buffered acquisition; (b) Analog buffered acquisition.

same while-loop control structure. **Appendix 3A.3** contains a detailed discussion of each of these USB EEG acquisition VI's and their underlying USB DLL commands.

Function Name	Description and Features
NI Intermediate-Level Digital DAQ	
DIO Config	Set Buffer size, device number, port list, group direction (input, output, or both), handshaking parameters
DIO Start	Set number of scans to acquire or continuous, clock/handshake source, clock frequency
DIO Read	Buffered acquisition, tracking scan backlog, providing data output for display, file writing, and analysis
DIO Clear	Terminates acquisition
NI Intermediate-Level Analog DAQ	
AI Config	Sets channel timing, number of channels, input coupling info, input limits, device number, channels, buffer size, group number, number of buffers
AI Start	Sets trigger type, edge or slope trigger, pretrigger scans, number of scans to acquire or continuous, scan rate, scan clock source, analog trigger settings
AI Read	Buffered acquisition, tracking scan backlog, providing data output in multiple formats for display, file writing, and analysis
AI Clear	Terminates acquisition
USB EEG Interface	
AI Config 24Bits	Sets multiplexing mode (8 channels or 32 channels), channel number, anti-aliasing filter setting (12 or 24 kHz), and memory location in SX48 for storing configuration ("bank" number, similar in concept to "Process ID")
AI Start 24Bits	Sets configuration "bank," number of scans to acquire or continuous
AI Read 24Bits	Buffered acquisition, reads FIFO when data are present, data output converted to 4(time) x 32(channel) matrix in signed 32-bit integer (I32) for display, file writing, and analysis.
AI Clear 24Bits	Terminates acquisition

Table 3.1. Overview of Intermediate-Level DAQ Functions for Digital, Analog, and USB EEG acquisitions.

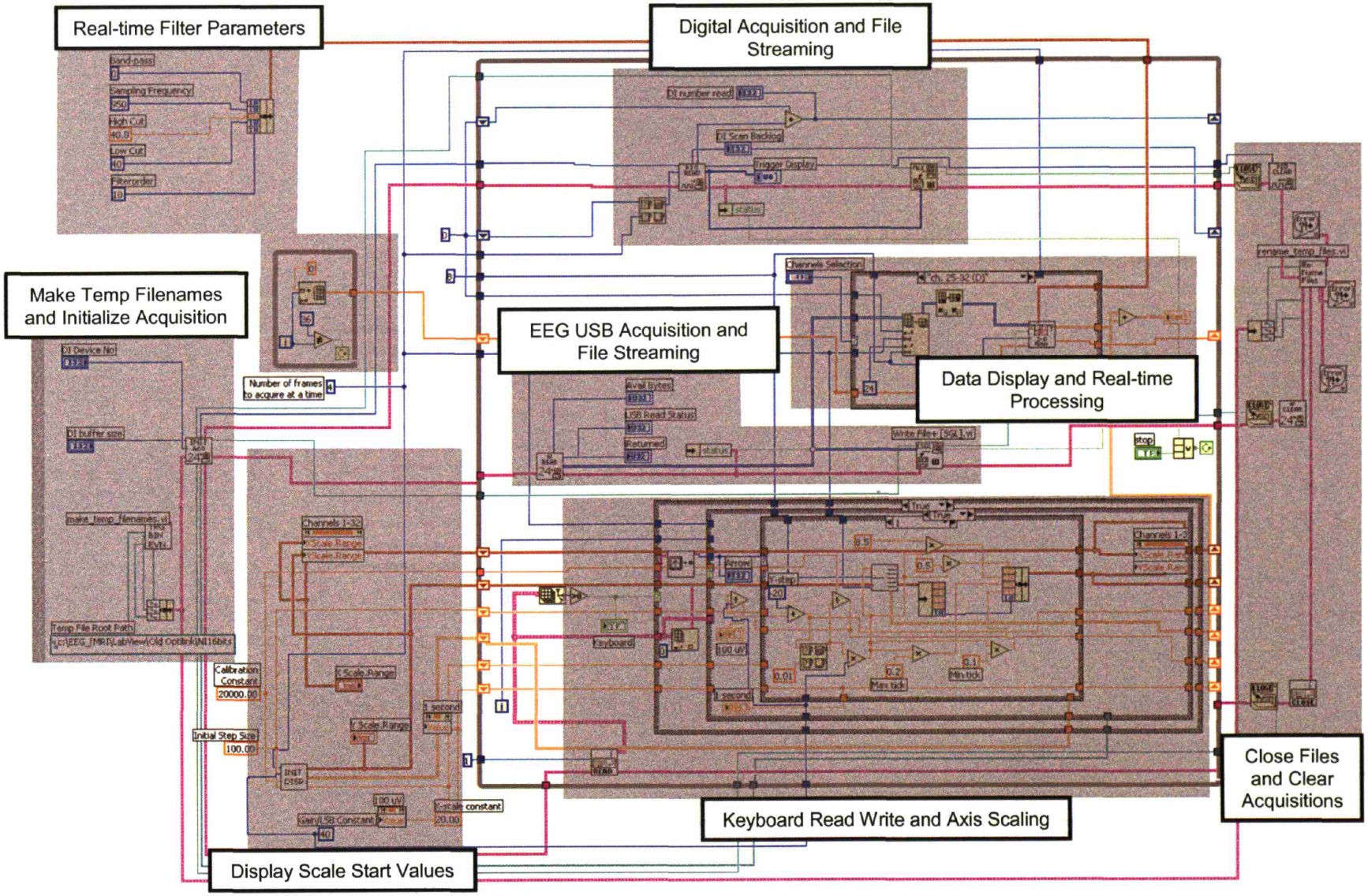

Figure 3.11. Top-level block diagram of EEG acquisition VI with functional annotations.

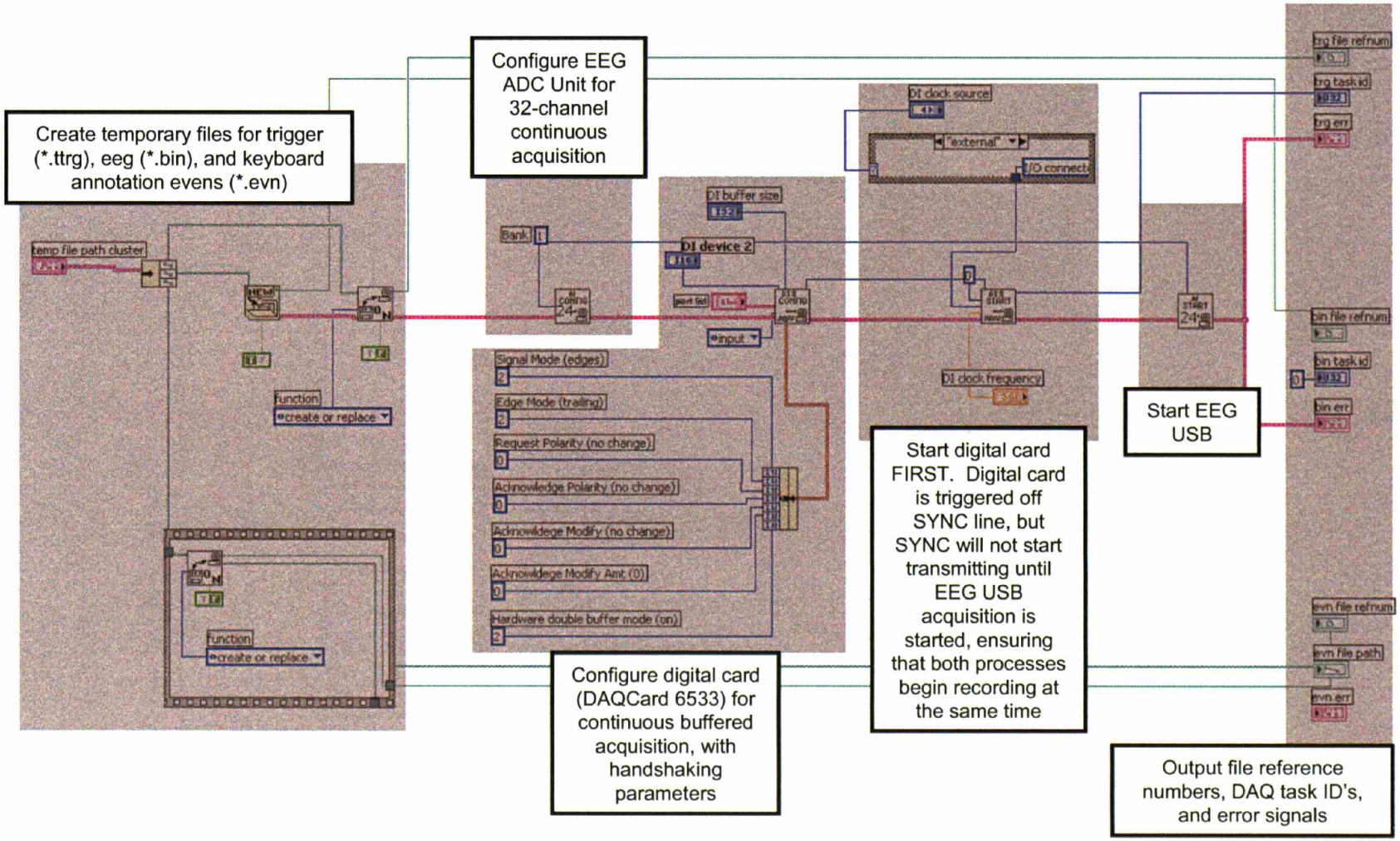

Figure 3.12. Annotated block diagram of "initialize_acquisition_24Bits.vi"

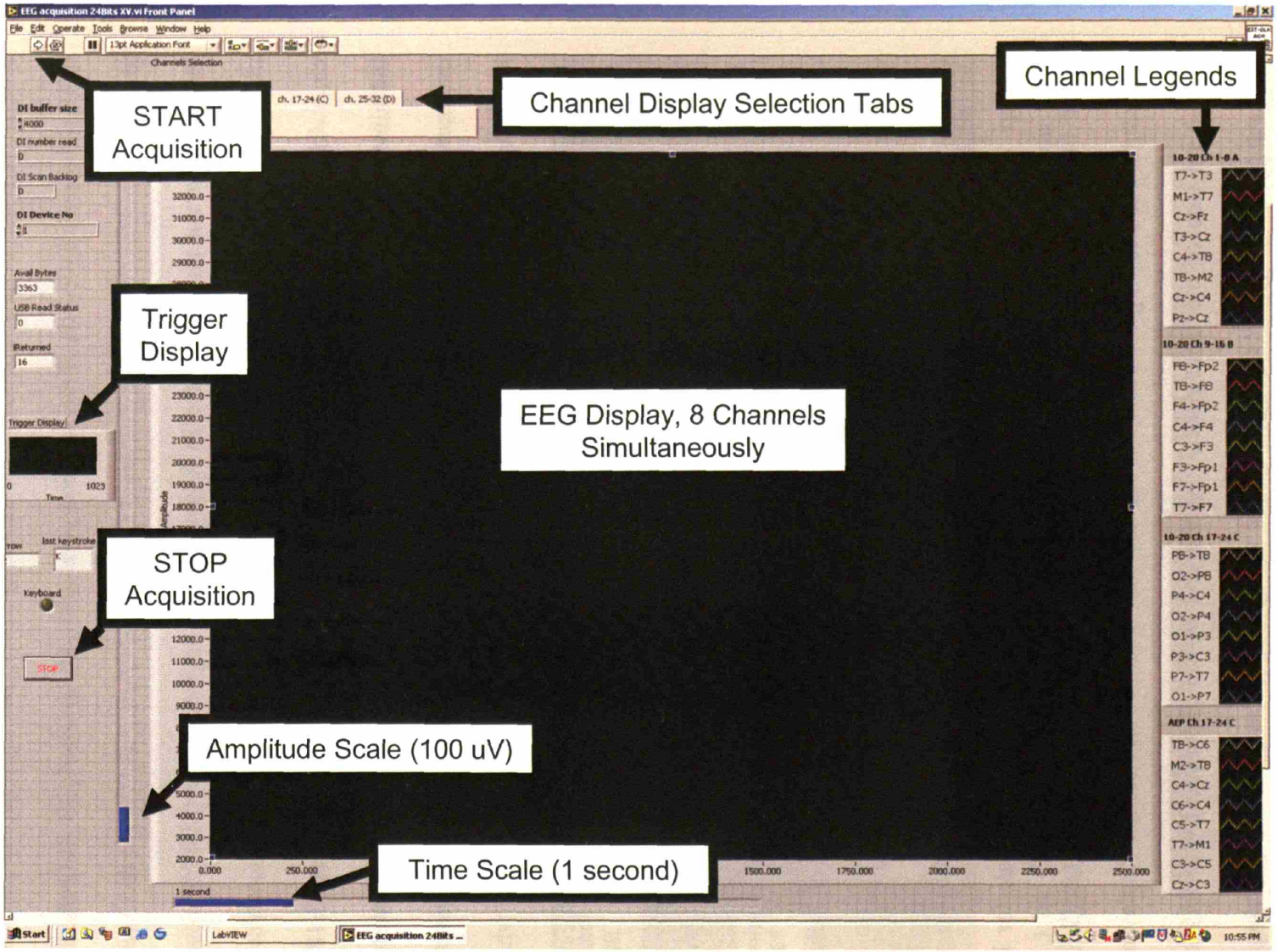

Figure 3.13. Front panel of EEG acquisition VI.

Figure 3.11 shows the top-level block diagram of the EEG data acquisition VI. When end-user begins acquisition, temporary files and acquisition processes are configured and started for three separate data streams: 1) The USB EEG data, 2) The DAQCard process for recording external signals (code for the DAQCard 6533 is shown, but is similar for the 6024E) and 3) A keyboard-polling process to record real-time end-user annotations (e.g., "m" for subject movement, "o" for eyes open, "c" for eyes closed, etc.). The initialization process for these acquisitions is described in **Figure 3.12**. After initialization, all three processes run continuously within a "while-loop" structure, where data are read, displayed, and streamed to disk. Real-time processing modules, such as the low-pass filter module illustrated in Figure 3.10) can also be added within the while-loop structure. At the end of the acquisition, all files are closed and acquisition processes are cleared.

The EEG acquisition front panel is shown in **Figure 3.13**. The acquisition is started by pressing the "run button" in the upper left corner of the LabView window. The acquisition will start immediately, and the user can switch between four different 8-channel displays, and can examine the trigger display to ensure that stimulus triggers or external signals are being received properly. Amplitude scaling can be adjusted by using the up- or down-arrow keys, with the blue vertical bar indicating the scale for 100 uV, while time scaling can be adjusted using the left- or right-arrow keys, with the blue horizontal bar showing the scale for one second. Channel legends are displayed on the right-hand side of the front panel. At the end of the experiment, the acquisition is stopped by pressing the "STOP" button. At this point, a file-saving dialog box is displayed prompting the user to provide a filename. The temporary files created at the

beginning of the acquisition are then re-named accordingly. The application software, USB interface, and external acquisition DAQCards are run on a Dell Latitude 810C with a 1.7GHz Pentium IV processor, 400 MHz bus, 1 GB of RAM, and 80 GB hard disk. For digital external signals using the DAQCard 6533, assuming a 16-bit digital input running at the base SYNC rate of 4 kHz, approximately 8 MB of disk space are required per minute of recording. Analog external signals using the DAQCard 6024E, assuming 8-channels of external signals at 16-bits, requires approximately 11.5 MB of disk space per minute of recording. **Figure 3.14** shows the complete system setup with amplifiers, EEG ADC acquisition unit, external signal card and cable assembly, and acquisition computer.

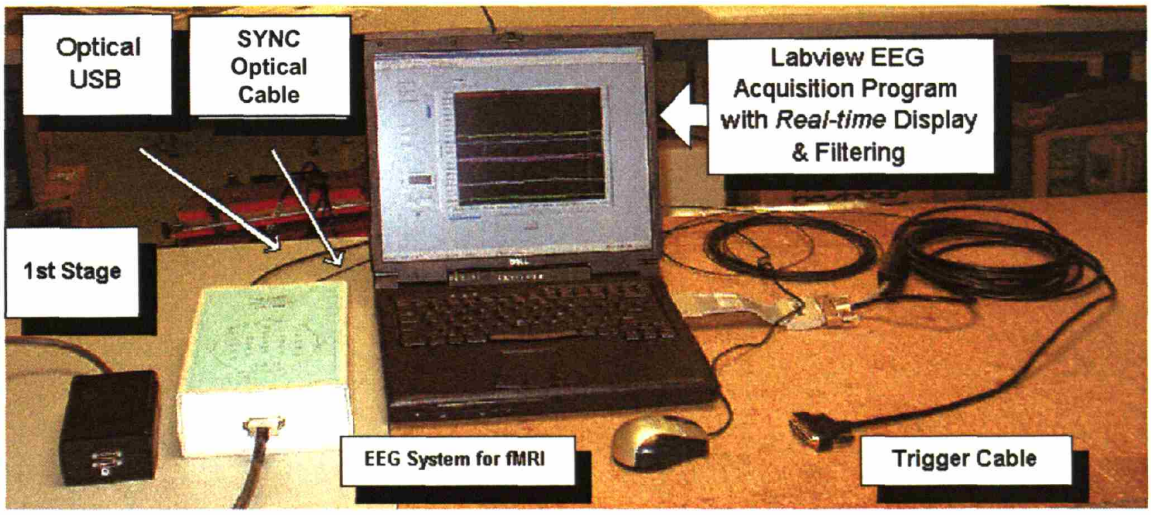

Figure 3.14. Complete system setup with amplifiers, EEG ADC acquisition unit, external signal card and cable assembly, and acquisition computer.

3.4. Electrode and Motion Sensor Systems for EEG-fMRI

As discussed in Chapter 2, heating due to increases in RF specific absorption rate from placement of scalp EEG electrodes is a potential problem for EEG-fMRI studies.

The de-facto standard to prevent electrode heating has been to place discrete resistors, 10 kOhm or larger, at the tip of each electrode (Lemieux et al., 1997), but simple direct calculations (Chapter 2) and RF simulations using realistic head models (Angelone and Bonmassar, 2004) illustrate that these resistors provide little or no power attenuation at the RF frequencies used for MRI, particularly at 3 or 7 Tesla. Modest resistances of as little as 4.2 Ohms/inch (166 Ohms/meter) distributed along the lead, achievable in practice using carbon fiber wires, can bring the SAR close to nominal levels (Angelone and Bonmassar, 2004). Another problem associated with EEG electrodes used during MRI is that motion or vibration within the static field will inductively couple noise signals through loops within the recording circuit. Since head motion, physiological pulsation, and vibration of the head and body are the largest source of this noise, loops formed from the EEG electrode leads provide the greatest opportunity for noise coupling.

We have designed a series of EEG electrodes to provide both RF protection and static field-induced noise attenuation. This system has been constructed from off-the-shelf components in two bipolar montage configurations, one spanning 8 channels along a coronal plane for auditory evoked potential (AEP) measurements, and a 19-electrode 10/20 montage designed for anesthesia and sleep studies (**Figure 3.15**). Since safety studies and experience at 3 or 7 Tesla had not been well-established at the time of design, the number of electrodes was chosen conservatively to limit RF heating risk. Carbon fiber wires ("Fiber-Ohm;" Marktek, Inc., Chesterfield, MO), with 7 Ohms/inch resistance (276 Ohms/meter), were used to limit increases in SAR, and were connected to Ag/Ag-Cl electrode bodies using conductive epoxy (Circuit Works CW2400, Chemtronics, Kennesaw, GA). These electrode bodies featured plastic housings to prevent direct

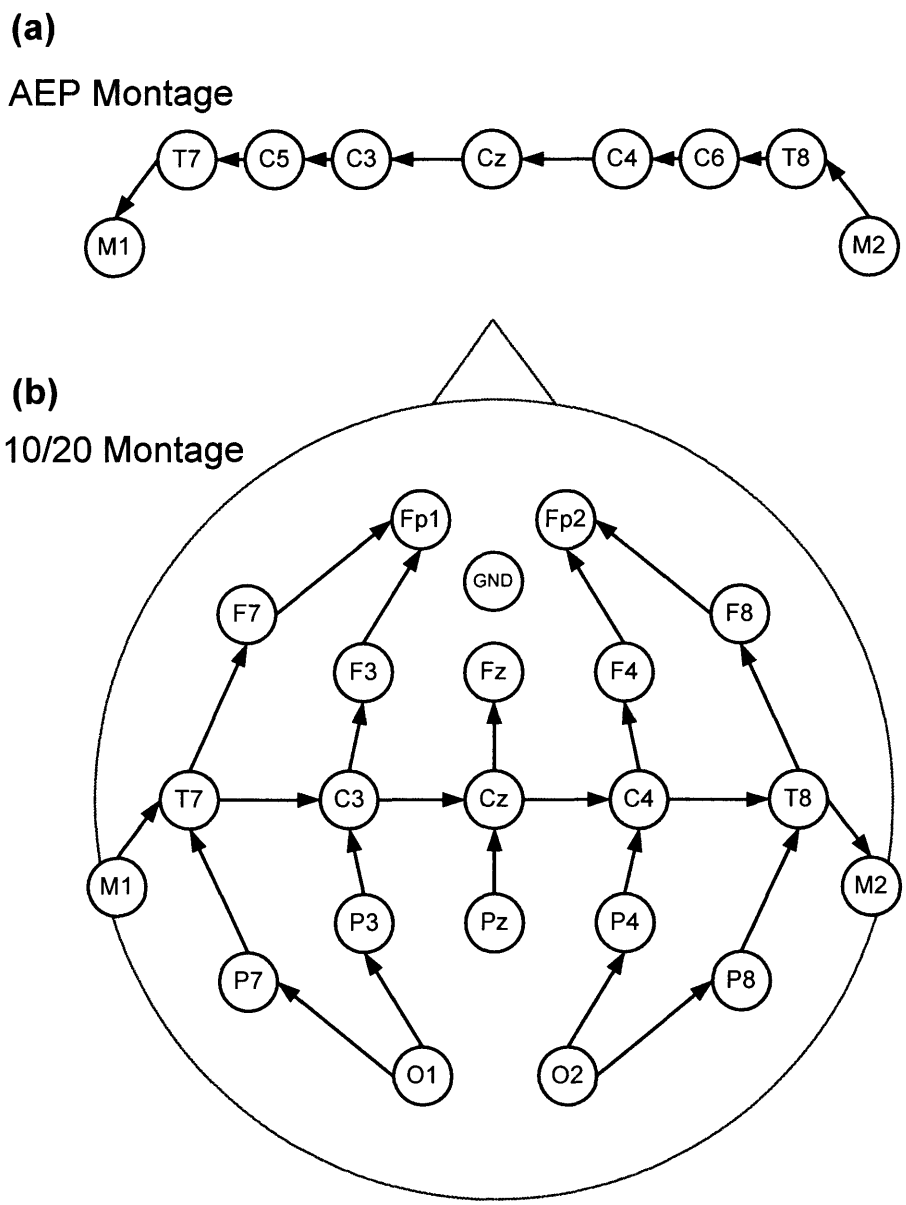

Figure 3.15. EEG-fMRI electrode montages: (a) Coronal AEP montage; (b) 10/20 montage.

electrode skin contact (Gereonics, Inc., Solana Beach, CA). To provide a reference signal for artifact removal using adaptive noise cancellation, a set of motion sensors were constructed from Murata PKM11-4A0 piezo-electric buzzers (Murata Electronics North America, Inc., Smyrna, GA) using similar methods, replacing soldered metallic leads with conductive epoxied carbon fiber leads (**Figure 3.16**).

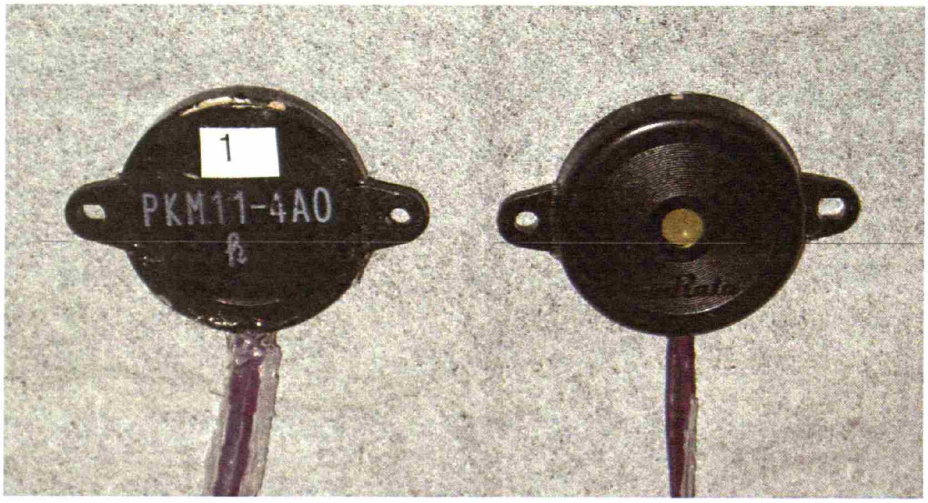

Figure 3.16. Motion sensors for EEG-fMRI.

To reduce motion-induced inductive noise coupling, the carbon fiber electrode wires were arranged in a "ribbon cable" fashion, with wire lengths cut to fit the appropriate electrode locations for average- to large-sized heads (**Figure 3.17**). The ribbon cable arrangement reduces motion-induced noise coupling by both reducing loop sizes between differential electrode pairs, and between electrodes and reference, and by holding these leads in a fixed relative position, which allows some of the noise coupling to be eliminated through common-mode rejection (**Figure 3.18**). The wires were bound together using silicone adhesive sealant, which served both to hold the wires together, and as a mass and damping material to reduce mechanical vibration. Construction details for these electrodes are provided in **Appendix 3A.4**. For complex montage arrangements such as the 10/20 system, the ribbon cable is more practical than twisted pair arrangements reported by some investigators (Goldman et al., 2000), and is likely to offer similar if not better performance due to the practical difficulty of braiding identically-sized loops from individual wires. Electrodes from the coronal montage can be held in

place with the combination of EEG paste, tape, and elastic surgical netting, while the 10/20 montage is best held in place with collodion glue and elastic surgical netting.

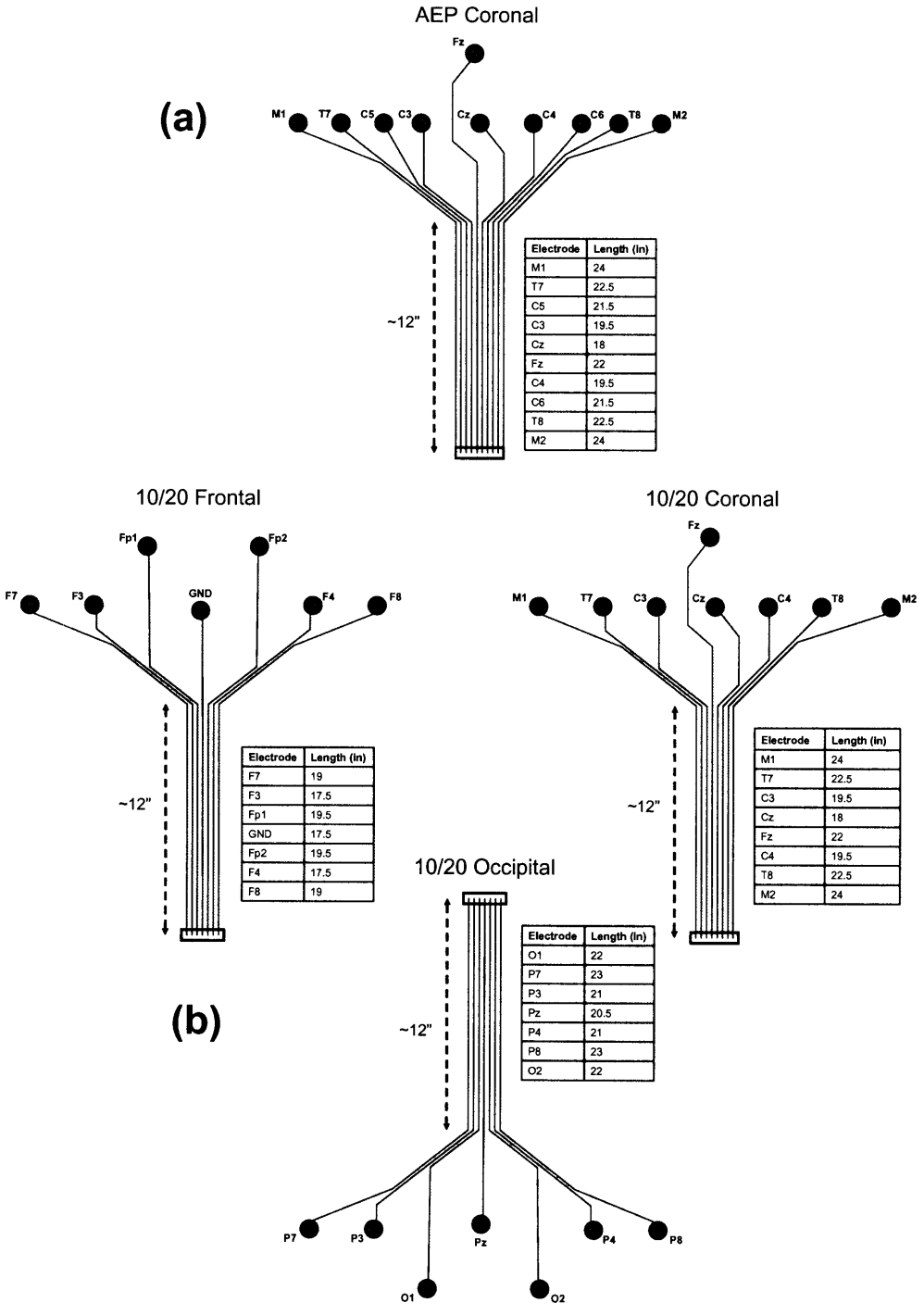

Figure 3.17. Ribbon cable EEG lead arrangements for (a) coronal montage and (b) 10/20 montage.

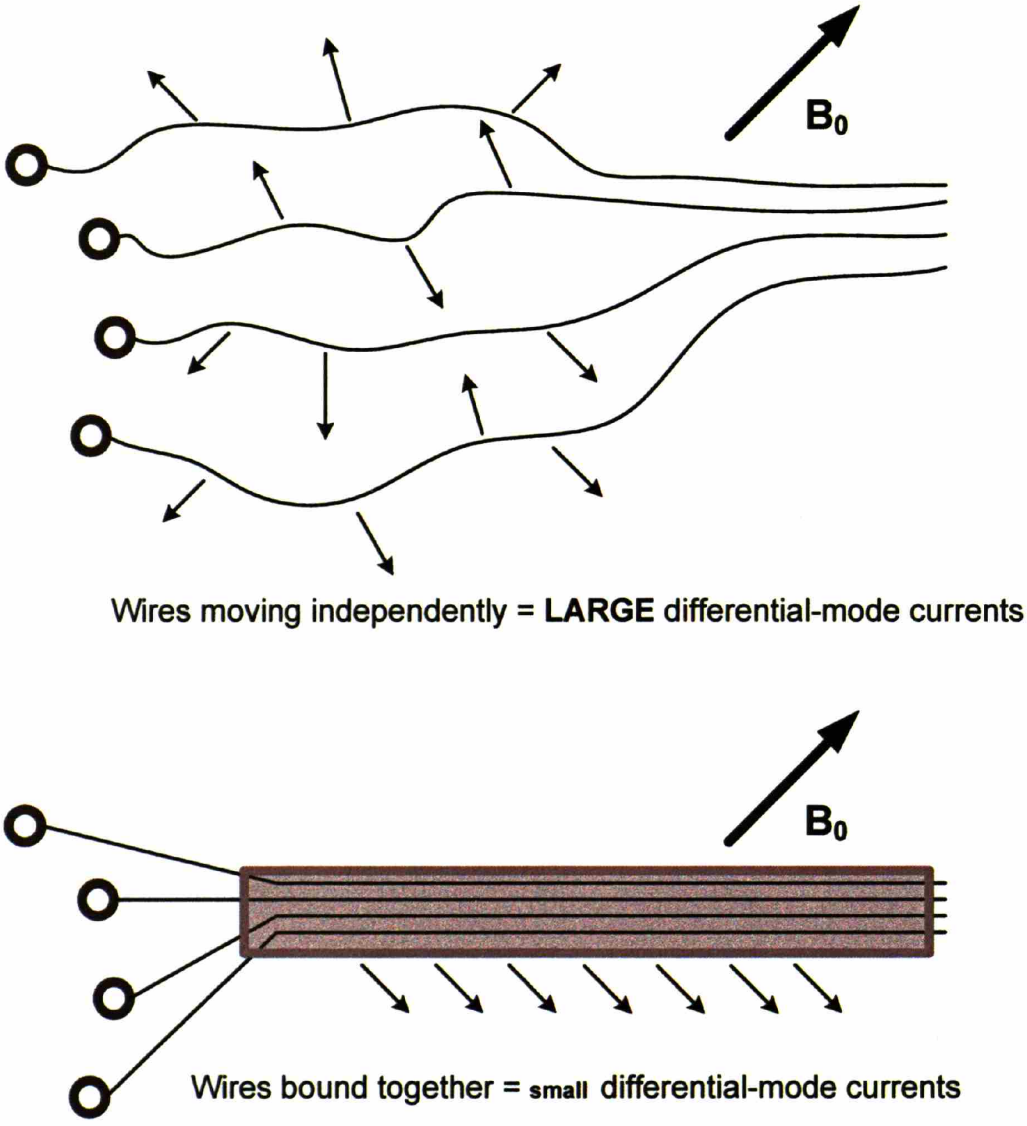

Figure 3.18. Ribbon cable EEG lead arrangement reduces electromechanical noise coupling.

Increased RF attenuation can be achieved with higher resistance levels, but there are practical limits on the resistance levels available with carbon fiber wires. Commercially available off-the-shelf wires come in two resistance ranges: a low resistance range of 4 to 7 Ohms/inch, and a higher resistance level of 3 M-Ohms/inch and beyond (Personal communication, Art Henn, Marktek, Inc., 2003). RF-attenuating EEG-

fMRI electrodes would likely require resistances in the 1 kOhm/inch range at most.[1] Carbon fiber composite wires, blending high and low resistance fibers, could be used to obtain intermediate values in this range, but could be expensive to manufacture in the small quantities required for EEG electrodes (Personal communication, Art Henn, Marktek, Inc., 2003). We have developed an alternative strategy using carbon or silver conductive inks to print or silkscreen electrode wires onto flex-circuit material. With this strategy, it is possible to selectively tune the impedance for each electrode lead, by controlling the mixture of inks used in the electrode, and to precisely layout leads into ribbons to reduce motion-induced noise coupling. A prototype EEG cap using this conductive ink technology with integrated motion sensors has been constructed and is being developed for routine use in EEG-fMRI studies (Vasios et al., 2005) (**Figure 3.19**), particularly those at high field where RF safety is a major concern.

Figure 3.19. EEG cap featuring conductive ink-based electrodes and integrated motion sensors.

[1] EEG leads from our applications have measured anywhere from 16 to 22 inches in length, and with 1 kOhm/inch resistance, this would give total electrode resistances in the range of 16 to 22 kOhm, resulting in a low-pass cutoff of 62 or 45 Hz, respectively, assuming a 1 nF parallel capacitance at input.

3.5. An Auditory Stimulus Delivery System for EEG-fMRI

Auditory stimulus presentation during fMRI or EEG-fMRI requires careful consideration of numerous design features, including timing precision, audio fidelity, MRI compatibility, and EEG compatibility. The inherent difficulty in meeting all these design challenges simultaneously is apparent when one examines the EEG-fMRI literature: Numerous groups have been successful at recording visual evoked potentials (VEPs) during fMRI (Bonmassar et al., 1999;Vanni et al., 2004;Garreffa et al., 2004), while relatively few have been able to record auditory evoked potentials (AEPs) during fMRI., achieving success mainly with simple tone stimuli at long inter-stimulus intervals (Liebenthal et al., 2003). Event-related potential (ERP) studies, regardless of the stimulus modality, require high-precision timing. Timing accuracy can be quantified in terms of average delay (or latency), which refers to the average time difference between the stimulus trigger onset and the actual stimulus onset, and the jitter about that average delay (**Figure 3.20**). Stimulus delays can be accounted for in ERP analysis simply by introducing an opposite delay prior to averaging, but large jitter values can compromise the ability to discern peaks within the ERP waveform. Audio fidelity, considered broadly, comprises many elements, including the frequency response of the headphone and amplification system, their total harmonic distortion, the maximum volume achievable by the system, and the degree of background noise, such as the notorious 60-Hz ground loop "hum." Compatibility with the MRI environment requires electromagnetic compatibility, study subject protection from acoustic scanner noise, use of non-ferrous headphone elements, and portability to accommodate multi-user MRI facilities or use in multiple imaging facilities. Audio systems must also be compatible

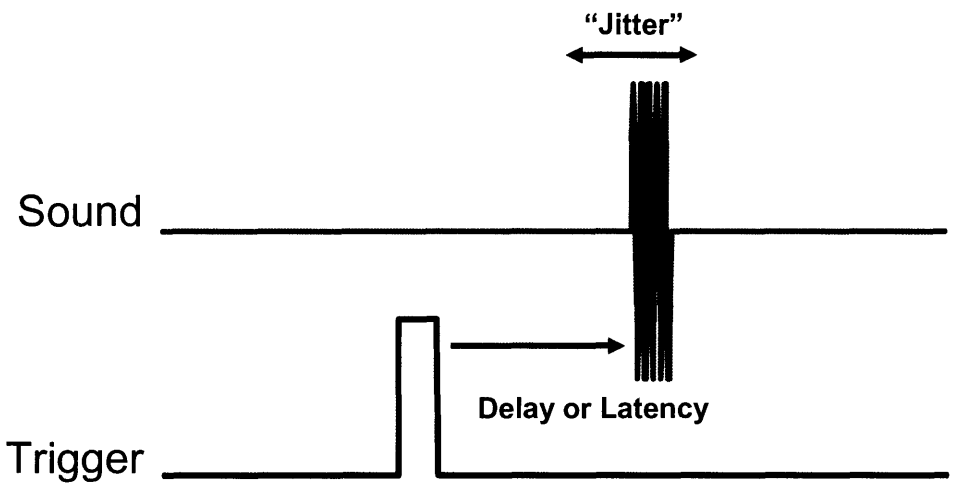

Figure 3.20. Stimulus presentation timing accuracy in terms of average delay (or latency) and jitter.

with ERP studies: Auditory ERPs are best observed using stimuli with high bandwidth, such as click trains or noise bursts, and are typically presented using headphones whose frequency response extends to 15 or 20 kHz. Headphones for ERP studies must not introduce stimulus-related noise coupling into the EEG recordings, as this could confound ERP analysis, depending on the experimental paradigm.

Auditory presentation systems fulfilling all these requirements are not available commercially. The requirement to use only non-ferrous components rules out standard magnetic-coil headphones. Headphones using air-tube sound transmission with sound-attenuating earmuffs (e.g., Avotec SS-3100, Avotec, Inc., Stuart, FL, USA) are popular for fMRI studies, but provide a frequency response of only 4.5 kHz, inadequate for stimuli such as click-trains or noise-bursts that require a high frequency-response. Electrostatic headphones provide a frequency response in excess of 20 kHz, but commercially available models (e.g., Koss ESP-900, Koss Corp., Milwaukee, WI, USA) offer no hearing protection. In addition, as will be shown below, electrostatic headphones emit electromagnetic fields that couple to EEG recordings with an amplitude

that is orders of magnitude higher than the EEG signal itself. In the next two sections, we describe a portable, electrically-isolated auditory stimulus presentation system capable of achieving sub-millisecond timing precision, combined with an electrostatic MRI-compatible headphone system with passive sound-attenuation and electrical shielding that eliminates noise coupling with EEG.

3.5.1. Stimulus presentation

Stimuli were delivered using an IBM Thinkpad T40 laptop (1.6 GHz P4, 512MB 266 MHz RAM, 80GB 4500rpm hard drive; IBM, White Plains, NY) running Microsoft Windows XP (Microsoft Corporation, Redmond, WA). To boost sound output levels and signal to noise relative to the onboard sound card, an Echo Indigo Digital Audio PCMCIA card (Echo Digital Audio Corp., Carpinteria, CA) was used as the sound device. The stimulus presentation laptop was configured to deliver stimulus triggers through its parallel port and was connected to the EEG acquisition computer as described in Section 3.3 and Appendix 3A.2. Task-related button-press responses were recorded using a USB button box configured as a keyboard device to send the numbers "1" through "4" for each of the keypad buttons. With the headphone system (described below), stimulus delivery and EEG acquisition computers connected and AC powered with no stimulus, there was no audible background noise of any kind. When the USB button box was added to this configuration, a faint 60-Hz hum could be perceived. This background hum was eliminated by electrically isolating the USB button box from the rest of the system using an Opticis M2-100 optical USB extension cable (Opticis North America Ltd., Richmond Hill, Ontario, Canada). Stimuli were scripted and delivered using NeuroBehavioral Systems Presentation 0.76 (NeuroBehavioral Systems, Albany,

CA). Stimulus delay and jitter relative to recorded parallel port stimulus triggers were measured by recording stimuli and triggers under different hardware and scripting arrangements. Depending on the laptop and sound hardware used, the average delay could be brought to within 1 msec, with a jitter of less than 1 msec, sufficiently accurate for most ERP experiments. A detailed description of the testing protocol and results for different laptop, software, and audio hardware configurations is provided in **Appendix 3A.5**.

3.5.2. A high-fidelity headphone system for simultaneous EEG-fMRI studies

A set of headphones were constructed for EEG-fMRI studies, featuring the high-fidelity audio performance of electrostatic headphones, passive sound attenuation, and electrical shielding for compatibility with EEG and ERP studies. The electrostatic headphone elements were removed from a set of Koss ESP-950 headphones (Koss Corp., Milwaukee, WI), electrically shielded, and placed within a set of sound-attenuating earmuffs (Silenta Ergomax, Oy Silenta Ltd., Finland). Electrical shielding was accomplished by replacing the first 6 feet of headphone cable with double-shielded (braid over foil) computer cabling, and by enclosing each headphone element within a conductive fabric sock constructed from silver-coated sheer nylon mesh (Less EMF Cat. #A209, Less EMF Inc., Albany, NY). The conductive fabric mesh was chosen for its low resistivity (<5 Ohms/square) and because of its thin, light, porous structure, providing minimal absorption of acoustic energy. Shielded cabling was limited to 6 feet to reduce capacitive load on the electrostatic amplifier system (<600 pF). The cable shield was connected to the conductive sock using copper foil tape, and terminated on a copper mesh housing encasing the Koss amplifier unit via a single wire running along the remaining

length of the headphone cable. The conductive sock was electrically insulated from the headphone using a thin plastic membrane. The amplifier unit was powered from a 9.6V rechargeable battery placed outside the MRI room and routed through the penetration panel. Battery power was chosen over AC power to reduce the risk of electrical shock in the event that bodily fluids such as mucosal secretions or vomitus cause a short circuit within the headphone elements. The battery ground terminal and amplifier shield were connected at the penetration panel. Construction details for the headphone system are provided in **Appendix 3A.6**.

Acoustic attenuation recordings were made using an electret condenser mic (Shure SM-93, Shure, Niles, IL) by comparing scanner noise during gradient echo functional scanning (Siemens Trio) with the microphone placed inside and then directly outside the headphone earmuff, with the headphones in place on a human volunteer. Acoustic attenuation measurements were made for the electrostatic system as well as an off-the-shelf Avotec MRI-compatible audio system (Avotec SS-3100, Avotec, Inc., Stuart, FL). Electromagnetic noise coupling measurements were made by coating an MRI phantom in EEG paste (Elefix, Nihon Kohden, Japan), placing adjacent bipolar pairs of EEG electrodes in the coronal plane to simulate the M1/2, T7/8, C3/4, C1/2, and Cz positions, fixing the headphone earpieces over the phantom while presenting sound stimuli, and recording using the EEG/fMRI recording system described earlier. Sound stimuli consisted of noise-bursts (12.5 msec) and click-trains (1 msec) sampled at 44.1 kHz, presented at 25 msec intervals, 30 seconds ON, 30 seconds OFF, using the stimulus presentation system described in Section 3.5.1. Recordings were made with the headphone shield disconnected and floating ("unshielded") and then with the shield

connected ("shielded"). Auditory ERPs and ASSRs were recorded from 24 human volunteers (similar stimuli and EEG setup) using the shielded-electrostatic headphone system. All studies were conducted with the approval of the Human Studies Committee at the Massachusetts General Hospital (Boston, MA), with informed consent from all volunteers.

Attenuation and noise coupling were studied by computing multi-taper power spectral estimates (Percival and Walden, 1993) for each condition, and taking ratios of the appropriate power spectra to determine attenuation or noise coupling. To quantify acoustic attenuation $A(e^{j\omega})$, the ratio of power spectra for sound recordings with microphones inside the earmuffs ($P_{inside}(e^{j\omega})$), were compared to the power spectra for recordings with microphones outside the earmuffs ($P_{outside}(e^{j\omega})$):

$$A(e^{j\omega}) = \frac{P_{inside}(e^{j\omega})}{P_{outside}(e^{j\omega})}. \tag{1.9}$$

To quantify electromagnetic noise coupling $C(e^{j\omega})$ for each shielding condition ("unshielded" or "shielded"), the EEG power spectra with stimulus "ON" ($P_{EEG,ON}(e^{j\omega})$) was compared to that for with the stimulus "OFF" ($P_{EEG,OFF}(e^{j\omega})$):

$$C(e^{j\omega}) = \frac{P_{EEG,ON}(e^{j\omega})}{P_{EEG,OFF}(e^{j\omega})}. \tag{1.10}$$

Acoustic attenuation for the shielded-electrostatic and Avotec systems were similar, 32.8 and 38.1 dB, respectively, averaged between 0.8 and 20 kHz. **Figure 3.21** shows electromagnetic noise coupling $C(e^{j\omega})$ on a dB scale for the unshielded (solid) and shielded (dotted) cases, illustrating that the shielding reduces electromagnetic noise coupling by over 40dB throughout the bandwidth of the EEG recording device. To

quantify the shielding effectiveness with greater sensitivity, **Figure 3.22** compares the shielded noise coupling (Phantom) with the 40-Hz ASSR from a human volunteer on a linear scale (perfect shielding corresponds to $C(e^{j\omega})=1$), illustrating that the shielded noise coupling is indistinguishable from background noise and is well below the level of the measured electrophysiological response (approx 1 uV p-p). For the human studies, there were no discernable image artifacts during MRI due to the headphones.

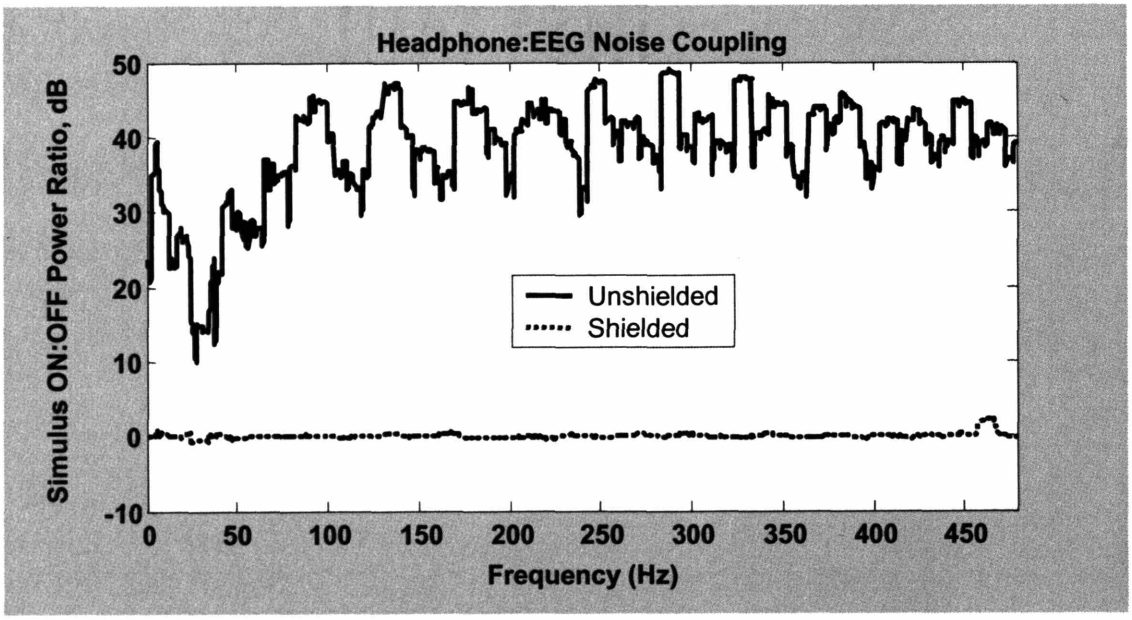

Figure 3.21. Headphone noise coupling, with and without shielding, across full EEG bandwidth

3.6. Summary

In this chapter we have described the design and implementation of a hardware and software system for recording EEG during fMRI consisting of: 1) An EEG amplification and analog-to-digital conversion system featuring low-noise and high-dyanamic range that is electromagnetically compatible for use within the MRI; 2) A computer hardware and software platform for EEG data acquisition that integrates EEG recordings with external signals such as event triggers and physiological monitoring, with

a user-expandable software platform offering the capability to do real-time EEG signal processing; 3) An EEG electrode system that reduces MRI-related noise coupling and radio-frequency (RF) specific absorption rate (SAR) relative to conventional EEG electrodes; 4) A stimulus delivery system integrated with the EEG acquisition system featuring a headphone system for use during MRI offering passive noise protection, high frequency response, and compatibility with ERP recordings.

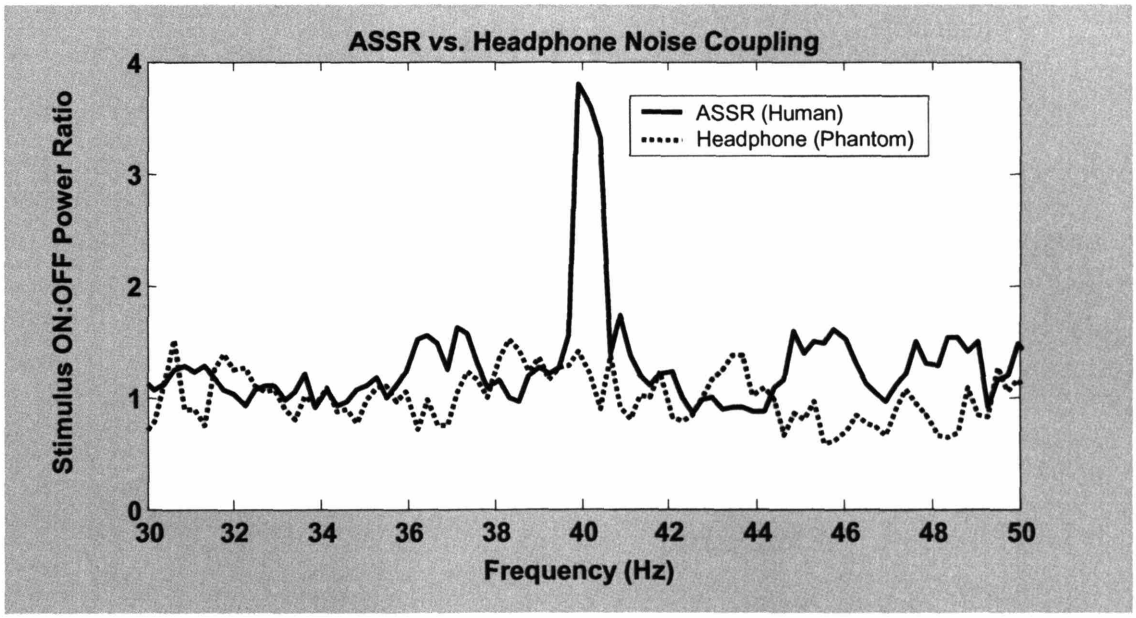

Figure 3.22. Comparison of auditory steady-state response (ASSR) to electrostatic headphone phantom recordings, illustrating that headphone shielding is effective

Appendix 3A.1. Construction details for shielded chassis endplates and 21-pin micro-D filtered connectors

Shielded chassis endplates were precision cut using a T-Tech CircuitWorks 7000 PCB milling machine (T-Tech, Norcross, GA), using FR4 PCB material featuring double-sided 0.5-ounce copper (T-Tech BM-FR4-1DS, T-Tech, Norcross, GA; Figure

3A.1.a). Endplate shielding was enhanced by using copper tape (3M 3324-1, 3M, St. Paul, MN) to connect the two copper faces, and by soldering a row of copper mesh "teeth" (50007G; Amaco, Inc., Indianapolis, IN) to each edge of the endplates, which provide a light abrasion to the oxidation layer of the aluminum coating to ensure good contact (**Figure 3A.1.b**). A series of internal bulkheads were constructed, in a fashion similar to the endplates, in order to provide additional RF isolation for the ADC unit via filtered interconnects. Arrays of 70 nF feed-through filter capacitors (Tusonix 4404-002, Tusonix, Tuscon, AZ) were placed in each bulkhead to route critical input-output signal lines such as +/-12V power, amplified EEG signal lines, and +/-10V power, similar to those shown in **Figure 3A.1.b**. The Tusonix 4404-002 feed-through capacitor is rated with a capacitance of 50nF guaranteed minimum value (GMV), but in practice the parts supplied had a capacitance of 70.6 +/- 3.4 nF (from random sample of N=20).

Non-ferromagnetic 21-pin MIL-SPEC-83513 micro-D connectors (Microdot 624-0021-0001, Tyco Electronics, Harrisburg, PA) were modified by installing custom-made 1nF micro-D planar capacitor arrays (Syfer A055101X, 1 nF +/-20%, X7R ceramic, 5GOhm at 40 VDC, Syfer Technology Limited, Norwich, UK; **Figure 3A.2.a**). These capacitor arrays provide uniform pin-to-pin and pin-to-ground capacitance with low effective series resistance (ESR), and a geometry that provides input-output RF filtration as close to the chassis as possible, minimizing high-frequency RF susceptibility or radiation. The capacitor arrays were placed within approximately 2mm of the micro-D connector shell and soldered to each pin using indium solder (Indium Solder Research Kit, Alloy #4, Indium Corporation of America, Utica, NY) at approximately 185-degrees C to reduce the likelihood of temperature-related stress fractures in the capacitor arrays.

The gap between the micro-D connector shell and the edge of the capacitor array was filled using a bare 14-gauge copper braid wire wrapped and soldered circumferentially to provide a 360-contact between the connector shell and capacitor array (**Figure 3A.2.b**). The amplifier analog ground was terminated to the amplifier chassis at pins 1, 10, 11, 12 and 21 of each micro-d input connector, with the corresponding pins on the capacitor arrays manufactured as ground pins (**Figure 3A.2.c**).

(a)

(b)

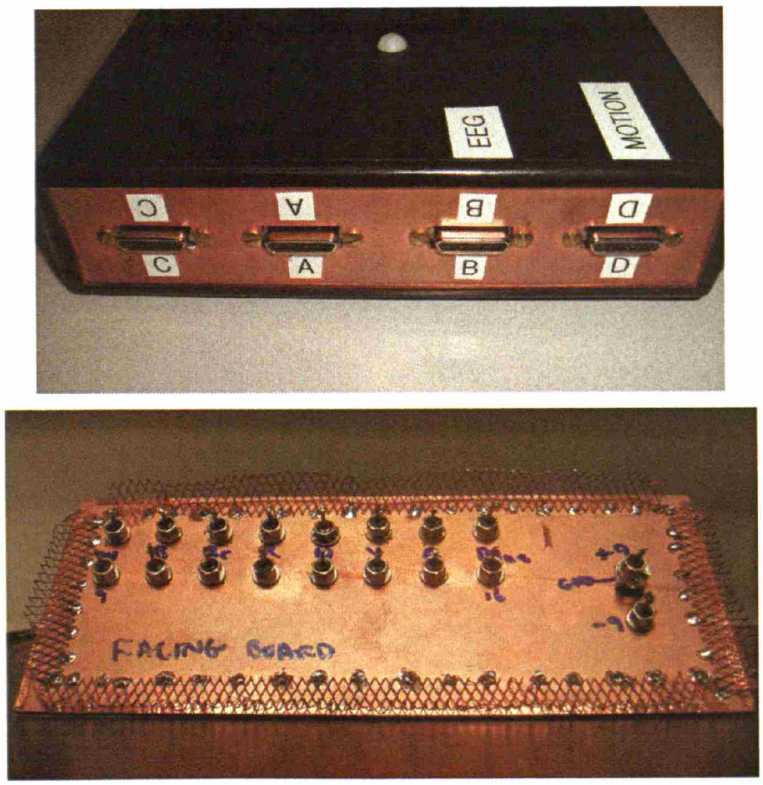

Figure 3A.1. Shielded Chassis Construction Details: (a) Double-sided copper endplates with precision-milled input-output connector ports; (b) RF bulkhead with feed-through capacitors and copper-mesh "teeth" to improve endplate-chassis connection.

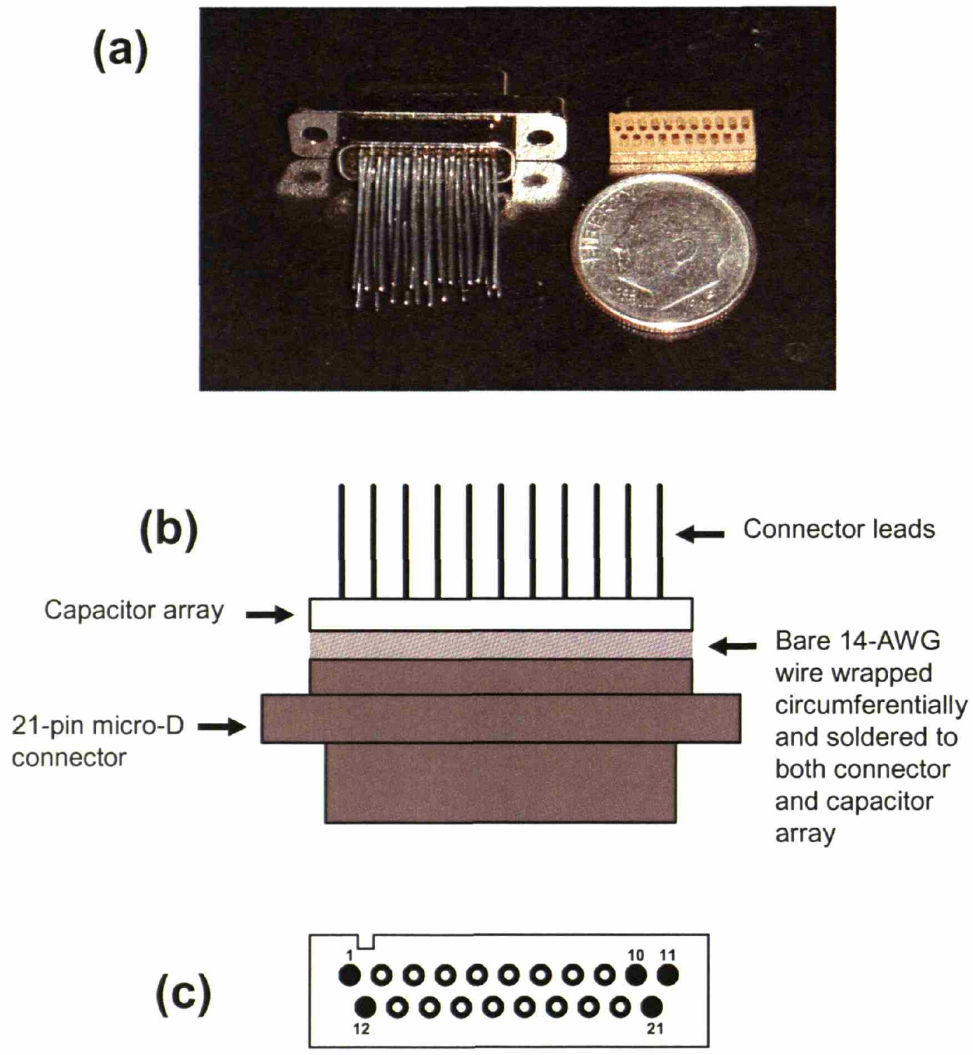

Figure 3A.2. 21-pin Micro-D Filtered Connector: (a) Photo of connector and capacitor array; (b) Schematic of capacitor array construction; (c) Location of ground-chassis connection at connector. Prior to order and delivery of capacitor arrays, the author constructed two prototype filtered connectors by individually soldering 1 nF 0405 surface mount ceramic capacitors between each of the 21 connector leads shown in (a) and the connector shell (not shown).

Appendix 3A.2. Interconnects for integration of external digital or analog signals.

Adapter cable assemblies were constructed to provide interconnects for each external signal setup. Event triggers were recorded from the DB-25 parallel port of the stimulus presentation computer (described in Section 3.4). For the digital setup, the 8 parallel port data lines (D0-D7) were tied to the first 8 data lines of the 6533 (DIOA0-DIOA7). The optical SYNC signal from the ADC unit was received by an Agilent HFBR-2521 optical receiver (Agilent, Palo Alto, CA). The SYNC signal was connected to the REQ1 pin of the 6533 to drive externally-triggered acquisition. These connections were made using a National Instruments 68-pin backshell assembly (National Instruments 776832-01, National Instruments, Austin, TX). For the analog setup, the first four parallel port data lines (D0-D3) were connected to analog channels AI4-AI7, and the SYNC signal from the Agilent HFBR-2521 was tied to both PFI0 (TRIG1) and PFI7 (STARTSCAN) of the 6024E. Analog input channels AI0-AI3 were connected to pins 1 through 4 of a female DB-9 connector, to interface with the analog output lines from an Invivo Magnitude MRI-Compatible Patient Monitor (Invivo Research, Orlando, FL) corresponding to electrocardiogram (ECG), invasive pressure (P1), end-tidal CO2 (EtCO2), and pulse oximetry (SpO2) signals. A two-layer PCB board was constructed to integrate the optical receiver and input signals with a 68-pin connector to interface with the 6024E (National Instruments 777600-01, National Instruments, Austin, TX).

Appendix 3A.3. USB EEG interface functions.

3A.3.1. Overview of software drivers.

The software drivers for the USB EEG acquisition device consist of two pieces: A dynamic linked-library (DLL) for the FTDI FT245BM chipset used in the DLP USB interface ("FTD2XX.DLL"; Future Technology Devices International, Ltd., Glasgow, Scotland, UK; DLP Design, Inc., Allen, TX), and a second DLL written by Techen, Inc. ("TNusb.DLL" revision 110702; Milton, MA) to interface with the Ubicom SX48 (Ubicom, Inc., Mountain View, CA). Both files must be installed in the %SystemRoot%/System32 directory.

3A.3.2. Integration of USB DAQ functions from TNusb.DLL into LabView intermediate-level DAQ VI structure.

In Table 3A.3.1 below we describe four LabView intermediate-level DAQ VIs and their construction based on USB DAQ functions from TNusb.DLL. Most of these USB EEG VI's are constructed from simple LabView library function call, except for "AI Read 24-Bits.vi," which requires additional control structures to check the device status before reading data. A block diagram and description for "AI Read 24Bits.vi" is illustrated in **Figure 3A.3.1**.

VI Name	AI Config 24Bits
Purpose	Configure EEG acquisition
USB Commands Used	unsigned long_UsbConfig@16(unsigned long iBank, unsigned long iCount, unsigned long iadcCH, unsigned long iFilter);
Description	iBank (1-8): Specifies SX48 memory location where configuration setting will be stored. Operates much like the "process ID" used in NI DAQ VIs. iCount (0-65535): Number of samples to acquire. "0" corresponds to continuous recording. Set to "0" in AI Config 24Bits. iadcCH (1-5): ADC channel to take data from. "5" corresponds to multiplexing through all four channels on each chip, resulting in 32 channels total.
VI Name	**AI Start 24Bits**
Purpose	Start EEG acquisition
USB Commands Used	unsigned long_UsbStart@8(unsigned long iBank, unsigned long iCount);
Description	iBank (1-8): Specifies SX48 memory location where configuration setting have been stored during "AI Config 24-Bits" process. Operates much like the "process ID" used in NI DAQ VIs. iCount (0-65535): Number of samples to acquire. "0" corresponds to continuous recording. Set to "0" in AI Config 24Bits.
VI Name	**AI Read 24Bits**
Purpose	Read EEG data in buffered acquisition
USB Commands Used	unsigned long UsbStatus(unsigned long *AvailableBytes); unsigned long_UsbRead@12(long_*Data, unsigned long *iReturned, unsigned long *AvailableBytes);
Description	AvailableBytes: Available bytes in buffer. Data: Data packet consisting of a 16x10 array of 32-bit signed integers. Only first 8 columns of array contain EEG data. In full multiplexing mode (iadcCH=5), each packet corresponds to 4 time points of 32 channels. AI Read 24Bits.vi re-packages each packet into a 4 (time) x 32 (channel) array.
VI Name	**AI Clear 24Bits**
Purpose	Stop EEG acquisition
USB Commands Used	Unsigned long_UsbStop@0(void);
Description	Required for proper acquisition termination. If VI is terminated without using this function, EEG ADC unit may have to be re-booted to resume normal operation.

Table 3A.3.1. LabView intermediate-level DAQ VIs and USB DAQ functions from TNusb.DLL

3A.3.3. Status Messages

The FTD2XX.DLL driver has a series of status messages ranging from 0 to 17. The TNusb.DLL driver wrapper has an additional series of status messages ranging from 256 to 263 and 999. All the status message definitions are listed below.

Message	Code
FTD2XX.DLL Status Messages:	
FT_OK	0
FT_INVALID_HANDLE	1
FT_DEVICE_NOT_FOUND	2
FT_DEVICE_NOT_OPENED	3
FT_IO_ERROR	4
FT_INSUFFICIENT_RESOURCES	5
FT_INVALID_PARAMETER	6
FT_INVALID_BAUD_RATE	7
FT_DEVICE_NOT_OPENED_FOR_ERASE	8
FT_DEVICE_NOT_OPENED_FOR_WRITE	9
FT_FAILED_TO_WRITE_DEVICE	10
FT_EEPROM_READ_FAILED	11
FT_EEPROM_WRITE_FAILED	12
FT_EEPROM_ERASE_FAILED	13
FT_EEPROM_NOT_PRESENT	14
FT_EEPROM_NOT_PROGRAMMED	15
FT_INVALID_ARGS	16
FT_OTHER_ERROR	17
TNusb.DLL Status Messages:	
TN_DeviceNotOpen	256
TN_ParameterLimit	257
TN_BytesWrittenError	258
TN_DeviceAlreadyOpened	259
TN_NoDataAvailable	260
TN_NumAvailableBusy	261
TN_SYNCBytesNotFound	262
TN_AlreadyProcessing	263
TN_BufferOverRun	999

Table 3A.3.1. Status Messages.

Message 999 indicates that the TNusb.DLL internal 2 million byte buffer has over flown. If this status message is received, no additional data can be read from the buffer before a new "start" command has been issued.

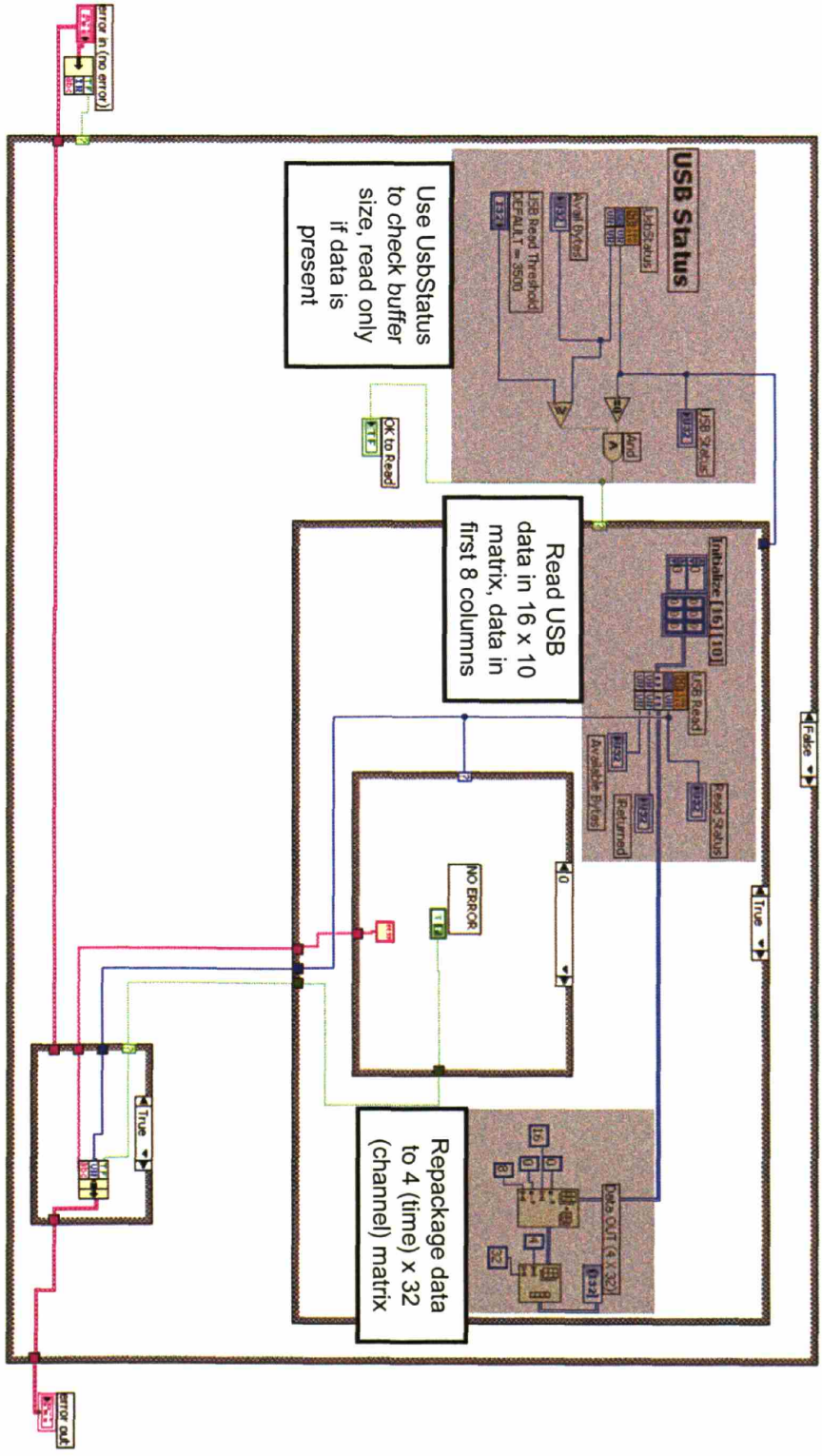

Figure 3A.3.1. Block diagram of for "AI Read 24Bits.vi"

Appendix 3A.4. Electrode construction details.

Carbon fiber wires ("Fiber-Ohm;" Marktek, Inc., Chesterfield, MO), with 7 Ohms/inch resistance (276 Ohms/meter), were bonded to Gereonics Ag/Ag-Cl electrode bodies (Gereonics, Inc., Solana Beach, CA) using conductive epoxy (Circuit Works CW2400; Chemtronics, Kennesaw, GA). These electrode-to-wire connections were mechanically reinforced by using an adhesive sealant (Shoe Goo, Eclectic Products, Inc., Pineville, LA) to form a protective sheath around the conductive epoxy joint (**Figure 3A.4.a**). Electrode wires were arranged into a ribbon and then bonded together with a double-sided coating of RTV silicone (MG Chemicals 1015-85, MG Chemicals, Surrey, British Columbia, Canada), as shown in **Figure 3A.4.b**. A PCB adapter was constructed to provide connections between the 21-pin MIL-SPEC-83513 micro-D connectors (**Figure 3A.4.d**; Microdot 8-1532027-4, Tyco Electronics, Harrisburg, PA) and short segments of ribbon cable, which were then bonded to the carbon fiber wires using standard cable crimp connectors (**Figure 3A.4.c**; Gardner Bender 10-123, Gardner Bender, Milwaukee, WI).

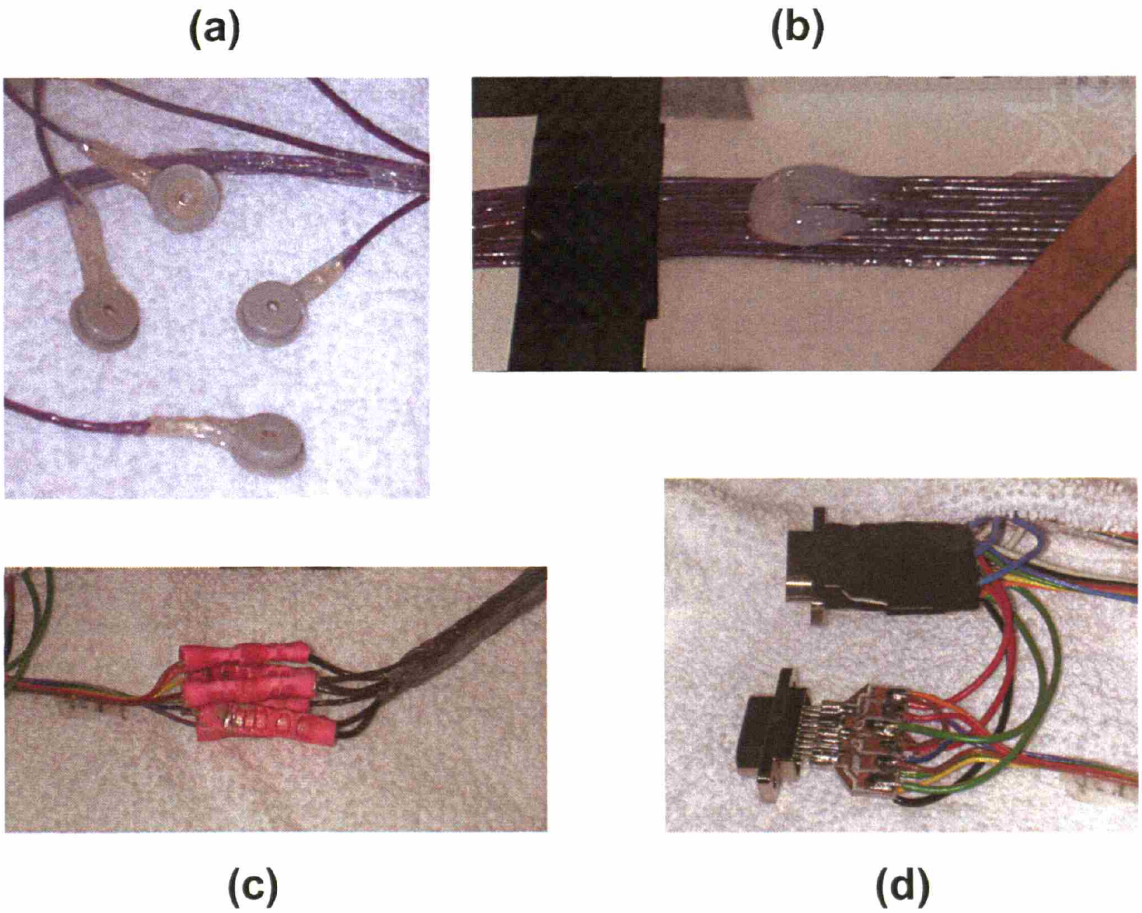

Figure 3A.4. Electrode construction details: (a) Electrode-to-wire connections made with conductive epoxy and mechanically reinforced with adhesive sealant; (b) Bonding of ribbon cable using RTV silicone; (c) Butt-splice connectors bonded with conductive epoxy to join carbon fiber wires with copper braid ribbon cable from 21-pin micro-D connector (d) PCB adapter to interface with 21-pin micro-D connector.

Appendix 3A.5. Stimulus Timing Accuracy

Stimulus timing accuracy for a variety of hardware and software configurations were tested using a modified version of the NeuroBehavioral Systems Sound Card Latency Analyzer (SCLA) software distribution (release date ca. January 2004, NeuroBehavioral Systems, Carpinteria, CA). For many of the experimental protocols used in our laboratory, precise timing between fMRI acquisitions and stimulus delivery were desired. If the MRI system and Presentation system operate independently during a

scan, small systematic differences between the MRI system timing and Presentation timing could produce large accumulated timing errors during longer fMRI scans. To enforce precise timing between fMRI acquisitions and stimulus delivery, presentation scripts were developed to provide an external trigger to the MRI system via the parallel port. Since Presentation handles port output (i.e., triggers) with interrupts, there was concern that use of multiple trigger types (e.g., stimulus triggers vs. scan triggers) might influence stimulus timing. For this reason the SCLA testing protocol was modified to give insight into how different configurations of stimulus and scan triggers might influence timing accuracy. Three trigger configurations were tested, as illustrated in **Figure 3A.5.1:** (1) Sending only stimulus triggers and no scan triggers (NO_SCAN); (2) Sending stimulus and scan triggers simultaneously (SIMULTANEOUS); (3) Delaying stimulus triggers by 200 msec after scan triggers (STIM_DELAY). In addition, since specific computer configurations can influence timing, several hardware and software configurations were tested: (1) Different laptops (an IBM Thinkpad T40 running Windows XP vs. a Dell Latitude C610 running Windows 2000), (2) Different versions of Presentation (0.47 vs. 0.76), and (3) Different sound cards (laptop built-in sound or external Echo Indigo PCMCIA card).

Recording hardware were set up according to the suggested SCLA protocol, with one computer used to provide the stimuli, and another to record the stimuli and triggers using its audio input jack: a 1/8" stereo audio jack was connected to the line-in input of recording computer, with one channel set to the audio channel and the other tied to the Data0 pin of the presentation computer (**Figure 3A.5.2**). A 10 msec 2 KHz sine wave was used as the stimulus, with a stimulus trigger duration of 5 msec. Each

stimulus/stimulus-trigger/scan-trigger packet was presented at an interval of 500 msec, with 100 trials per experimental condition. The stimulus and trigger outputs were recorded as WAV files from the sound input port using the Windows sound recorder utility. The data were analyzed using Matlab (Mathworks, Natick, MA). Onset timing for stimuli and stimulus triggers were detected by thresholding (threshold value of 0.2 for data values ranging from -1 to +1), and the mean (delay) and standard deviation (jitter) were computed for the difference between stimulus time and stimulus trigger time for each experimental condition. These results are summarized in Table 3A.1. A number of important inferences can be made from these data:

1. Stimuli should be delayed relative to scan triggers if possible. Across all conditions, both average delay and jitter were orders of magnitude larger when scan and stimulus triggers were delivered simultaneously. When stimuli were delayed relative to scan triggers, delay and jitter values were similar to those without scan triggers.
2. Use of the Echo Indigo PCMCIA sound device added approximately 1 msec to the average delay compared with onboard sound devices, but jitter values remained similar when averaged across laptops and remained below 1 msec. Occasional sound stimulus events were omitted when using this card with Presentation 0.76, but this occurred only for ~1% of trials presented with this card and software version.

Computer	Sound Device	Pres. Ver.	Stimulus Condition	Avg. Delay	Jitter
LatitudeC610	CrystalWDM	0.76	NO_SCAN	-0.485	0.057
LatitudeC610	CrystalWDM	0.76	SIMULTANEOUS	-26.245	2.826
LatitudeC610	CrystalWDM	0.76	STIM_DELAY	-0.588	0.412
LatitudeC610	Echo Indigo	0.47	NO_SCAN	-23.722	0.831
LatitudeC610	Echo Indigo	0.47	SIMULTANEOUS	-25.845	0.849
LatitudeC610	Echo Indigo	0.47	STIM_DELAY	-25.461	0.848
LatitudeC610	Echo Indigo*[2]	0.76	NO_SCAN	-1.566	0.223
LatitudeC610	Echo Indigo*[4]	0.76	SIMULTANEOUS	-30.181	2.655
LatitudeC610	Echo Indigo	0.76	STIM_DELAY	-1.789	0.09
ThinkpadT40	Echo Indigo*[1]	0.76	NO_SCAN	-1.869	0.256
ThinkpadT40	Echo Indigo	0.76	SIMULTANEOUS	-23.29	0.132
ThinkpadT40	Echo Indigo	0.76	STIM_DELAY	-1.914	0.495
ThinkpadT40	SoundMAX	0.76	NO_SCAN	-0.801	0.215
ThinkpadT40	SoundMAX	0.76	SIMULTANEOUS	-25.553	0.074
ThinkpadT40	SoundMAX	0.76	STIM_DELAY	-0.93	0.062

Table 3A.1. Average delay and jitter (std. dev.) values for different presentation hardware and software configurations. "CrystalWDM" and "SoundMAX" refer to chipsets for built-in laptop sound.

* = On these trials, sound stimuli were missing for 2, 4, or 1 out of 100 stimuli presented.

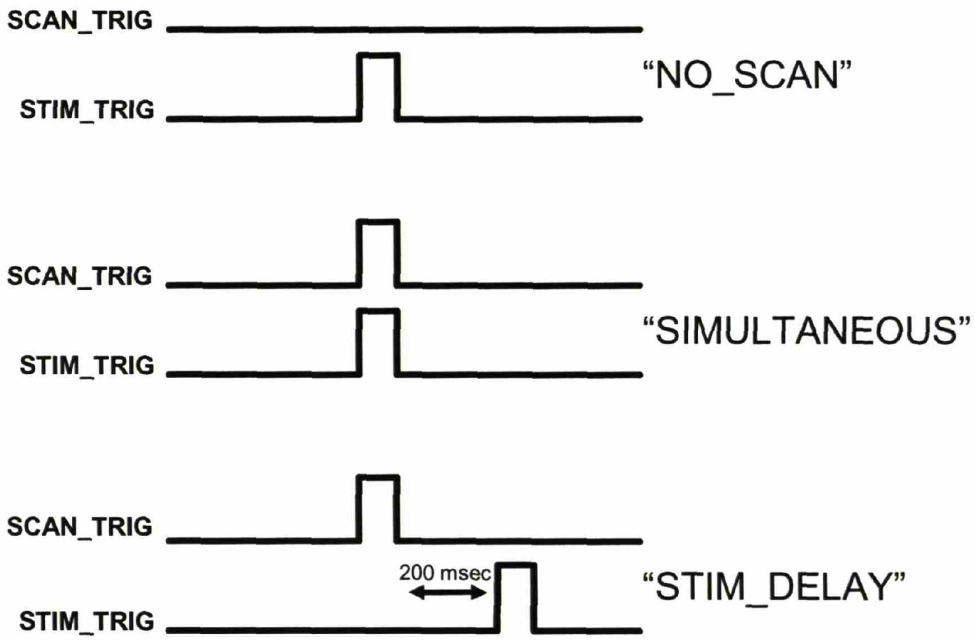

Figure 3A.5.1. Timing configurations for stimulus and scan triggers.

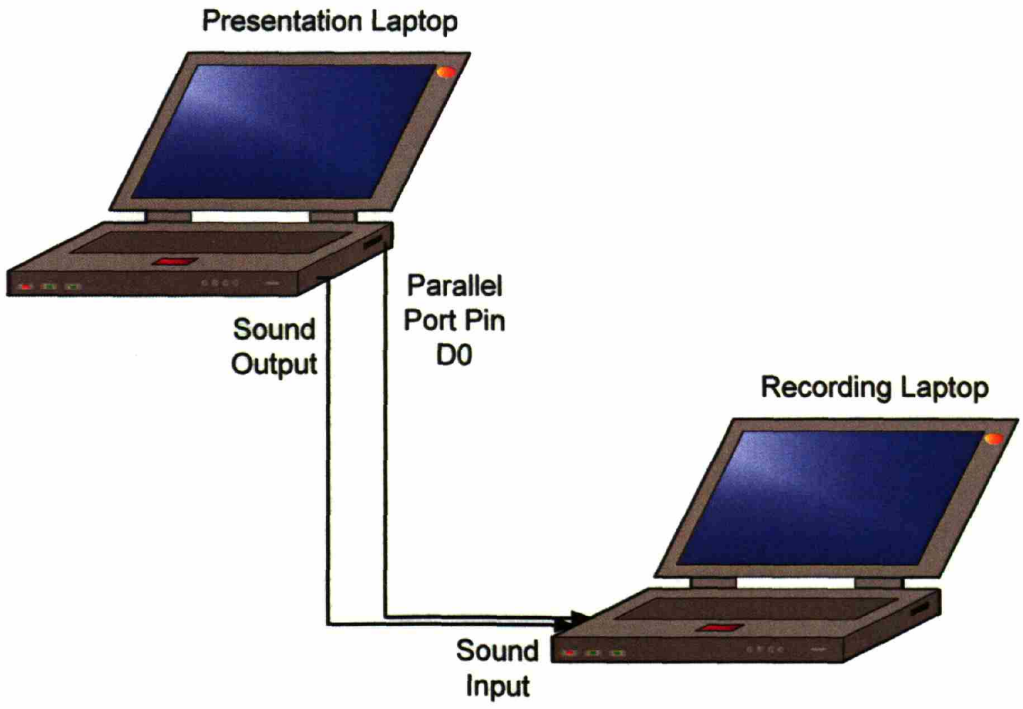

Figure 3A.5.2. Hardware connections for SCLA protocol.

Appendix 3A.6. Construction details for electrically-shielded acoustically-attenuating electrostatic headphones

3A.6.1. Modification of sound attenuating earmuffs

Sound-attenuating earmuffs (Silenta Ergomax, Oy Silenta Ltd., Finland) were modified to enclose the electrostatic headphone elements from a set of Koss ESP-950 headphones (Koss Corp., Milwaukee, WI). Internal molding posts and sharp edges were filed down to prevent abrasion or damage to the headphone elements. An aperture was cut at the bottom of each headphone enclosure, approximately 1.5 x 4.5 cm in dimensions, to allow the electrical contacts of the electrostatic headphone elements to fit inside the enclosure. A plastic box enclosure, approximately 2 x 5 x 5 cm in dimensions, was fused to the aperture using hot melt glue to protect the electrical contacts of the headphone elements. A ¼" hole was drilled in the outer aspect of each plastic box to allow cabling to pass through. The ear-cushion ring assembly was modified by placing a hard plastic mesh backing material (with ~1/8" holes) over the ear aperture, covering the external (ear side) of the hard plastic mesh with speaker cloth. This modification was made to prevent direct contact between the study subject and headphone elements. The modified enclosure is shown in **Figure 3A.6.1**.

3A.6.2. Replacing stock cables with double-shielded cables

The electrostatic headphone elements were removed from a set of Koss ESP-950 headphones (**Figure 3A.6.2**). The first 6 feet of stock cable attached to the headphone elements were replaced with double-shielded (braid over foil) computer cabling, taking care to leave approximately 1 cm of both braid and foil shield exposed near the

headphone elements. The double-shielded cables were threaded through the holes in the sound-attenuating enclosures, and then re-connected with headphone elements according to the wiring chart shown in **Figure 3A.6.3**. An additional 6 feet of stock headphone cable was spliced to the double-shielded cabling to provide connection with the amplifier unit, with a small plastic junction box to protect the cable splicing (**Figure 3A.6.4**). Heyco strain relief connectors (Bolt Products, Inc., City of Industry, CA) were also used to reinforce the cable connections. The computer cable shield was extended along the length of the stock headphone cable with a single 14-AWG wire, to allow for termination to the amplifier shield (described below). The stock headphone cable and ground cable were bound together and protected by a spiral cable wrap attached to the junction box with hot melt glue (**Figure 3A.6.4**).

3A.6.3. Electrical insulation for electrostatic headphone elements

Large diameter shrink-tubing was used to insulate the electrical connectors of the headphone elements. A single layered thin plastic membrane was wrapped around each headphone element and sealed to the large diameter shrink tubing using double-sided tape. A small 1 x 1 cm piece of electrician's tape was used to reinforce the thin plastic over the upper portion of the headphone element's electrical connector that remained unprotected by the large diameter shrink tubing. These elements are illustrated in **Figure 3A.6.5**.

3A.6.3. Conductive mesh fabric shield for electrostatic headphone elements

The electrostatic headphone elements were shielded by placing a conductive fabric sock constructed from silver-coated sheer nylon (Less EMF Cat. #A209, Less EMF Inc., Albany, NY) over the headphone element. The conductive fabric was chosen for its

low resistivity (<5 Ohms/square) and low acoustic absorption. The conductive mesh sock was sewn together circumferentially, except for a small hole where connector wires were allowed to pass. The fabric sock was carefully terminated to the double-shielded computer cable using copper tape applied in two stages. First, the open end of the fabric sock was wrapped circumferentially around the inner foil shield, which was secured with a wrapping of copper tape. Second, the braid shield was distributed circumferentially around that first layer of copper tape, and then secured in place with a second layer of copper tape. The shielded electrostatic elements were carefully inserted into the earmuff enclosure, a thin ring of plastic foam was placed around the outside edge of the electrostatic element to prevent abrasions from the ear cushion, and the ear cushion was snapped into place. Heyco strain relief connectors were used to secure the double-shielded computer cable to the earmuff enclosure.

3A.6.4. Power, grounding, sound input, and amplifier shield connections

Power was provided by a single 9.6V 1800 mA-hour Ni-Cd battery (Radio Shack Corp., Fort Worth, TX). Since the battery is ferromagnetic, it was kept outside the shielded room and brought in through the penetration panel through an unfiltered BNC port, connecting the positive terminal of the battery to the BNC signal conductor and the negative terminal of the battery to the BNC shield. In this way the power reference of the headphone amplifier was connected to the shielded room reference. A copper mesh shield was constructed for the Koss amplifier system with a interconnect system to connect the headphone shield cable to the amplifier shield, which was in turn connected to the battery/shielded-room reference. This arrangement is depicted in **Figure 3A.6.6**.

Sound was delivered using the 1/8" stereo jack at the front of the Koss amplifier unit, brought into the shielded room through a filtered DB-9 in the penetration panel.

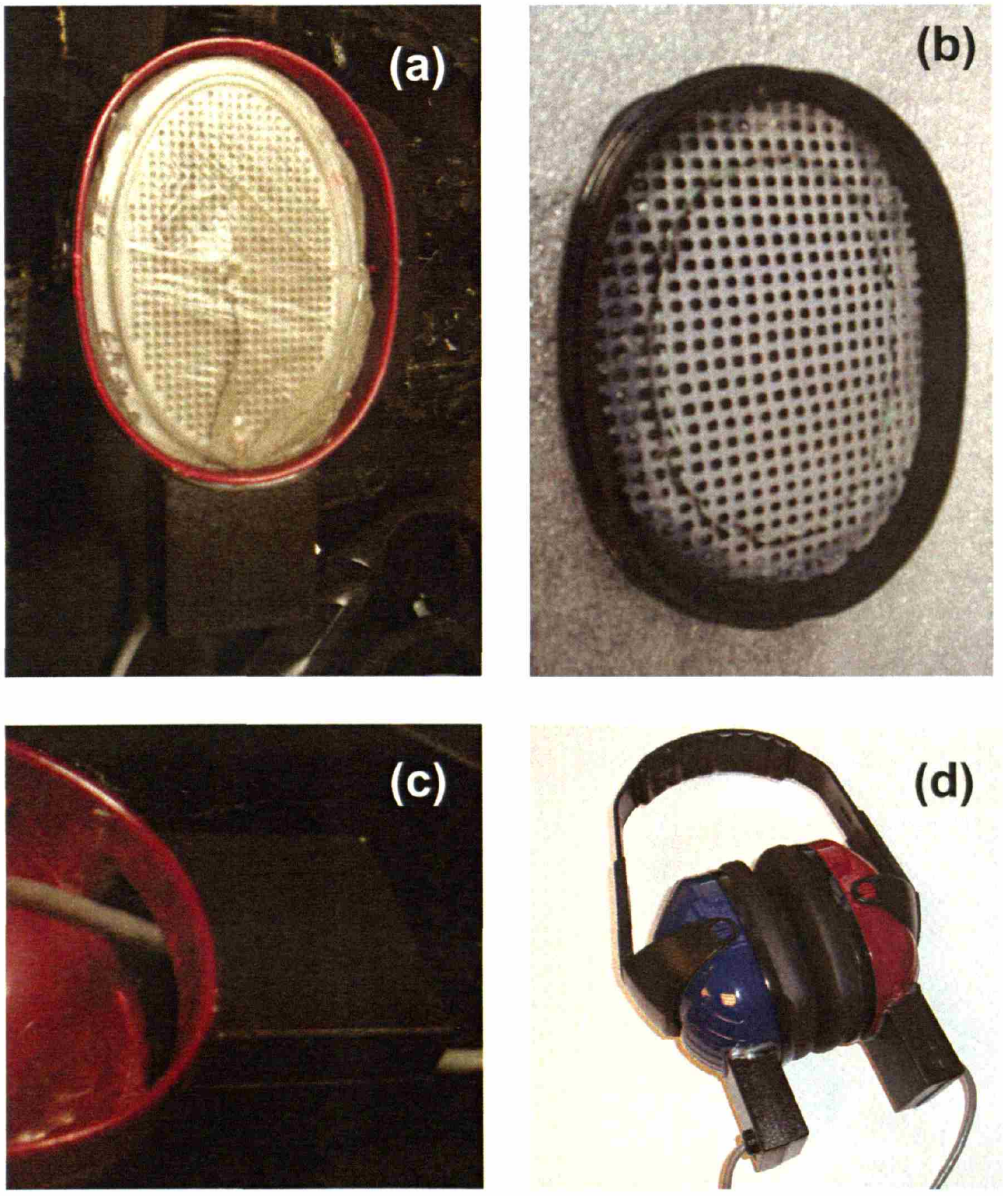

Figure 3A.6.1. Sound-attenuating headphone enclosures: (a) Internal view with electrostatic headphone elements in place; (b) Plastic grille secured within ear cushion; (c) Detail of aperture and box for headphone element connectors; (d) External view of enclosures fully assembled.

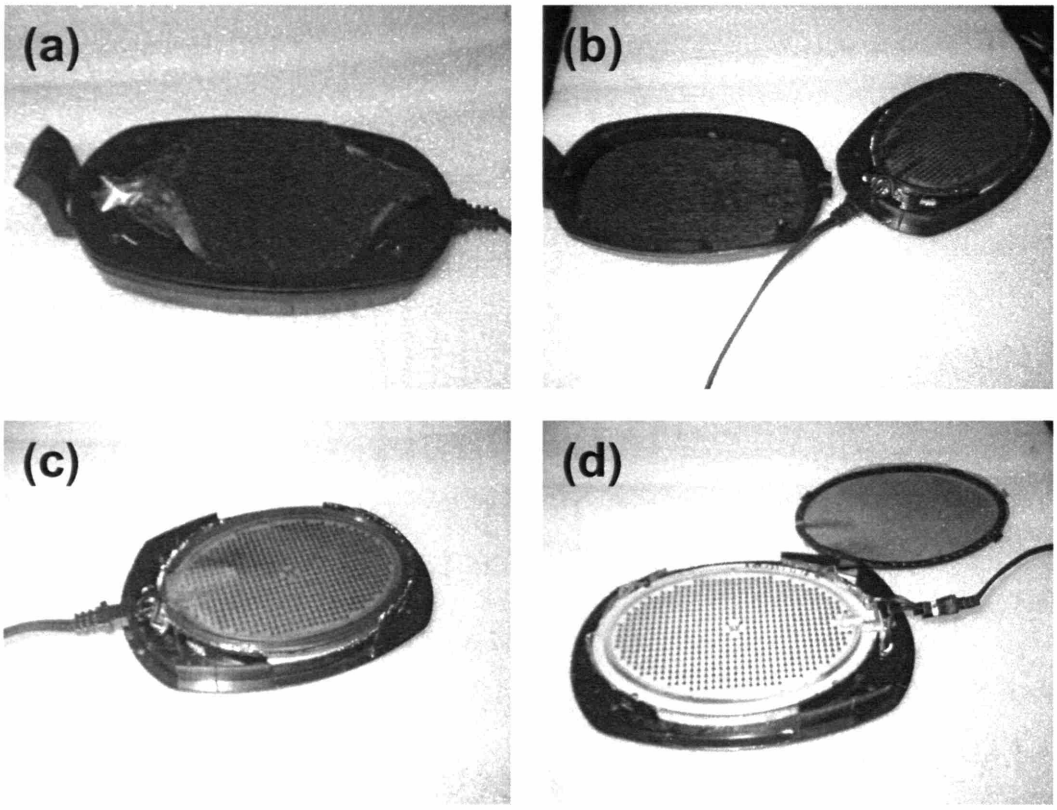

Figure 3A.6.2. Extraction of electrostatic elements from Koss ESP-950 headphones: (a) Exposure and removal of enclosure screws; (b) Separation of enclosure halves; (c) Retainer ring and protective mesh; (d) Removal of retainer ring and protective mesh, revealing electrostatic element, which can be snapped out of enclosure.

Connector Numbering (facing pin connector):

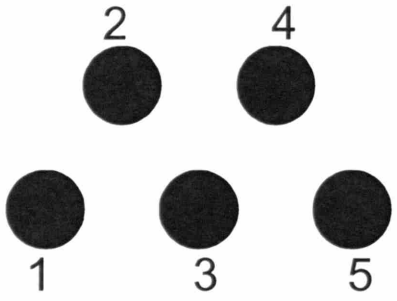

Pin #	Cable Color	Connection
1	Red	Right Inner Plate
2	Green	Right Outer Plate
3	Orange	Center Plate (R and L)
4	Yellow	Left Outer Plate
5	White	Left Inner Plate

("Inner" = closest to ear, "outer" = farthest from ear)

Figure 3A.6.3. Wiring chart for re-connecting electrostatic headphone elements. Wire colors refer to colors of inner insulators of original Koss cabling.

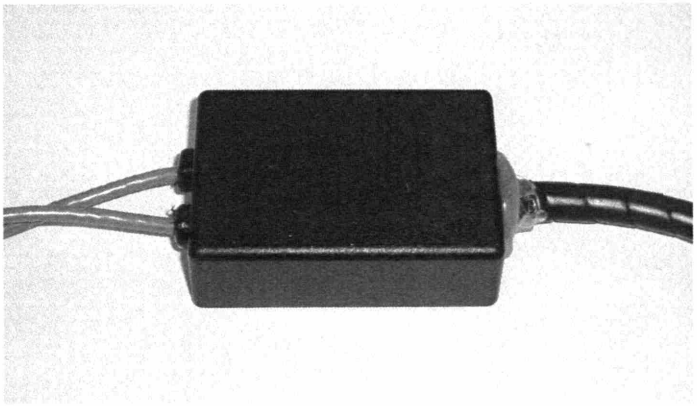

Figure 3A.6.4. Junction box showing shielded cable strain relief with Heyco connectors and spiral wrap cable protection.

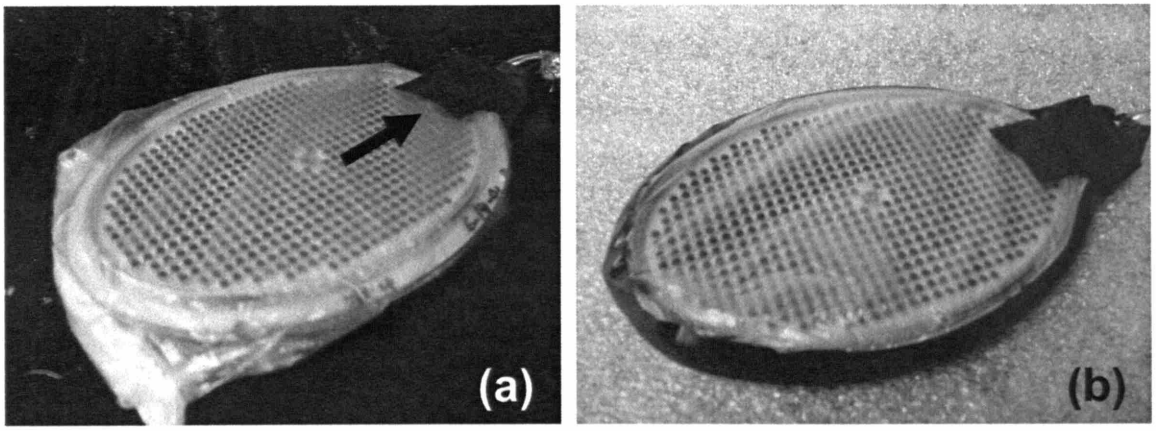

Figure 3A.6.5. Insulation for electrostatic headphone elements: Electrical connectors are protected by large-diameter shrink tubing (not shown); (a) Electrostatic element is sealed within thin single-layer plastic insulation and electrical tape is placed over conductors not covered by shrink tubing, illustrated by the arrow; (b) Edges of plastic insulation reinforced with electrical tape to protect against abrasion within headphone enclosure.

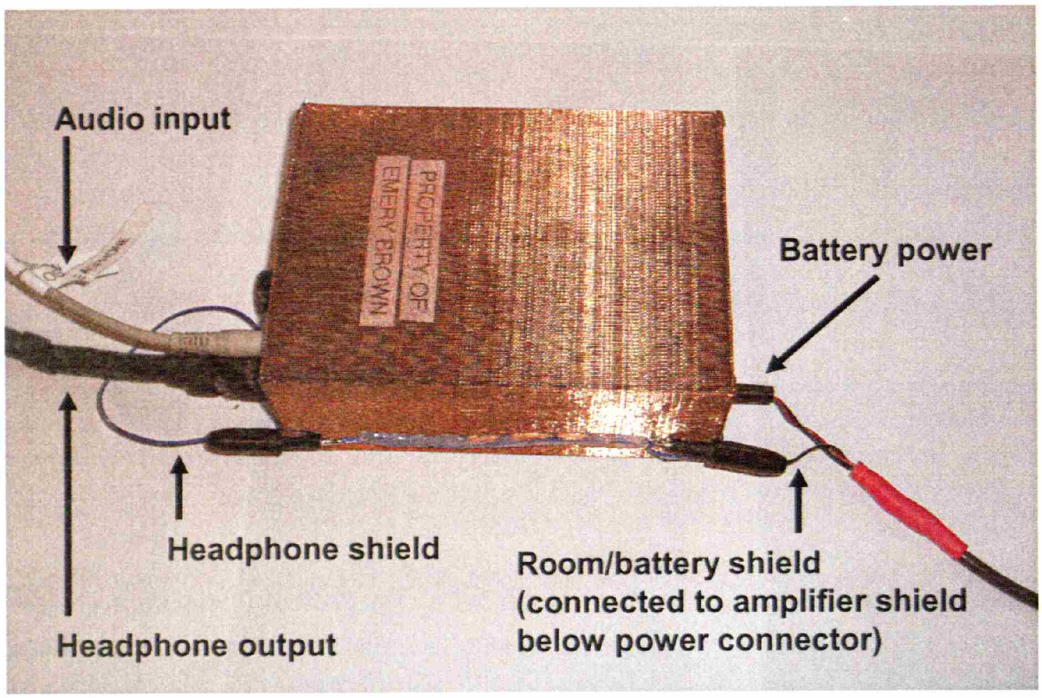

Figure 3A.6.6. Shield, ground, power, and audio inputs for modified Koss amplifier system.

3.7. References

1. Angelone, L. M. and Bonmassar, G. Use of resistances and resistive leads: Implications on computed electric field and SAR values. Proc.12th ISMRM , 1652. 2004.

2. Bishop RH (2001) Learning With Labview 6i. Upper Saddle River: Prentice Hall.

3. Bonmassar G, Anami K, Ives J, Belliveau JW (1999) Visual evoked potential (VEP) measured by simultaneous 64-channel EEG and 3T fMRI. Neuroreport 10: 1893-1897.

4. Burr-Brown Products. ADS1254: 24-bit, 20kHz, low power analog-to-digital converter. SBAS213. 2001. Dallas, TX, Texas Instruments, Inc.

5. Garreffa G, Bianciardi M, Hagberg GE, Macaluso E, Marciani MG, Maraviglia B, Abbafati M, Carni M, Bruni I, Bianchi L (2004) Simultaneous EEG-fMRI acquisition: how far is it from being a standardized technique? Magn Reson Imaging 22: 1445-1455.

6. Goldman RI, Stern JM, Engel J, Jr., Cohen MS (2000) Acquiring simultaneous EEG and functional MRI. Clin Neurophysiol 111: 1974-1980.

7. Ives JR, Warach S, Schmitt F, Edelman RR, Schomer DL (1993) Monitoring the patient's EEG during echo planar MRI. Electroencephalogr Clin Neurophysiol 87: 417-420.

8. Lemieux L, Allen PJ, Franconi F, Symms MR, Fish DR (1997) Recording of EEG during fMRI experiments: patient safety. Magn Reson Med 38: 943-952.

9. Liebenthal E, Ellingson ML, Spanaki MV, Prieto TE, Ropella KM, Binder JR (2003) Simultaneous ERP and fMRI of the auditory cortex in a passive oddball paradigm. Neuroimage 19: 1395-1404.

10. Linear Technology Corporation. LT1167: Single resistor gain programmable, precision instrumentation amplifier. 1167fa LT/TP 0301 2K REV A. 1998. Milpitas, CA, Linear Technology Corporation.

11. Mirsattari SM, Ives JR, Bihari F, Leung LS, Menon RS, Bartha R (2005) Real-time display of artifact-free electroencephalography during functional magnetic resonance imaging and magnetic resonance spectroscopy in an animal model of epilepsy. Magn Reson Med 53: 456-464.

12. Percival DB, Walden AT (1993) Spectral analysis for physical applications. New York: Cambridge University Press.

13. Vanni S, Dojat M, Warnking J, Delon-Martin C, Segebarth C, Bullier J (2004) Timing of interactions across the visual field in the human cortex. Neuroimage 21: 818-828.

14. Vasios, C. E., Angelone, L. M., Purdon, P., Belliveau, J. W., and Bonmassar, G. EEG measurements at 7T Tesla using the ink cap. 13th ISMRM (submitted). 2005.

Chapter 4
Adaptive filtering methods for removal of ballistocardiogram noise and motion artifacts

4.1. Introduction

Simultaneous recording of EEG and fMRI is an important, emerging tool in functional neuroimaging that combines the high spatial resolution of fMRI with the high temporal resolution of EEG. A fundamental limitation of this combined technique is the noise introduced in the EEG due to motion within the magnetic field, either from cardiac pulsation (ballistocardiogram) or from head movements (Huang-Hellinger et al., 1995). The ballistocardiogram noise obscures EEG activity at alpha frequencies (8-13 Hz) and below, with amplitudes sometimes in excess of 150 μV at 1.5 T field strength, much larger than the alpha waves seen in most subjects (~ 50μV). Head rotations and translations, present in longer recordings or in recordings of patients with certain neurological disorders, result in even larger disturbances to the EEG. In evoked-potential studies, these large-amplitude disturbances result in rejection of epochs, increasing the duration of such experiments due to lost data, and making recordings from subjects who

possess large ballistocardiogram waveforms practically impossible. In EEG-fMRI studies of epilepsy, it is essential to have clinically interpretable EEG from which to identify epileptic spikes, either in real-time for spike-triggered studies (Huang-Hellinger et al., 1995), or in post-processing to generate hemodynamic response waveforms for fMRI analysis (Lemieux et al., 2001). Ballistocardiogram and motion-induced noise can make these epileptic events difficult to detect with precision. In sleep or anesthesia studies, identification of delta (0.5-4 Hz) and alpha waves is essential (Portas et al., 2000;Rampil, 1998), yet the ballistocardiogram artifact directly obscures these frequency ranges. Because these sources of noise are the direct result of electromagnetic induction within the static magnetic field, the problem becomes worse at higher field strengths such as 3, 4, or 7T.

One method for removing the ballistocardiogram noise is to subtract an average ballistocardiogram template created from the EEG data itself (Allen et al., 1998;Sijbersa et al., 2000), using a limited window of past data to construct the averaged waveform. This template subtraction method relies heavily on accurate ECG peak detection: If ECG peak detection is inconsistent, accurate subtraction templates cannot be formed, and furthermore time epochs from which to subtract the template cannot be correctly identified, resulting in large residual noise signals. At higher field strengths such as 3, 4 or 7 Tesla, ECG recordings become increasingly difficult to record cleanly. Chest motion from respiration, chest vibration from cardiac pulsation, and Hall-effect artifacts from aortic flow produce signal artifacts that distort and obscure the R-wave. Furthermore, the "average-waveform" method cannot remove motion artifacts, and would be cumbersome to implement in real-time, which limits its potential usefulness in

EEG-triggered MRI applications. ICA-based methods have been developed recently to remove ballistocardiogram artifacts (Srivastava et al., 2005), but these methods are designed for short epochs of data, primarily for ERP studies, and are not suitable for continuous recordings for sleep, epilepsy, or anesthesia. Furthermore, if the EEG signals of interest are similar in amplitude to the ballistocardiogram noise, separation of independent signal components over noise components can be problematic, since noise components can no longer be identified solely by their large amplitudes.

In this chapter, we present a method for adaptive noise cancellation of the ballistocardiogram artifact employing a novel motion sensor system that functions robustly at 1.5, 3, and 7T. The proposed method is capable of removing both ballistocardiogram and motion-induced noise simultaneously in a way that lends itself naturally to real-time implementation. We demonstrate its efficacy in recordings and simulation studies in the static magnetic field or during interleaved EEG-fMRI at 1.5, 3 and 7T field strengths.

4.2. Materials and Methods

4.2.1 Overview of EEG-fMRI recordings

To evaluate the performance of our algorithm, we collected EEG data sets containing alpha waves, VEPs, and head motion, within the static magnetic field, during interleaved EEG/fMRI scanning at 1.5, 3, and 7 T (Siemens, Erlangen, Germany), and at earth magnetic field strength outside the MRI. In addition, we collected anatomic MRI images to confirm that the novel motion sensing hardware did not introduce imaging

artifacts. All study subjects provided informed consent in accordance with Massachusetts General Hospital policies (MGH IRB numbers 1999-P-010946/1 and 2002-P-001703).

4.2.1.a. EEG Acquisition

EEG recordings were performed at 3 and 7T using a 24-bit electrophysiological recording system featuring low noise and high dynamic range to prevent saturation during imaging, with a sampling rate of 957 Hz and a bandwidth of DC to 500 Hz. Data were displayed, recorded, and integrated with stimulus triggers using data acquisition software written in the LabView development environment (National Instruments). For 3T recordings, EEG electrodes were placed in adjacent bipolar pairs along a coronal plane (M2→T8, T8→C6, C6→C4, C4→Cz, Cz→C3, C3→C5, C5→T7, T7→M1) using Ag/Ag-Cl electrodes featuring a plastic housing (Gereonics, Inc., Solana Beach, CA) bonded to carbon fiber wires ("Fiber-Ohm" wires with 7 ohms/inch resistance; Marktek, Inc., Chesterfield, MO) with conductive epoxy. For 7T recordings, EEG was recorded using a 32-channel EEG cap featuring resistive EEG leads made from conductive inks printed onto flex-circuit material (Vasios et al., 2005), with a referential montage featuring a single reference on the left mastoid. EEG was recorded at 1.5 T using a 32-channel OptiLink EEG system (Neuro Scan Labs, Sterling, VA), amplified using SynAmps (Neuro Scan Labs), acquired using Scan 4.1 software at a rate of 1000 Hz with a bandwidth of 0.5 Hz to 35 Hz, using a 32-channel MRI compatible Quickcap (Neuro Scan Labs) modified to provide a short-chained bipolar montage (Schomer et al., 2000).

4.2.1.b. Motion Sensor Recordings

To provide a reference signal for adaptive noise cancellation, a set of motion sensors were constructed from Murata PKM11-4A0 piezo-electric sensors (Murata

Electronics North America, Inc., Smyrna, GA), replacing soldered metallic leads with carbon fiber leads (Marktek) bonded with conductive epoxy. To maximize mechanical coupling to the cardiac pulsation of the head, sensors were placed in the vicinity of the temporal artery, held in position either by tape, surgical netting, or the EEG cap material, with light pressure applied using small cushions placed between the head coil and the subject's head. Motion sensor signals were acquired using the same amplification and acquisition system as the EEG.

4.2.2. Signal Processing Methods

4.2.2.a. Adaptive Filtering

We model the recorded EEG signal y_t as the sum of a noise signal n_t containing motion and ballistocardiogram components and a "true" underlying EEG signal v_t:

$$y_t = n_t + v_t \tag{4.1}$$

The relationship between the noise signal n_t and the motion sensor signal u_t is represented by a linear time-varying finite impulse response (FIR) model $x_{t,k}$,

$$\begin{aligned} n_t &= \sum_{k=0}^{N-1} x_{t,k} u_{t-k} = \mathbf{u}_t^T \mathbf{x}_t \\ \mathbf{u}_t^T &= [u_t \quad u_{t-1} \quad \cdots \quad u_{t-(M-1)}] \\ \mathbf{x}_t^T &= [x_{t,0} \quad x_{t,1} \quad \cdots \quad x_{t,(M-1)}] \end{aligned} \tag{4.2}$$

where N is the order of the FIR kernel. The dynamics of the FIR system are modeled as a random walk

$$\mathbf{x}_t = \mathbf{x}_{t-1} + \mathbf{w}_t, \tag{4.3}$$

where $\mathbf{w}_t$ represents a random state noise. We model the underlying EEG signal v_t and state noise $\mathbf{w}_t$ as independent jointly-Gaussian processes

$$\begin{bmatrix} w_t \\ v_t \end{bmatrix} \sim N\left(0, \begin{bmatrix} \Sigma_w & 0 \\ 0 & \sigma_v^2 \end{bmatrix}\right). \qquad (4.4)$$
$$\Sigma_w = \sigma_w^2 I_M$$

Given the observed signal y_t, reference signal u_t, and the noise variances σ_v^2 and σ_w^2, we estimate the terms of the FIR model recursively using the Kalman filter (Anderson and Moore, 1979;Haykin, 2002), discussed briefly in Appendix 4A. We use the prediction estimates $\hat{\mathbf{x}}_{t|t-1}$ at each step to estimate the noise term n_t,

$$\hat{n}_t = \mathbf{u}_t^T \hat{\mathbf{x}}_{t|t-1}, \qquad (4.5)$$

recovering an estimate of the true signal $\hat{v}_t$,

$$\hat{v}_t = y_t - \hat{n}_t. \qquad (4.6)$$

For studies at 1.5 T, signals were downsampled by a factor of 10 to 100 Hz prior to adaptive filtering. For studies at 3 and 7 T, signals were downsampled by a factor of 8 to approximately 120 Hz. Computational details are overviewed in Appendix 4A.

4.2.2.b. Adaptive Filter Parameter Estimation

The noise variances σ_v^2 and σ_w^2 are unknown parameters and must be set properly for effective adaptive filtering and noise cancellation. An EM algorithm (McLachlan and Krishnan, 1997) was developed to estimate these variances from a short segment of data (~17 sec) for each channel of EEG. The FIR filter components $\mathbf{x}_t$ were treated as the unobserved component of a complete data likelihood consisting of both $\mathbf{x}_t$ and y_t, parameterized by σ_v^2 and σ_w^2. The conditional expectations in the E-step of the EM algorithm were computed using the fixed-interval smoother (Appendix 4B). The derivation of the EM algorithm is presented in Appendix 4C.

4.2.2.c. Motion Sensor Selection Using Coherence Estimation

The performance of the adaptive noise cancellation algorithm depends strongly on the quality of the motion sensor reference signal. Poor mechanical contact with the study subject's head can result in a noisy or low-amplitude motion signal, and physical damage to the piezoelectric element from repeated use can also reduce motion signal quality. In practice, 2 to 4 motion sensors are used for every recording to ensure that an adequate motion signal was available for every recording. Motion sensor signal quality was assessed by examining the coherence between the motion signal and EEG channels of interest. The coherence $C_{uy}(\omega)$ quantifies the correlation between the signals u_t and y_t as a function of frequency (Priestley, 1982), and is defined as

$$C_{uy}(\omega) = \frac{\left|P_{uy}(\omega)\right|^2}{P_{uu}(\omega)P_{yy}(\omega)} \tag{4.7}$$

where $P_{uy}(\omega)$ is the cross-spectral density, and $P_{uu}(\omega)$ and $P_{yy}(\omega)$ are the power spectral densities of u_t and y_t. The coherence assumes values between 0 and 1 and can be thought of as a frequency-specific correlation coefficient. A large coherence between u_t and y_t at a given frequency indicates that there is a strong linear correlation between u_t and y_t at that frequency, while a small coherence suggests the opposite. Since the coupling between motion and ballistocardiogram is modeled as a linear relationship, the coherence in frequency bands with large ballistocardiogram noise should be predictive of adaptive filter performance. As a diagnostic metric, the coherence was useful for identifying misplaced or malfunctioning motion sensors during baseline recordings prior to fMRI scanning, and for selecting the best motion signal to use in adaptive filtering for a given EEG channel. The coherence method was estimated using a multi-taper method

in order to precisely control the bandwidth of the spectral estimates (set to < 1 Hz in practice) (Percival and Walden, 1993). Computational details for coherence estimation are provided in Appendix 4D.

4.2.2.d. Performance Calculations

The most commonly used metric of adaptive filter performance is the residual mean-squared error (MSE)(Haykin, 2002):

$$MSE = \sum_{t} \left(y_t - \hat{n}_t \right)^2 . \tag{4.8}$$

While the MSE is convenient both computationally and analytically, in practical applications it can misrepresent filter performance: Filters that remove both "true" signal components as well as noise components will have a lower MSE than those that remove only noise components while preserving "true" signal components. An alternative is to quantify improvements in signal-to-noise (SNR) where the true underlying signal is known. This can be accomplished by analyzing simulated data sets where a known signal is added to resting-state EEG data containing ballistocardiogram artifacts.

For an oscillatory signal that modulates between periods of full amplitude ("ON") and zero amplitude ("OFF"), we define the signal to noise as

$$SNR(\omega) = \frac{\overline{P}_{ON}(\omega)}{\overline{P}_{OFF}(\omega)}, \tag{4.9}$$

where $\overline{P}_{ON}(\omega)$ represents the average power spectrum in the signal when the oscillatory signal is ON, and $\overline{P}_{OFF}(\omega)$ represents the average power spectrum in the signal when the oscillatory signal is OFF. To calculate the SNR in a specific frequency band Ω, we compute the SNR in-band as:

$$SNR_{\Omega} = \frac{1}{|N_{\Omega}|} \sum_{\omega \in \Omega} SNR(\omega), \tag{4.10}$$

where N_{Ω} is the number of discrete frequency components within the band Ω. To assess filtering performance, we compare the SNR before and after filtering and compute the SNR gain in the band Ω as:

$$G_{\Omega} = \frac{SNR_{\Omega}(\text{BEFORE FILTERING})}{SNR_{\Omega}(\text{AFTER FILTERING})}. \tag{4.11}$$

4.2.3. Simulation Studies

4.2.3.a. SNR Performance Comparison Using Resting State EEG with Sinusoidal Test Signals

For investigations related to sleep, anesthesia, and resting-state brain activity, EEG-fMRI studies are designed to estimate time-varying fluctuations in oscillatory power in the delta, theta, alpha, beta, and gamma bands and their relationship to BOLD responses (Goldman et al., 2002;Laufs et al., 2003a;Laufs et al., 2003b). Ballistocardiogram noise corrupts signals in the alpha band and below (< 12 Hz). To study the signal-to-noise performance of the adaptive filtering algorithm, sinusoidal test signals were added to resting state EEG data and SNR calculations were performed as described in Section 4.2.2.e. Resting state EEG data were collected from two study subjects inside the 3T scanner with simultaneous ECG to provide data for comparison with the subtraction method. Each study subject was asked to lay awake and motionless in the scanner for approximately 5 minutes with eyes open. ECG was recorded with an InVivo Magnitude MRI-compatible patient monitor using the InVivo Quattrode electrode system (InVivo Research, Orlando, FL). The ECG signal was acquired using a National

Instruments DAQCard 6024E 16-bit analog acquisition card, integrated and synchronized with 24-bit EEG acquisition using LabView.

For each of the two study subjects, two simulated data sets were created, one with an alpha-band signal (10 Hz) and another with a delta-band signal (3 Hz). Each test signal was modulated in an ON-OFF pattern, 8.5 seconds ON, 8.5 seconds OFF, with a total of 16 ON-OFF repeats over a total of 274 seconds. For each channel of each data set, filter parameters were estimated using the EM algorithm described in Section 4.2.2.b and Appendix 4C from the first 17 second ON-OFF period. The adaptive filter was then applied using the corresponding estimated filter parameters. The data were also analyzed using the subtraction method (Allen et al., 1998), as implemented in Brain Vision Analyzer 1.05 (Brain Products GMBH, Munich, Germany), using R-wave peak detection and a 0.21 second delay between R-wave peak and ballistocardiogram artifact.

The power spectra for each 8.5 second block were estimated using the multitaper method with a bandwidth of 1 Hz and smoothing parameter of NW = 4.28 (Percival and Walden, 1993) and were used to calculate $\overline{P}_{ON}(\omega)$ and $\overline{P}_{OFF}(\omega)$ for the adaptive filtered data, the subtraction method data, and the original ballistocardiogram data. The SNR in-band SNR_{Ω} and SNR gain G_{Ω} were then computed and compared.

4.2.3.b Simulations of epileptic activity within EEG data corrupted by head motion

Time-domain identification of epileptic spikes is another important objective for EEG-fMRI studies, both as a way of spike-triggering fMRI scans in real-time (Huang-Hellinger et al., 1995), or for identifying spikes in post-processing in order to generate hemodynamic response waveforms for fMRI analysis (Lemieux et al., 2001). Since epileptic spikes are usually large (~10^2 uV) compared to ballistocardiogram, head

movement-related EEG artifacts pose a larger challenge for time-domain spike identification. To test the efficacy of the adaptive filtering algorithm in removing head movement artifacts from epileptic spiking data, simulated biphasic epileptic spikes (Nunez, 1995) with approximately 400 μV peak-to-peak amplitude and 100 msec duration were randomly added to EEG data recorded in the magnet containing head movement. The head movement data was generated by asking two subjects to lie quietly in the 1.5 T scanner with eyes open while nodding his or her head slightly (a few millimeters displacement) once every 7 to 10 seconds over a five-minute period.

4.2.4. Real data examples

4.2.4.a. Evaluation of Motion Signal Quality Using Coherence Estimates

A broken motion sensor was identified from repeated recordings where the sensor produced a periodic signal time-locked to the heart beat, but with an altered morphology and visibly reduced adaptive filter performance. Five minutes of resting state EEG data were recorded at 3T using this broken motion sensor on one side of the head, and a normally-functioning motion sensor on the other side of the head. This data set was used to evaluate the use of coherence estimates for motion sensor selection and quality control. Adaptive filtering was performed on a single channel of EEG, using the broken motion sensor in one case, and the normal motion sensor in another. The power spectra of the original EEG data, filtered data using the broken sensor, and filtered data using the normal sensor were estimated using the multitaper method with a bandwidth of 1 Hz and a smoothing parameter NW of 8.5. Coherence spectra between the EEG data and each motion sensor were also calculated using identical multitaper parameters.

4.2.4.b. Visual EEG-fMRI

Visual evoked potential (VEP) measurements were performed at 1.5T during interleaved fMRI. A set of control VEP data was also recorded at earth magnetic field strength. Visual stimuli consisted of 15 seconds of a full-field black and white checkerboard pattern reversing at 2 Hz, followed by 15 seconds of uniform gray field, with a 100-msec jitter. In all conditions, a central fixation spot was present. The 10×10-checkerboard pattern (25° × 25°) was rear-projected by a LCD projector, through a collimating lens onto an acrylic screen (40° × 25°). An SGI-O_2 workstation generated the visual stimulus and sent synchronized triggers to the scanner and to the SynAmps to tag the stimulus events for subsequent binning, temporal epoching and averaging. Epoch selection was performed by comparing the maximum voltage excursion of each epoch for each active channel to the ± 50 μV threshold level, rejecting epochs that exceeded this threshold.

Anatomical MRI was performed using a quadrature birdcage receive-only head coil on a 1.5 T scanner. For each subject, three whole-head acquisitions were collected using a T1 weighted 3D-SPGR (TR/TE = 24 ms/8 ms) sequence with 124 slices, 1.3 mm thick (matrix size 256×192, FOV 25 cm). _Functional MRI was performed with the same 1.5 T scanner and head coil used for the anatomical MRI acquisition. The first echo planar imaging (EPI) sequence was a T1-weighted spin-echo inversion recovery (TR/TE/TI = 2s / 20 ms / 800 ms) used to acquire 10 slices (7 mm-thick, 1 mm gap, 1.56 mm × 1.56 mm in-plane resolution) oriented perpendicular to the calcarine fissure. These images were later used to coregister the functional data with the subject's anatomical MRI set. Functional MRI data were acquired from those same slices using a gradient

echo sequence (TE/TR = 50 ms/1000 ms) with the same slice thickness and gap, but 3.1 mm × 3.1 mm in-plane resolution. EEG and fMRI were interleaved in alternating 30-second blocks of EEG followed by 30-seconds of continuous fMRI, with each 30-second block consisting of a 15-second fixation period and a 15-second flashing checkerboard period. Each EEG/fMRI run lasted 15 minutes, with two runs per subject. Two subjects were studied using this paradigm.

4.2.1.d. Alpha Wave Recordings

To record alpha waves, subjects were instructed to lie quietly in the magnet with eyes open for 10 seconds, followed by 20 seconds with eyes closed (Nunez, 1995). To produce an adequate visual stimulus during the eyes open segment, the lights in the room and within the magnet bore were turned on throughout the experiment. This paradigm was repeated over a 3-minute (1.5 T) or 4-minute (7 T) period to produce several alpha wave epochs. Additional alpha wave recordings were made outside the scanner (1.5 T) using the same paradigm. Five subjects were studied at 1.5 T and 4 subjects at 7 T.

4.3. Results

4.3.1. Simulation Studies

4.3.1.a. SNR Performance Comparison: Adaptive Filtering Improves SNR in-band by up to 676%

SNR gain calculations for both the adaptive filter and the subtraction method are presented in **Table 4.1** for each channel of each data set studied. In some instances the adaptive filter produced small reductions in SNR (Worst case: Subject 2, channel C4→ Cz, $G_\alpha = 0.78$), but the overwhelming effect of the filter was to improve SNR in-band by a large proportion, with greater than 600% improvement in some cases. Inspection of power spectra before and after filtering in cases with low SNR gain showed that these channels possessed low noise power in the frequency bands being studied, while those with high SNR gain had high noise power in those bands. In contrast, the subtraction method produced smaller improvements in SNR gain, with a maximum SNR improvement of 68%. In a large number of cases, the subtraction method reduced SNR in band by a large fraction (up to -64%). Visual inspection of ECG traces for these channels showed that poor performance could be attributed directly to mis-identification of ECG peaks, resulting in inaccurate estimation of ballistocardiogram template waveforms, as well as subtraction of those templates from inappropriate epochs of the data. **Figure 4.1** illustrates the performance of both methods in time-frequency domain, showing spectrograms of simulated delta signals (Subject 1, channel M2→T8) before and after processing with both the adaptive filter and the subtraction algorithm. Prior to filtering, the delta-band test signal is difficult to identify, but after adaptive filtering, it is easy to discern, with a clear improvement in SNR in-band. The subtraction method

improves SNR over some segments of the test data, but fails to improve SNR in other sections, resulting in poor overall performance.

Subject 1 Alpha Waves											
	Channel										
SNR Gain	M2-->T8	T8-->C6	C6-->C4	C4-->Cz	Cz-->C3	C3-->C5	C5-->T7	T7-->M1	Avg	Max	Min
Adaptive Filter	0.93	1.44	1.78	1.11	0.89	1.98	2.68	2.50	1.66	2.68	0.89
Subtraction Alg.	0.36	0.71	0.70	0.52	0.36	0.51	0.63	1.03	0.60	1.03	0.36
Subject 2 Alpha Waves											
	Channel										
SNR Gain	M2-->T8	T8-->C6	C6-->C4	C4-->Cz	Cz-->C3	C3-->C5	C5-->T7	T7-->M1	Avg	Max	Min
Adaptive Filter	3.53	2.55	1.99	0.78	0.95	2.58	2.17	1.14	1.96	3.53	0.78
Subtraction Alg.	1.02	0.94	0.90	0.36	0.46	1.02	0.95	1.06	0.84	1.06	0.36
Subject 1 Delta Waves											
	Channel										
SNR Gain	M2-->T8	T8-->C6	C6-->C4	C4-->Cz	Cz-->C3	C3-->C5	C5-->T7	T7-->M1	Avg	Max	Min
Adaptive Filter	7.49	3.77	5.19	3.75	4.28	3.77	7.76	5.24	5.16	7.76	3.75
Subtraction Alg.	1.13	1.02	0.99	0.96	0.90	0.74	1.05	1.07	0.98	1.13	0.74
Subject 2 Delta Waves											
	Channel										
SNR Gain	M2-->T8	T8-->C6	C6-->C4	C4-->Cz	Cz-->C3	C3-->C5	C5-->T7	T7-->M1	Avg	Max	Min
Adaptive Filter	1.69	0.96	0.86	1.04	0.86	1.00	1.19	1.68	1.16	1.69	0.86
Subtraction Alg.	1.21	1.09	0.95	0.80	0.69	1.07	1.21	1.33	1.04	1.33	0.69

Table 4.1. SNR Gain Comparison of Adaptive Filter vs. Subtraction Method.

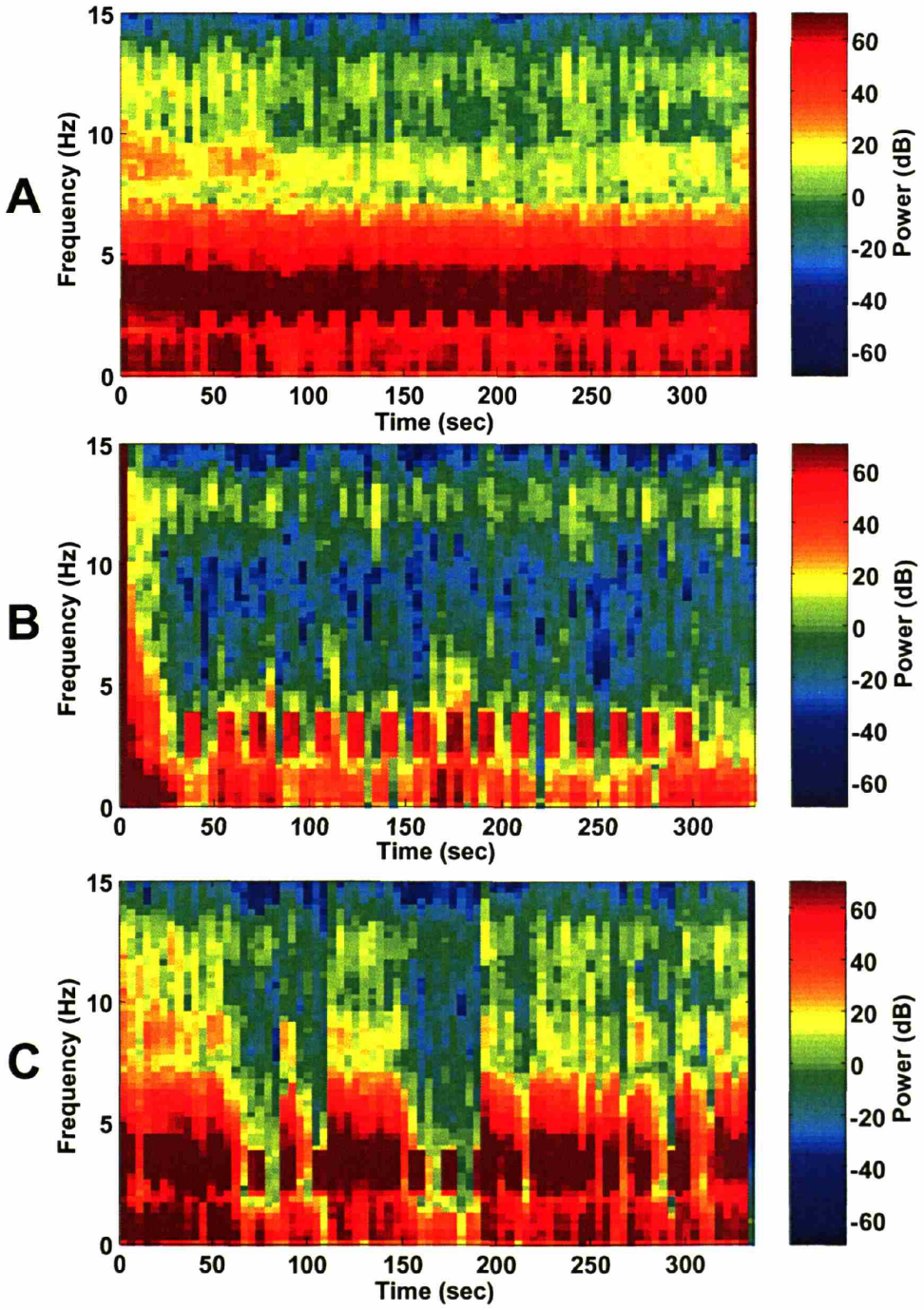

Figure 4.1. Performance comparison of adaptive filter with template subtraction method, using spectrograms of simulated delta signals (Subject 1, channel M2→T8). A 10 uV simulated delta-band signal (3 Hz) was added to resting-state EEG data in an 8.5-second ON, 8.5-second OFF pattern. Prior to filtering (top), the delta-band test signal is difficult to identify, but after adaptive filtering (middle), it is easy to discern, with a clear improvement in SNR in-band. The subtraction method (bottom) improves SNR over some segments of the test data, but fails to improve SNR in other sections, resulting in poor overall performance.

4.3.1.b. Adaptive Filtering Can Recover Epileptic Spikes from Movement-Corrupted EEG Data

The adaptive filter can also be used to remove gross motion-artifacts on the EEG to reveal hidden simulated epileptic spikes, as demonstrated in **Figure 4.2**. Prior to adaptive filtering, the simulated epileptic spikes are hidden by head movement artifacts, but after filtering, the hidden spikes are recovered, as indicated by the arrows.

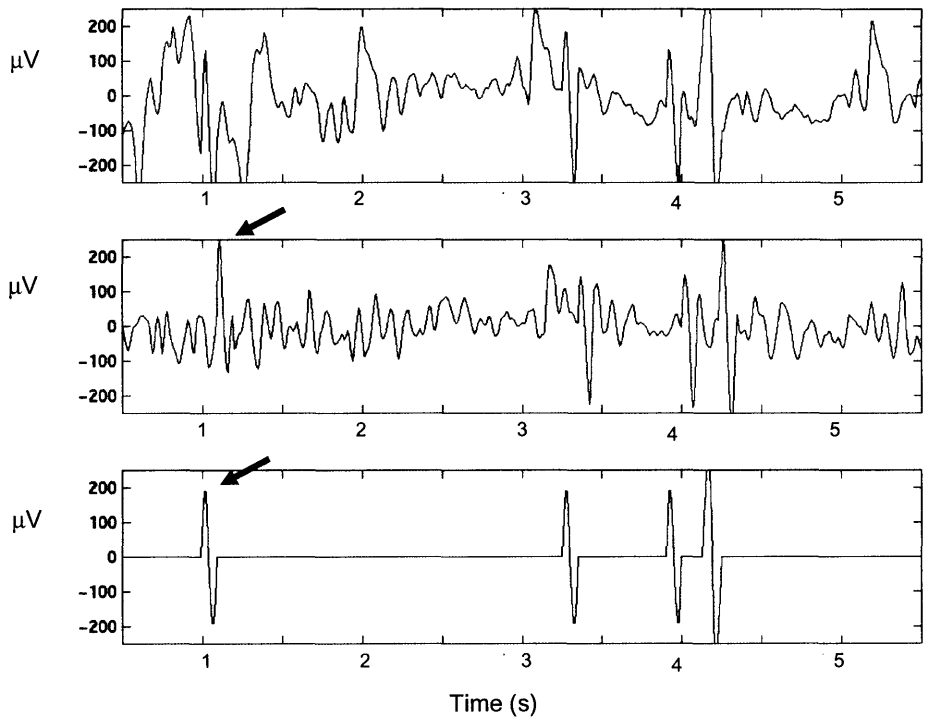

Figure 4.2. Adaptive filtering of movement artifacts in simulated epileptic spiking data. The adaptive filter can be used to remove gross motion-artifacts on the EEG to reveal hidden simulated epileptic spikes. Simulated biphasic epileptic spikes with approximately 400 μV peak-to-peak amplitude and 100 msec duration were randomly added to EEG data recorded in the magnet containing head movement. The head movement data was generated by asking two subjects to lie quietly in the 1.5 T scanner with eyes open while nodding his or her head slightly once every 7 to 10 seconds over a five-minute period. Prior to adaptive filtering (top), the simulated epileptic spikes are hidden by head movement artifacts, but after filtering (bottom), the hidden spikes are recovered, as indicated by the arrows.

4.3.2. Real Data Examples

4.3.2.a. Coherence Estimates Predict Adaptive Filtering Performance

Coherence estimates can be used to select motion sensors for use in adaptive noise cancellation, identifying both good and bad motion sensors, as illustrated in **Figure 4.3**. The broken ("bad") motion sensor shows a noticeable band of low coherence centered at 3 Hz (middle), a frequency that contains a substantial amount of ballistocardiogram noise power (top), as shown in the EEG power spectrum. In contrast, the "good" motion sensor has high coherence through the ballistocardiogram band (middle). Residual power after adaptive filtering with the "bad" motion sensor reveals a large residual peak centered at 3 Hz, while the good motion sensor had negligible residual power at this frequency (bottom). Inspection of the time-domain residuals shows the large low-frequency residual noise present after filtering with the "bad" motion sensor (**Figure 4.4**). These calculations demonstrate that coherence estimates can predict adaptive filtering performance and can be used to select motion sensors for noise cancellation, and to diagnose potential problems with motion sensor placement prior to commencing an EEG-fMRI scan.

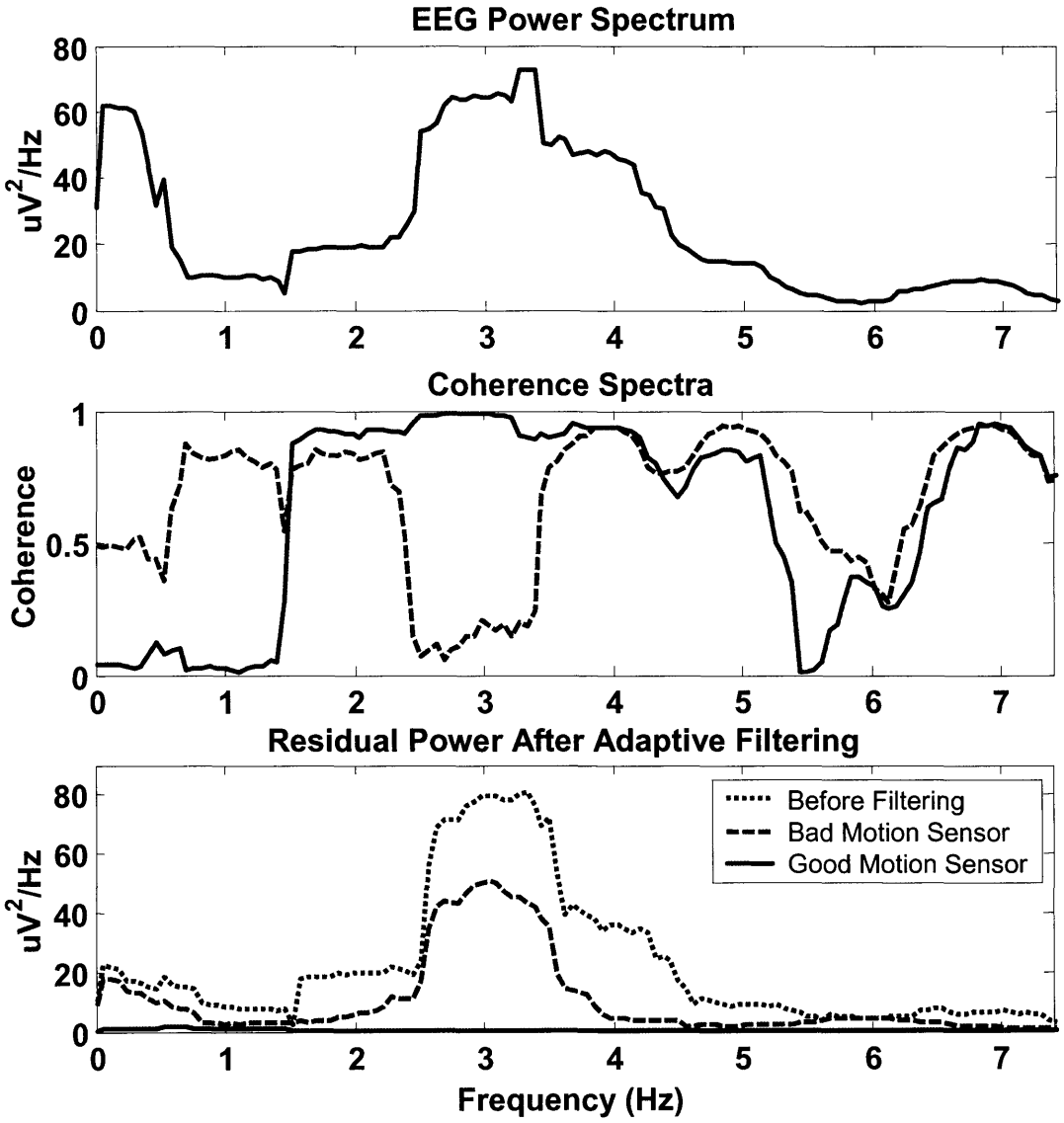

Figure 4.3. Coherence estimates of motion signal quality. A broken motion sensor was identified from repeated recordings where the sensor produced a periodic signal time-locked to the heart beat, but with an altered morphology and visibly reduced adaptive filter performance. Five minutes of resting state EEG data were recorded at 3T using this broken motion sensor on one side of the head, and a normally-functioning motion sensor on the other side of the head. The broken ("bad") motion sensor shows a noticeable band of low coherence centered at 3 Hz (middle, dotted line), a frequency that contains a substantial amount of ballistocardiogram noise power (top), as shown in the EEG power spectrum. In contrast, the "good" motion sensor has high coherence through the ballistocardiogram band (middle, solid line). Residual power after adaptive filtering with the "bad" motion sensor reveals a large residual peak centered at 3 Hz, while the good motion sensor had negligible residual power at this frequency (bottom).

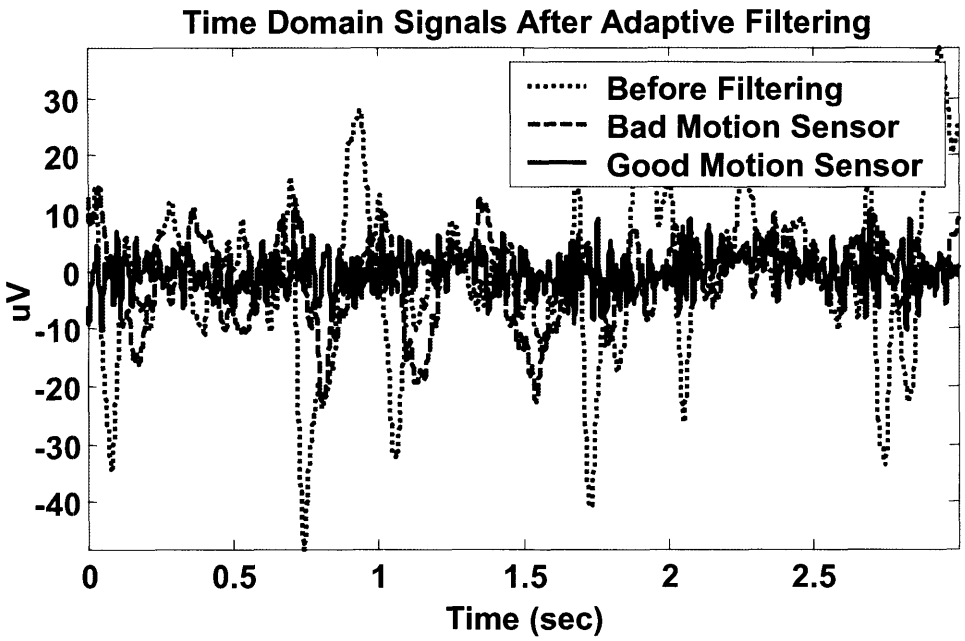

Figure 4.4. Coherence estimates predict adaptive filtering performance in time domain. Inspection of time-domain residuals show the large low-frequency residual noise present after filtering with the "bad" motion sensor (broad dotted line) compared with the "good" motion sensor (solid line).

4.3.2.b. VEPs Recorded During Interleaved EEG-fMRI Are Comparable to VEPs Recorded Outside The Magnet; Motion Sensors Produce No Visible MRI Artifacts

Figure 4.5 provides examples of visual evoked potentials taken during interleaved EEG/fMRI at 1.5 T (right side) and outside the MRI under normal conditions (left side). The first row presents the potentials of the five bipolar occipital channels used in this study (P3→O1, Pz→Oz, P4→O2, CP3→P3, CP4→P4). Equipotential plots of all the 32-channels are displayed in the second row, after transformation to a referential montage (denoted by black dots). Both the VEP waveforms and equipotential plots show good agreement between data collected inside and outside the magnet. The individual differences in peak onset and amplitude can be explained by the small differences in stimulus presentation (i.e., contrast, size, and luminosity) and brain state (i.e., state of

arousal, supine vs. sitting position). Note that the major positivity is concentrated over the right hemisphere, which is a common finding (Blumhardt et al., 1979). Our studies on human subjects indicate that no MR image artifacts are visible when using the proposed piezoelectric motion sensor (**Figure 4.6**).

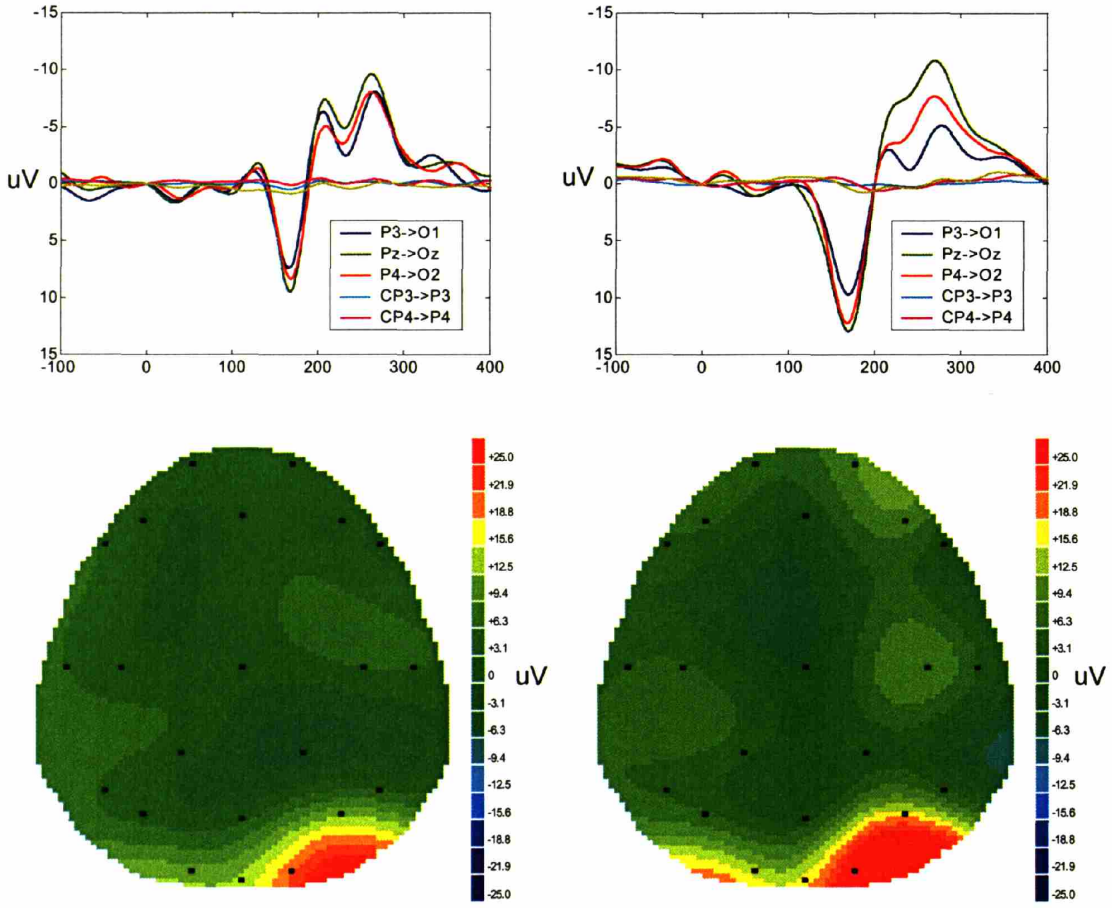

Figure 4.5. An example of visual evoked potentials (VEPs) collected outside the magnet (left column) and during an interleaved EEG/fMRI study (right column) from the same subject. On the top are the potentials of the five bipolar occipital channels used in this study. Below are the equipotential plots of all the 32-channels, after transforming them back into a referential montage. The map collected outside the magnet (bottom left) is shown at the 168 ms maximum peak (P4→O2) and the map collected during interleaved EEG/fMRI (bottom right, same colorbar) is shown at the 164 ms maximum peak (P4→O2). The similarity in both VEP waveforms and equipotential plots suggests that the adaptive filtering method does not alter the true underlying EEG signal.

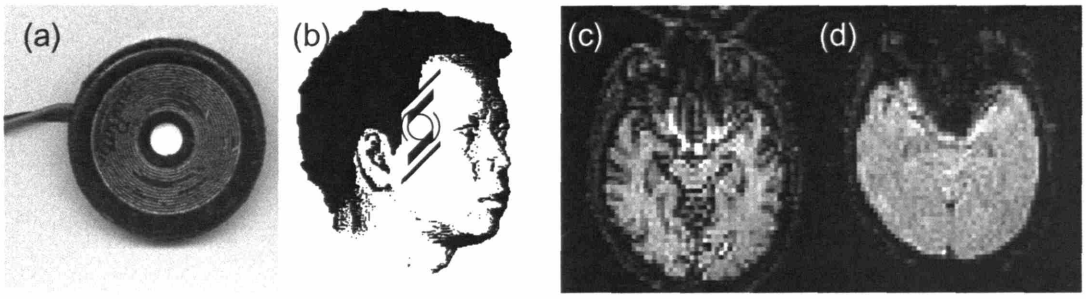

Figure 4.6. (a) The piezoelectric-transducer (muRata Inc., PKM11-4A0) with a silicon filling to reduce its sensitivity to acoustic noise. (b) The motion sensor was placed on the temporal artery. The motion sensor does not produce any visible artifact on the EPI T1-weighted (c) images and the T2*-weighted (d) images.

4.3.2.c. Adaptive Filtering Recovers Alpha Waves Recorded at 1.5 and 7 T

Raw EEG data collected outside the magnet during the eyes open/closed experiment are presented in **Figure 4.7**, for bipolar channel Pz→Oz. **Figure 4.8** shows identical recordings from inside the 1.5T static field: during the initial 5 seconds the subject was instructed to have open eyes and during the last 5 seconds the eyes were closed. The adaptive filtered EEG traces (middle) unlike the raw traces (top) clearly show the presence of alpha waves (8-13 Hz). The bottom trace shows the motion sensor signal. In time-frequency domain the presence of alpha activity is even easier to detect in both the spectrograms of the filtered and non-filtered data (**Figure 4.9**). As in the simulation studies, adaptive filtering is able to improve signal to noise in band (top). **Figure 4.10** shows alpha waves in time domain from channel P4→P8 from a recording at 7 T, before (top) and after (bottom) adaptive filtering. **Figure 4.11** shows an EEG channel (T8→P8) with alpha waves at 7 T where ballistocardiogram noise substantially overlaps the alpha band in time-frequency, obscuring the eyes open, eyes closed pattern. Adaptive filtering recovers the eyes open, eyes closed pattern, producing a 60% increase in SNR in-band for the indicated time intervals.

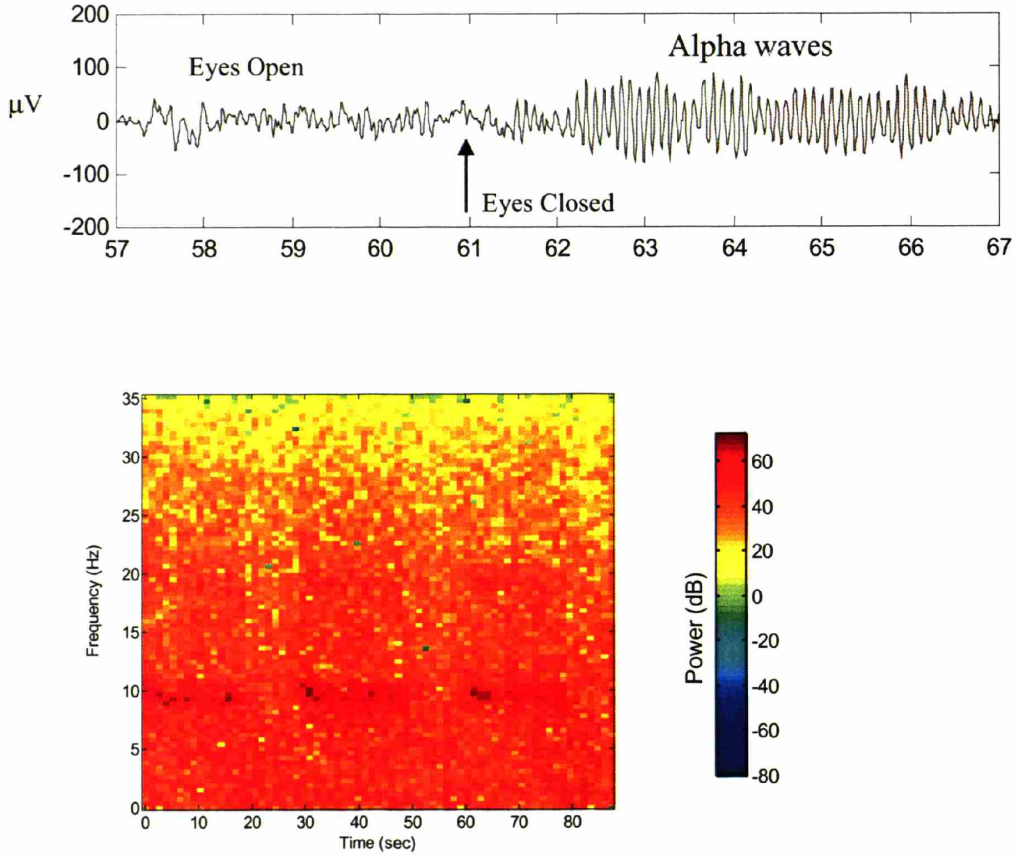

Figure 4.7. (Top) Fragment of raw EEG data collected outside the magnet during an eyes open/closed experiment. (Bottom) Spectrogram of the entire experiment collected using the bipolar channel Pz→Oz. Alpha activity is observed during three 20 sec periods of the eyes closed.

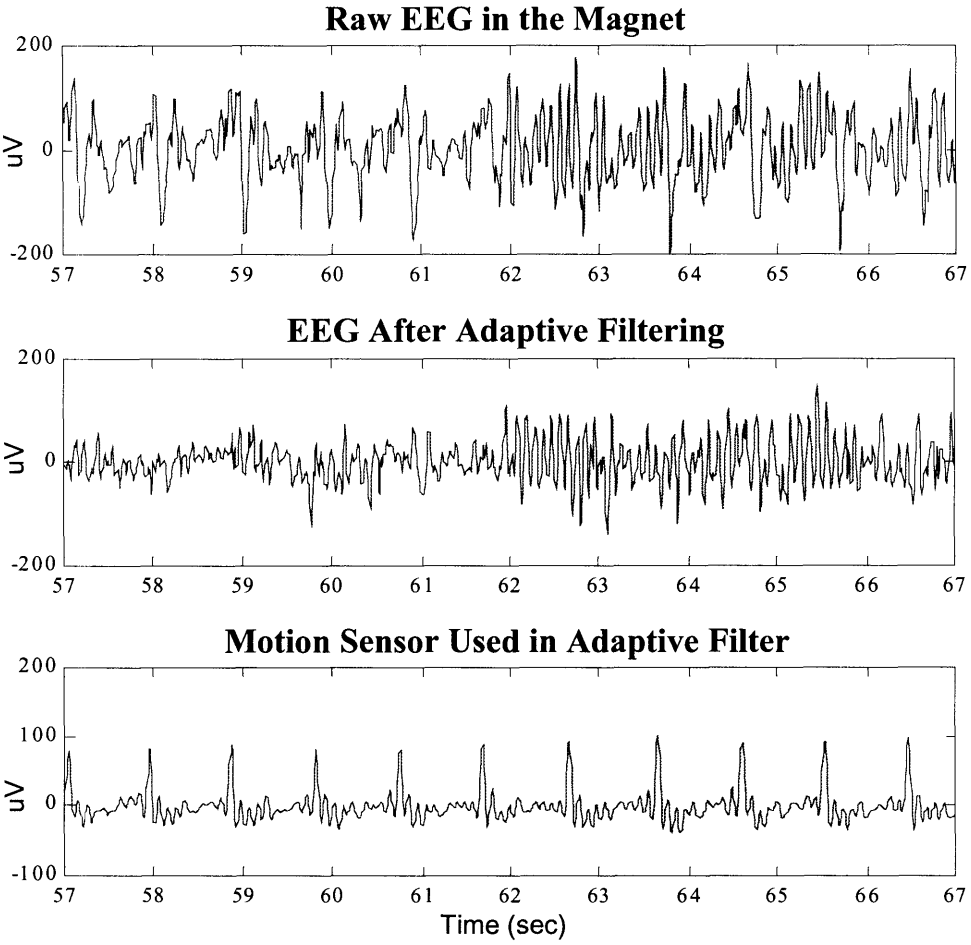

Figure 4.8. (Top) Raw EEG data collected inside the 1.5T static field during an eyes open/closed experiment from bipolar channel Pz→Oz. (Middle) Filtered EEG data that clearly shows the alpha waves present during the eyes closed condition. (Bottom) Output of the piezoelectric motion sensor shows ballistocardiogram activity.

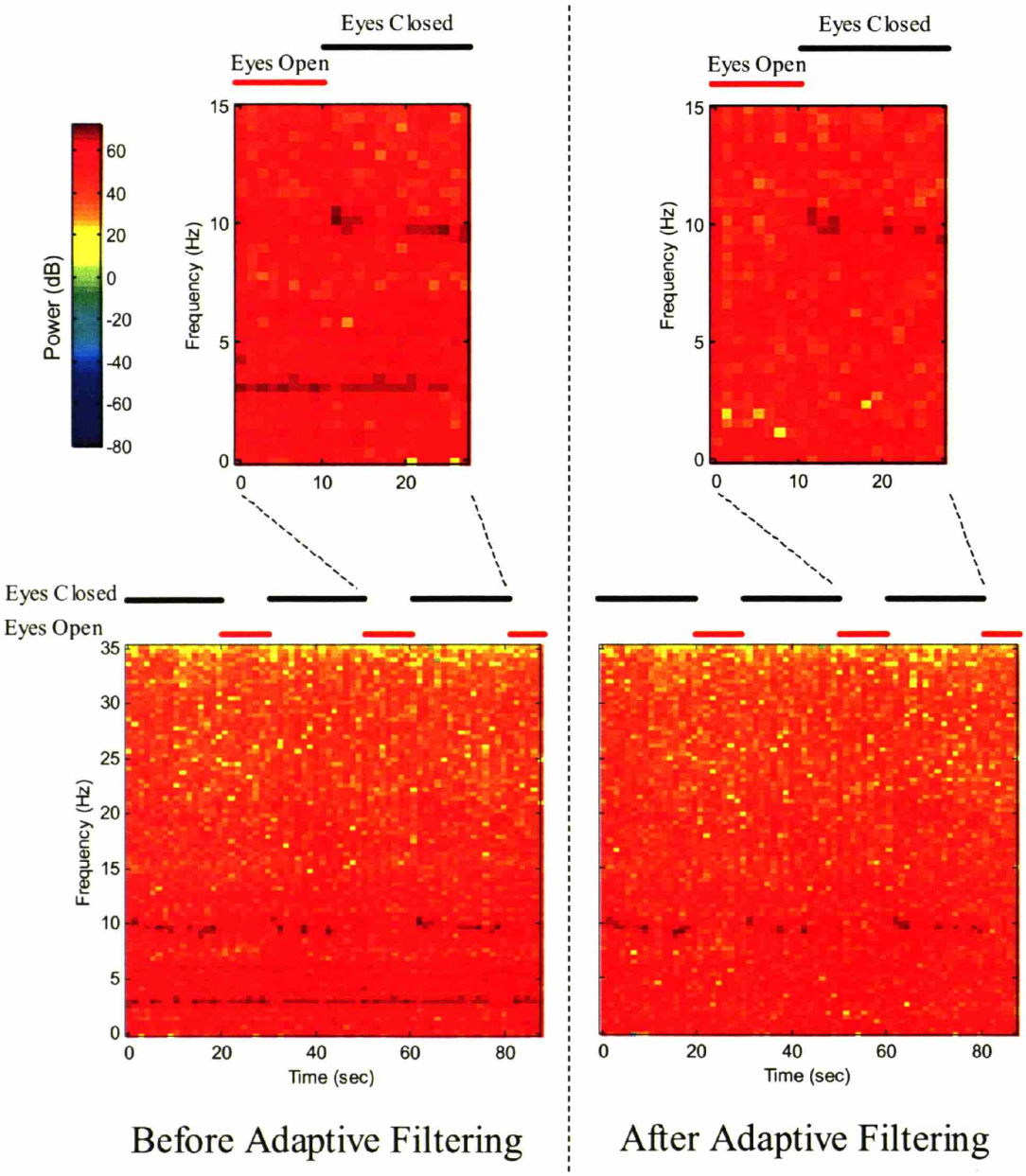

Figure 4.9. Spectrogram of the EEG with (right) and without (left) adaptive filtering during an eyes open/closed experiment from bipolar channel Pz→Oz recorded inside a 1.5T static field. The average amount of noise power removed by the adaptive filter in any 30 sec (i.e., a full cycle of eyes open/closed) window was approximately 70 dB. Note that the noise cancellation algorithm is cabable of improving the SNR of the signal both inside and outside the alpha band (8-13 Hz).

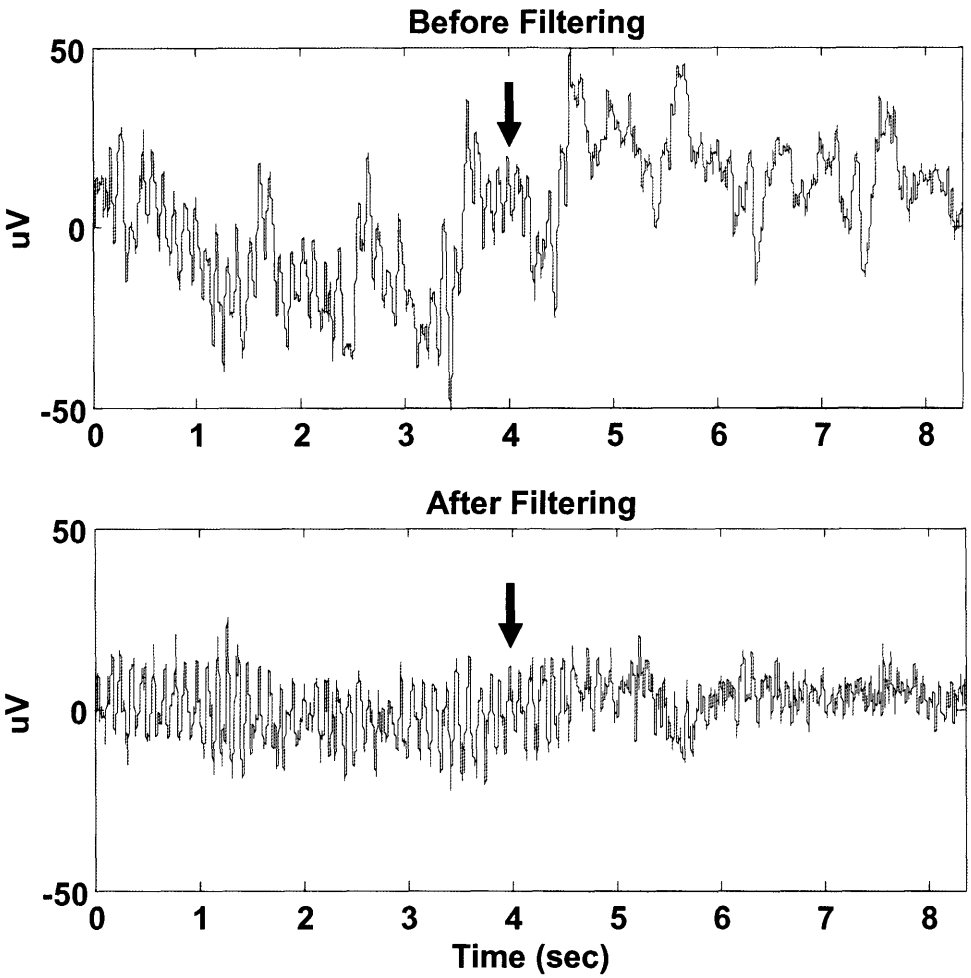

Figure 4.10. Alpha wave recordings at 7T in time domain from channel P4→P8 before (top) and after (bottom) adaptive filtering. After filtering, the alpha waves present before the subject opens his or her eyes (arrow) are readily visible.

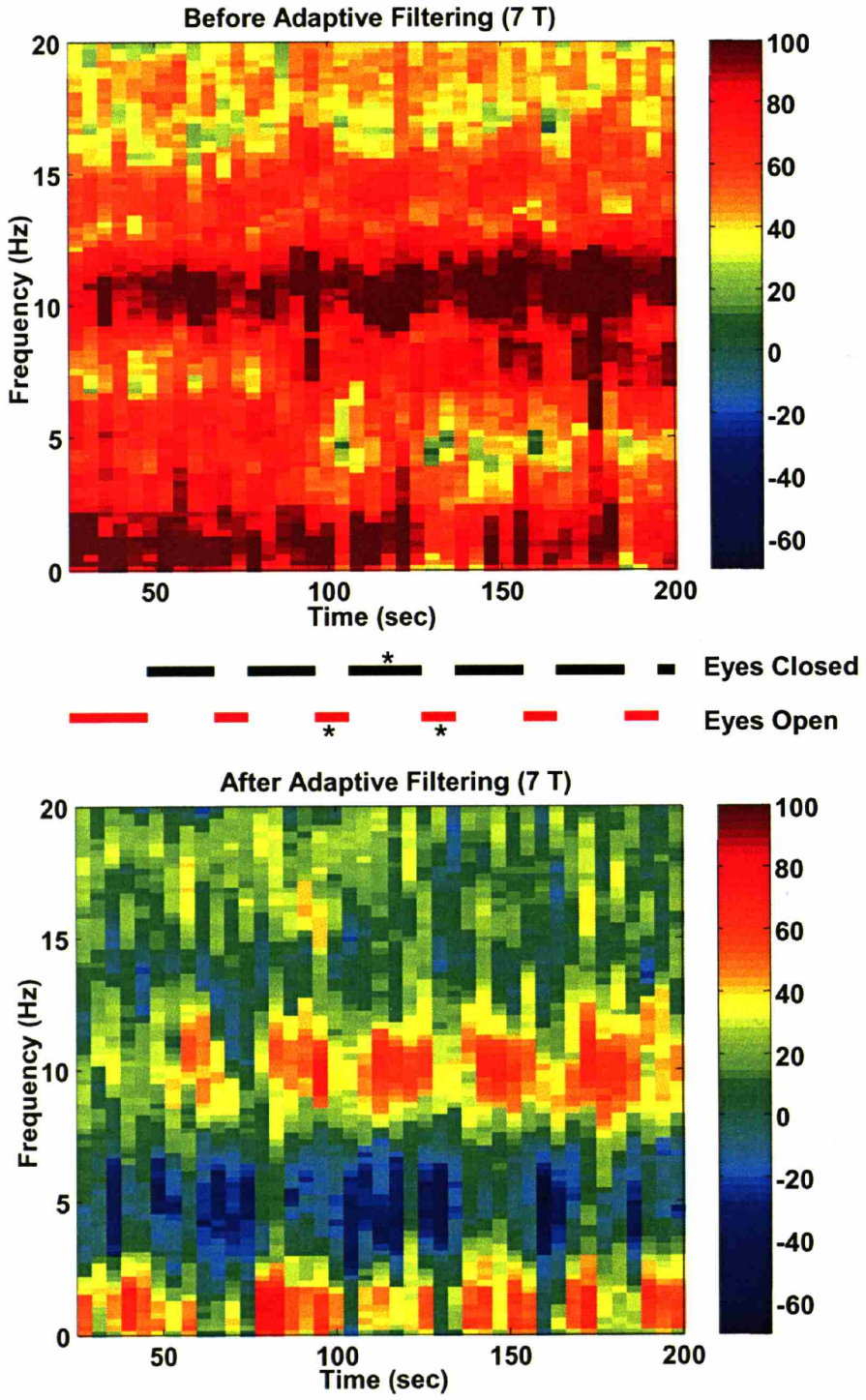

Figure 4.11. A time-frequency representation of alpha waves at 7T shows an EEG channel (T8→P8) where ballistocardiogram noise substantially overlaps the alpha band, obscuring the eyes open, eyes closed pattern. Adaptive filtering recovers the eyes open, eyes closed pattern, producing a 60% increase in SNR in-band for the indicated (*) time intervals.

4.4. Discussion

A number of methods have been proposed for ballistocardiogram artifact reduction. Template subtraction methods (Allen et al., 1998;Sijbersa et al., 2000) use ECG peak markers to identify temporal epochs containing heartbeats, and construct an average ballistocardiogram template waveform from the EEG that is subtracted from the EEG for each heartbeat interval. These methods are similar to the adaptive noise cancellation method proposed in this chapter in that they employ an external reference signal to inform the artifact removal process, but the reference signal and its processing are different. The SNR performance calculations presented in Section 4.3.1.a demonstrates that the adaptive filtering technique is able to provide much larger SNR gains than the subtraction method, by a margin of over 600% in some cases. Furthermore, in many cases, the subtraction method resulted in substantial reductions in SNR, by up to -64%. The poor performance of the subtraction method can be directly attributed to the difficulties associated with ECG acquisition and peak detection in the high field 3 T MRI environment. The template subtraction algorithms are highly sensitive to ECG peak mis-specifications: For instance, for an individual ECG epoch, if peak detection is translated by as little as +/- 50 msec (the half-period of a 10 Hz alpha wave), the ballistocardiogram noise in the alpha band can actually increase for that epoch. At higher field strengths such as 3, 4 or 7 T, ECG recordings become increasingly difficult to record cleanly. Chest motion from respiration, chest vibration from cardiac pulsation, and Hall-effect flow artifacts, most likely from aortic flow, produce signal artifacts that distort and add noise to the ECG signal. Peak detection on noisy or

distorted ECG signals is prone to failure, since the usual ECG morphology recognized by peak detection algorithms is no longer present. Furthermore, peak detection algorithms require estimates of signal slopes or derivatives, which are inherently sensitive to noise. The adaptive noise cancellation algorithm presented here suffers from none of these shortcomings, and has the added benefit that it is able to remove head movement artifacts in addition to ballistocardiogram.

The inherent physical and signal processing limitations associated with ECG acquisition and peak detection during MRI argue strongly in favor of motion-based adaptive filtering over ECG-based template subtraction for high field EEG-fMRI. In addition to these fundamental reasons, there are also practical reasons for choosing the motion-based adaptive filtering method presented here. During experimental studies, whether ECG or motion signals are being recorded, it is often difficult to ascertain whether the acquired reference signal is of adequate quality for artifact correction. The coherence estimation technique presented in Section 4.2.2.c provides a simple diagnostic tool for assessing motion sensor quality during experimental recordings from a short segment of baseline data. If the motion sensors have poor low-frequency coherence, the sensors can be re-positioned to provide better mechanical transduction, closer to the temporal arteries if necessary, or replaced if they are broken prior to functional scanning. No equivalent diagnostic tool exists for ECG-based methods, and even if such a tool did exist, improving ECG peak detection during the experimental recording session might not be possible, since ECG artifacts are tied directly to the fundamental physical constraints of the MRI static magnetic field. In post-processing, ECG peak detection failures would require time-consuming manual editing of ECG markers. In contrast, given a suitable

motion sensor, the adaptive filtering method requires no manual tuning, since its parameters can be estimated automatically from a short segment of data using the EM algorithm presented in Section 4.2.2.b and Appendix 4C.

Beyond template subtraction methods, other authors have proposed methods that attempt to remove ballistocardiogram artifacts directly from the EEG without the use of a reference signal of any kind, either by using a wavelet basis decomposition (Kim et al., 2004), or with an ICA decomposition (Srivastava et al., 2005)\. Both methods suffer from the problem that ballistocardiogram artifacts and the true underlying EEG signals occupy overlapping portions of time-frequency space, and are therefore difficult to separate without an external reference signal, particularly if the amplitudes of the signal and noise are similar (e.g., alpha waves, sleep induced delta waves, anesthesia induced burst-suppression patterns). The ICA-based methods have been developed for short epochs of data, primarily for ERP studies, and are not suitable for continuous recordings for sleep, epilepsy, or anesthesia. Given the low cost and simplicity of motion and ECG recordings, these reference-free methods should only be considered in cases where a motion or ECG reference are unavailable or of insufficient quality for noise cancellation.

4.5. Conclusions

In summary, we have developed a method for removing motion and ballistocardiogram artifacts using a novel motion sensor system combined with adaptive noise cancellation techniques. Adaptive filter parameters for each data set and channel are estimated using an EM algorithm that works on a short segment of EEG data, allowing for automatic filter parameter adjustment without manual tuning. We have also

developed a diagnostic technique based on coherence estimation for identifying motion signals to use with adaptive filtering, and to identify malfunctioning or badly placed motion sensors during EEG-fMRI experiments. We have demonstrated the efficacy of the method on recordings of alpha waves, VEPs, and head motion at 1.5, 3 and 7 T. Performance calculations from simulation studies show that the adaptive filter produces substantial improvements in SNR in-band, over 600% in some cases. In contrast, the subtraction method achieves much lower levels of SNR improvement (only 68% at maximum), and can actually reduce SNR in-band by a large percentage (up to -64% SNR).

Appendix 4A. A Random Walk Kalman Filter For Adaptive Noise Cancellation.

Given observations y_t, a reference signal u_t, and a random walk evolution for the state $\mathbf{x}_t$, we have

$$\begin{aligned} \mathbf{x}_t &= \mathbf{x}_{t-1} + \mathbf{w}_t \\ y_t &= \mathbf{u}_t^T \mathbf{x}_t + v_t \end{aligned}, \tag{4.12}$$

$$\mathbf{u}_t^T = [u_t \quad u_{t-1} \quad \ldots \quad u_{t-(M-1)}], \tag{4.13}$$

$$\begin{bmatrix} \mathbf{w}_t \\ v_t \end{bmatrix} \sim N\left(0, \begin{bmatrix} \sigma_w^2 \mathbf{I}_M & 0 \\ 0 & \sigma_v^2 \end{bmatrix}\right), \tag{4.14}$$

$$\begin{aligned} \mathbf{x}_0 &\sim N(\boldsymbol{\mu}_0, \boldsymbol{\Sigma}_0) \\ \boldsymbol{\mu}_0 &= 0 \\ \boldsymbol{\Sigma}_0 &= \delta^{-1} \mathbf{I}_M \end{aligned}, \tag{4.15}$$

where M is the number of FIR components in the adaptive filter. The Kalman filter provides a recursive estimate of both the state $\hat{\mathbf{x}}_{t|t}$ and the associated error covariance matrix $\boldsymbol{\Sigma}_{t|t}$ (Anderson and Moore, 1979):

$$\begin{aligned} \hat{\mathbf{x}}_{t|k} &= E[\mathbf{x}_t \mid Y_k] \\ \boldsymbol{\Sigma}_{t|k} &= E[(\mathbf{x}_t - \hat{\mathbf{x}}_{t|k})(\mathbf{x}_t - \hat{\mathbf{x}}_{t|k})^T \mid Y_k]. \\ Y_k &= \{y_{1,\ldots,} y_k\} \end{aligned} \tag{4.16}$$

It can be divided into three steps: Initialization, prediction (time update), and filtering (measurement update):

Initialization:

$$\begin{aligned} \hat{\mathbf{x}}_{0|0} &= \overline{\mathbf{x}}_0 = 0 \\ \boldsymbol{\Sigma}_{0|0} &= \boldsymbol{\Sigma}_0 = \delta^{-1}\mathbf{I}_M \end{aligned} \tag{4.17}$$

Prediction (Time Update):

$$\begin{aligned} \hat{\mathbf{x}}_{t|t-1} &= \hat{\mathbf{x}}_{t-1|t-1} \\ \boldsymbol{\Sigma}_{t|t-1} &= \boldsymbol{\Sigma}_{t-1|t-1} + \sigma_w^2 \mathbf{I}_M \end{aligned} \tag{4.18}$$

Filtering (Measurement Update):

$$\begin{aligned} \hat{\mathbf{x}}_{t|t} &= \hat{\mathbf{x}}_{t|t-1} + \mathbf{K}_t(y_t - \mathbf{u}_t^T \hat{\mathbf{x}}_{t|t-1}) \\ \boldsymbol{\Sigma}_{t|t} &= (\mathbf{I} - \mathbf{K}_t \mathbf{u}_t^T)\boldsymbol{\Sigma}_{t|t-1} \\ \mathbf{K}_t &= \boldsymbol{\Sigma}_{t|t-1}\mathbf{u}_t^T(\mathbf{u}_t^T \boldsymbol{\Sigma}_{t|t-1}\mathbf{u}_t + \sigma_v^2)^{-1} \end{aligned} \tag{4.19}$$

The prediction estimates $\hat{\mathbf{x}}_{t|t-1}$ are used to achieve adaptive noise cancellation using the relations

$$\hat{n}_t = \mathbf{u}_t^T \hat{\mathbf{x}}_{t|t-1}, \tag{4.20}$$

$$\hat{v}_t = y_t - \hat{n}_t. \tag{4.21}$$

where $\hat{n}_t$ is the estimate of the ballistocardiogram artifact, and $\hat{v}_t$ is the estimate of the true underlying EEG signal.

For 1.5 T studies, EEG signals were downsampled by a factor of 10 to 100 Hz before filtering, and the EEG signal was delayed by 10 samples (~0.1 sec) to account for any potential mechanical transduction delay in the motion sensor. At 3 and 7 T, the EEG was downsampled by a factor of 8 to approximately 120 Hz, with a 16 sample delay (~0.134 sec). In both cases, M = 80 filter taps were used for filtering, with an initial covariance weighting of $\delta^{-1} = 1000$.

Appendix 4B. A Fixed Interval Smoother For A Random Walk State Process

The fixed-interval smoother is a recursive algorithm based on the Kalman filter that provides estimates of a signal $\mathbf{x}_t$ whose dynamics are described by a linear state-space system, based on observations $Y_N = \{y_{1,\ldots,}y_N\}$, with an associated error covariance matrix:

$$\begin{aligned} \hat{\mathbf{x}}_{t|N} &= E[\mathbf{x}_t \mid Y_N] \\ \boldsymbol{\Sigma}_{t|N} &= E[(\mathbf{x}_t - \hat{\mathbf{x}}_{t|N})(\mathbf{x}_t - \hat{\mathbf{x}}_{t|N})^T \mid Y_N] \end{aligned} \tag{4.22}$$

The smoothed estimates $\hat{\mathbf{x}}_{t|N}$ are acquired by first running the Kalman filter to obtain a sequence of filtered estimates $\{\hat{\mathbf{x}}_{t|t}\}$ for $1 \le t \le N$, and then using a recursive "backward" filter, initialized with $\hat{\mathbf{x}}_{N|N}$, to yield the smoothed estimates $\hat{\mathbf{x}}_{t|N}$. For the random walk state process described in Appendix 4A, the fixed interval smoothing equations are:

$$\begin{aligned}\hat{\mathbf{x}}_{t-1|N} &= \hat{\mathbf{x}}_{t-1|t-1} + \mathbf{A}_{t-1}(\hat{\mathbf{x}}_{t|N} - \hat{\mathbf{x}}_{t|t-1}) \\ \boldsymbol{\Sigma}_{t-1|N} &= \boldsymbol{\Sigma}_{t-1|t-1} + \mathbf{A}_{t-1}(\boldsymbol{\Sigma}_{t|N} - \boldsymbol{\Sigma}_{t|t-1})\mathbf{A}_{t-1}^T \\ \mathbf{A}_{t-1} &= \boldsymbol{\Sigma}_{t-1|t-1}\boldsymbol{\Sigma}_{t|t-1}^{-1}\end{aligned} \quad (4.23)$$

A derivation of the fixed-interval smoother can be found in (Ansley and Kohn, 1982).

The covariance smoothing algorithm provides a simple expression for computing the one-step conditional cross-covariance from the conditional covariance (De Jong and Mackinnon, 1988):

$$\boldsymbol{\Sigma}_{t-1,t|N} = E[(\mathbf{x}_{t-1} - \hat{\mathbf{x}}_{t-1|N})(\mathbf{x}_t - \hat{\mathbf{x}}_{t|N})^T \mid Y_N] = \mathbf{A}_{t-1}\boldsymbol{\Sigma}_{t|N} \quad (4.24)$$

Appendix 4C. An EM Algorithm For Kalman Adaptive Filter Parameter Estimation

Given the state-observer model described in Appendix 4A, the observed data are $Y_N = \{y_N, \ldots, y_1\}$, while the complete data consist of Y_N and $X_N = \{x_N, \ldots, x_0\}$. Define the parameter vector $\theta = [\sigma_w^2, \sigma_v^2]^T$. We construct the complete data likelihood $L_c(\theta; Y_N, X_N)$ as follows:

$$\begin{aligned}p_\theta(y_N, \ldots, y_1, \mathbf{x}_N, \ldots, \mathbf{x}_0) &= p_\theta(y_N, \ldots, y_1 \mid \mathbf{x}_N, \ldots, \mathbf{x}_0)p_\theta(\mathbf{x}_N, \ldots, \mathbf{x}_0) \\ &= \left(\prod_{t=1}^{N} p_\theta(y_t \mid \mathbf{x}_t)\right)\left(\prod_{t=1}^{N} p_\theta(\mathbf{x}_t \mid \mathbf{x}_{t-1})\right)p_\theta(\mathbf{x}_0)\end{aligned} \quad (4.25)$$

$$\begin{aligned}p_\theta(y_t \mid \mathbf{x}_t) &= \frac{1}{(2\pi\sigma_v^2)^{1/2}}\exp\left(-\frac{1}{2}\frac{(y_t - \mathbf{u}_t^T\mathbf{x}_t)^2}{\sigma_v^2}\right) \\ p_\theta(\mathbf{x}_t \mid \mathbf{x}_{t-1}) &= \frac{1}{(2\pi\sigma_w^2)^{M/2}}\exp\left(-\frac{1}{2}\frac{(\mathbf{x}_t - \mathbf{x}_{t-1})^T(\mathbf{x}_t - \mathbf{x}_{t-1})}{\sigma_w^2}\right) \\ p_\theta(\mathbf{x}_0) &= \frac{1}{(2\pi\sigma_w^2)^{M/2}}\exp\left(-\frac{1}{2}\frac{\mathbf{x}_0^T\mathbf{x}_0}{\sigma_w^2}\right)\end{aligned} \quad (4.26)$$

$$\log L_c(\theta; Y_N, X_N) = -\frac{M(N+1)}{2}\log(2\pi\sigma_w^2) - \frac{N}{2}\log(2\pi\sigma_v^2)$$
$$-\frac{1}{2\sigma_w^2}\sum_{t=1}^{N}(\mathbf{x}_t^T\mathbf{x}_t - 2\mathbf{x}_{t-1}^T\mathbf{x}_t + \mathbf{x}_{t-1}^T\mathbf{x}_{t-1}) - \frac{1}{2\sigma_v^2}\sum_{t=1}^{N}(y_t^2 - 2y_t\mathbf{u}_t^T\mathbf{x}_t + \mathbf{u}_t^T\mathbf{x}_t\mathbf{x}_t^T\mathbf{u}_t) - \frac{1}{2\sigma_w^2}\mathbf{x}_0^T\mathbf{x}_0 \quad (4.27)$$

We next derive the EM algorithm for this complete data likelihood.

E-step:

$$\begin{aligned}
&Q(\theta;\theta_k) = E_{\theta_k}[\log L_c(\theta; Y_N, X_N) \mid Y_N] \\
&= -\frac{M(N+1)}{2}\log(2\pi\sigma_w^2) - \frac{N}{2}\log(2\pi\sigma_v^2) \\
&-\frac{1}{2\sigma_w^2}\sum_{t=1}^{N}\left(tr\left\{E_{\theta_k}[\mathbf{x}_t\mathbf{x}_t^T \mid Y_N]\right\} - 2\left(tr\left\{E_{\theta_k}[\mathbf{x}_{t-1}\mathbf{x}_t^T \mid Y_N]\right\}\right) + \left(tr\left\{E_{\theta_k}[\mathbf{x}_{t-1}\mathbf{x}_{t-1}^T \mid Y_N]\right\}\right)\right) \quad (4.28) \\
&-\frac{1}{2\sigma_v^2}\sum_{t=1}^{N}(y_t^2 - 2y_t\mathbf{u}_t^T E_{\theta_k}[\mathbf{x}_t \mid Y_N] + \mathbf{u}_t^T E_{\theta_k}[\mathbf{x}_t\mathbf{x}_t^T \mid Y_N]\mathbf{u}_t) \\
&-\frac{1}{2\sigma_w^2}tr\left\{E_{\theta_k}[\mathbf{x}_0\mathbf{x}_0^T \mid Y_N]\right\}
\end{aligned}$$

M-step:

$$\begin{aligned}
&\frac{\partial Q(\theta;\theta_k)}{\partial\sigma_w^2} = -\frac{M(N+1)}{2}\frac{1}{\sigma_w^2} \\
&-\frac{1}{2(\sigma_w^2)^2}\sum_{t=1}^{N}\left(tr\left\{E_{\theta_k}[\mathbf{x}_t\mathbf{x}_t^T \mid Y_N]\right\} - 2\left(tr\left\{E_{\theta_k}[\mathbf{x}_{t-1}\mathbf{x}_t^T \mid Y_N]\right\}\right) + \left(tr\left\{E_{\theta_k}[\mathbf{x}_{t-1}\mathbf{x}_{t-1}^T \mid Y_N]\right\}\right)\right) \quad (4.29) \\
&-\frac{1}{2(\sigma_w^2)^2}tr\left\{E_{\theta_k}[\mathbf{x}_0\mathbf{x}_0^T \mid Y_N]\right\} = 0
\end{aligned}$$

$$\begin{aligned}
\sigma_{w,k+1}^2 &= \frac{1}{M(N+1)}\sum_{t=1}^{N}\left(tr\left\{E_{\theta_k}[\mathbf{x}_t\mathbf{x}_t^T \mid Y_N]\right\} - 2\left(tr\left\{E_{\theta_k}[\mathbf{x}_{t-1}\mathbf{x}_t^T \mid Y_N]\right\}\right) + \left(tr\left\{E_{\theta_k}[\mathbf{x}_{t-1}\mathbf{x}_{t-1}^T \mid Y_N]\right\}\right)\right) \\
&+\frac{1}{M(N+1)}tr\left\{E_{\theta_k}[\mathbf{x}_0\mathbf{x}_0^T \mid Y_N]\right\}
\end{aligned} \quad (4.30)$$

$$\frac{\partial Q(\theta;\theta_k)}{\partial\sigma_v^2} = -\frac{N}{2}\frac{1}{\sigma_v^2} - \frac{1}{2(\sigma_v^2)^2}\sum_{t=1}^{N}(y_t^2 - 2y_t\mathbf{u}_t^T E_{\theta_k}[\mathbf{x}_t \mid Y_N] + \mathbf{u}_t^T E_{\theta_k}[\mathbf{x}_t\mathbf{x}_t^T \mid Y_N]\mathbf{u}_t) = 0 \quad (4.31)$$

$$\sigma_{v,k+1}^2 = \frac{1}{N}\sum_{t=1}^{N}(y_t^2 - 2y_t\mathbf{u}_t^T E_{\theta_k}[\mathbf{x}_t \mid Y_N] + \mathbf{u}_t^T E_{\theta_k}[\mathbf{x}_t\mathbf{x}_t^T \mid Y_N]\mathbf{u}_t) \tag{4.32}$$

The conditional expectations can be computed using the fixed-interval smoother and its associated covariance algorithm using the following relations:

$$\begin{aligned}\boldsymbol{\Sigma}_{t|N,\theta_k} &= E_{\theta_k}[(\mathbf{x}_t - \hat{\mathbf{x}}_{t|N})(\mathbf{x}_t - \hat{\mathbf{x}}_{t|N})^T \mid Y_N] \\ &= E_{\theta_k}[\mathbf{x}_t\mathbf{x}_t^T \mid Y_N] - E_{\theta_k}[\mathbf{x}_t \mid Y_N]E_{\theta_k}[\mathbf{x}_t^T \mid Y_N], \qquad (4.33) \\ E_{\theta_k}[\mathbf{x}_t\mathbf{x}_t^T \mid Y_N] &= \boldsymbol{\Sigma}_{t|N,\theta_k} + E_{\theta_k}[\mathbf{x}_t \mid Y_N]E_{\theta_k}[\mathbf{x}_t^T \mid Y_N]\end{aligned}$$

$$\begin{aligned}\boldsymbol{\Sigma}_{t-1,t|N,\theta_k} &= E_{\theta_k}[(\mathbf{x}_{t-1} - \hat{\mathbf{x}}_{t-1|N})(\mathbf{x}_t - \hat{\mathbf{x}}_{t|N})^T \mid Y_N] \\ &= E_{\theta_k}[\mathbf{x}_{t-1}\mathbf{x}_t^T \mid Y_N] - E_{\theta_k}[\mathbf{x}_{t-1} \mid Y_N]E_{\theta_k}[\mathbf{x}_t^T \mid Y_N]. \qquad (4.34) \\ E_{\theta_k}[\mathbf{x}_{t-1}\mathbf{x}_t^T \mid Y_N] &= \boldsymbol{\Sigma}_{t-1,t|N,\theta_k} + E_{\theta_k}[\mathbf{x}_{t-1} \mid Y_N]E_{\theta_k}[\mathbf{x}_t^T \mid Y_N]\end{aligned}$$

Appendix 4D. Multitaper Coherence Estimation

Multitaper spectral estimation methods (Percival and Walden, 1993) were used to perform coherence estimation. Let $w_{m,t}$ represent the m-th order discrete prolate spheroidal sequence with length N and unity-normalized half-bandwidth W. An estimate of the coherence between two signals u_t and y_t can be calculated as

$$
\begin{aligned}
C_{uy}(\omega) &= \frac{\left|P_{uy}(\omega)\right|^2}{P_{uu}(\omega)P_{yy}(\omega)} \\
P_{uy}(\omega) &= \frac{1}{[2NW]-1}\sum_{m=0}^{[2NW]-2}\tilde{U}_m(\omega)\tilde{Y}_m^*(\omega) \\
P_{uu}(\omega) &= \frac{1}{[2NW]-1}\sum_{m=0}^{[2NW]-2}\left|\tilde{U}_m(\omega)\right|^2 \\
P_{yy}(\omega) &= \frac{1}{[2NW]-1}\sum_{m=0}^{[2NW]-2}\left|\tilde{Y}_m(\omega)\right|^2 \\
\tilde{U}_m(\omega) &= \sum_{t=0}^{N-1}\tilde{u}_{m,t}e^{-j\omega t} \\
\tilde{Y}_m(\omega) &= \sum_{t=0}^{N-1}\tilde{y}_{m,t}e^{-j\omega t} \\
\tilde{u}_{m,t} &= w_{m,t}u_t \\
\tilde{y}_{m,t} &= w_{m,t}y_{m,t}
\end{aligned}
\tag{4.35}
$$

4.6. References

1. Allen PJ, Polizzi G, Krakow K, Fish DR, Lemieux L (1998) Identification of EEG events in the MR scanner: the problem of pulse artifact and a method for its subtraction. Neuroimage 8: 229-239.

2. Anderson BDO, Moore JB (1979) Optimal Filtering. Englewood Cliffs, New Jersey: Prentice-Hall.

3. Ansley CF, Kohn R (1982) A geometrical derivation of the fixed interval smoothing algorithm. Biometrika 69: 486-487.

4. Blumhardt L, Barrett G, Halliday A (1979) Hemisphere contribution to the composition of the pattern-evoked waveform. Exp Brain Res 36: 53-69.

5. De Jong P, Mackinnon MJ (1988) Covariances for smoothed estimates in state space models. Biometrika 75: 601-602.

6. Goldman RI, Stern JM, Engel J, Jr., Cohen MS (2002) Simultaneous EEG and fMRI of the alpha rhythm. Neuroreport 13: 2487-2492.

7. Haykin S (2002) Adaptive Filter Theory. Upper Saddle River, NJ: Prentice Hall.

8. Huang-Hellinger FR, Breiter HC, McCormack G, Cohen MS, Kwong KK, Sutton JP, Savoy RL, Weisskoff RM, Davis TL, Baker JR, Belliveau JW, Rosen BR (1995) Simultaneous functional magnetic resonance imaging and electrophysiological recording. Hum Brain Mapp 3: 13-23.

9. Kim KH, Yoon HW, Park HW (2004) Improved ballistocardiac artifact removal from the electroencephalogram recorded in fMRI. J Neurosci Methods 135: 193-203.

10. Laufs H, Kleinschmidt A, Beyerle A, Eger E, Salek-Haddadi A, Preibisch C, Krakow K (2003a) EEG-correlated fMRI of human alpha activity. Neuroimage 19: 1463-1476.

11. Laufs H, Krakow K, Sterzer P, Eger E, Beyerle A, Salek-Haddadi A, Kleinschmidt A (2003b) Electroencephalographic signatures of attentional and cognitive default modes in spontaneous brain activity fluctuations at rest. Proc Natl Acad Sci U S A 100: 11053-11058.

12. Lemieux L, Salek-Haddadi A, Josephs O, Allen P, Toms N, Scott C, Krakow K, Turner R, Fish DR (2001) Event-related fMRI with simultaneous and continuous EEG: description of the method and initial case report. Neuroimage 14: 780-787.

13. McLachlan GJ, Krishnan T (1997) The EM algorithms and extensions. New York: John Wiley.

14. Nunez PL (1995) New York: Oxford University Press.

15. Percival DB, Walden AT (1993) Spectral analysis for physical applications. New York: Cambridge University Press.

16. Portas CM, Krakow K, Allen P, Josephs O, Armony JL, Frith CD (2000) Auditory processing across the sleep-wake cycle: simultaneous EEG and fMRI monitoring in humans. Neuron 28: 991-999.

17. Priestley MB (1982) Spectral analysis and time series. New York: Academic Press.

18. Rampil IJ (1998) A primer for EEG signal processing in anesthesia. Anesthesiology 89: 980-1002.

19. Schomer DL, Bonmassar G, Lazeyras F, Seeck M, Blum A, Anami K, Schwartz D, Belliveau JW, Ives J (2000) EEG-Linked functional magnetic resonance imaging in epilepsy and cognitive neurophysiology. J Clin Neurophysiol 17: 43-58.

20. Sijbersa J, Van Audekerke J, Verhoye M, Van der LA, Van Dyck D (2000) Reduction of ECG and gradient related artifacts in simultaneously recorded human EEG/MRI data. Magn Reson Imaging 18: 881-886.

21. Srivastava G, Crottaz-Herbette S, Lau KM, Glover GH, Menon V (2005) ICA-based procedures for removing ballistocardiogram artifacts from EEG data acquired in the MRI scanner. Neuroimage 24: 50-60.

22. Vasios, C. E., Angelone, L. M., Purdon, P., Belliveau, J. W., and Bonmassar, G. EEG measurements at 7T Tesla using the ink cap. 13th ISMRM (submitted) . 2005.

Chapter 5
Simultaneous EEG-fMRI of the 40-Hz Auditory Steady State Response at 3 and 7 Tesla

5.1. Introduction

The 40-Hz auditory steady-state response (ASSR) is an auditory evoked potential related to sleep, consciousness, and anesthesia. The 40-Hz ASSR is reduced or eliminated by decreases in level of arousal (Picton et al., 2003), sleep (Cohen et al., 1991;Suzuki et al., 1994;Linden et al., 1985), and sedation or loss of consciousness under anesthesia (Plourde, 1996), and is also predictive of post-trauma coma survival (Serafini et al., 1994). The 40-Hz ASSR is not influenced by selective attention (Linden et al., 1987;Tiitinen et al., 1993) nor alerting nor orienting responses (Rohrbaugh et al., 1990), suggesting that the ASSR is highly specific for changes in level of arousal or consciousness. Understanding the mechanisms for generation and loss of the 40-Hz ASSR could provide insights into the mechanisms for sleep, anesthesia, and consciousness.

A common observation during functional imaging studies is that study subjects exhibit varying levels of arousal during the course of a study. Recently, studies by Goldman, et al. (Goldman et al., 2002), and Laufs, et al. (Laufs et al., 2003b;Laufs et al., 2003a) have recorded alpha waves in awake, resting study-subjects during simultaneous fMRI. Temporal changes in the level of alpha power during these studies reflected fluctuations in the study subjects' level of arousal or drowsiness (Goldman et al., 2002), and were correlated with fMRI signals across widespread cortical networks thought to support alpha activity (Goldman et al., 2002) as well as default-mode neural activity (Laufs et al., 2003b). In this chapter, we present a simultaneous EEG-fMRI study where we observe spontaneous fluctuations in 40-Hz ASSR amplitude, and we relate these fluctuations to fMRI signal changes. If the observed fluctuations in 40-Hz ASSR reflect spontaneous endogenous fluctuations in state of arousal or consciousness, these studies may provide insight into the mechanisms for generation and consciousness-related modulation of the 40-Hz ASSR.

5.2. Materials and Methods

5.2.1. Study Subjects

A total of 19 normal healthy volunteers were studied. All study subjects provided informed consent in accordance with Massachusetts General Hospital policies (MGH IRB number 2002-P-001703). Eleven subjects were studied at 3T, with 3 studies excluded due to excessive motion artifacts in either EEG or MRI, while 8 subjects were studied at 7T.

5.2.2. Stimulus Presentation

Subjects were presented with either 30-second trains of 1-msec clicks at 40-Hz (3T only), or with 30-second trains of 12.5 millisecond noise bursts at 40-Hz (both 3T and 7T), in a 30-second stimulus ON, 30-second stimulus OFF pattern over a 15-minute run. Subjects for all 3T studies were instructed to lie quietly in the magnet while listening to the click or noise bursts with eyes open. For studies at 7T, study subjects were instructed to perform this same listening task while awake with eyes closed in approximately half of all trials at 7T, with eyes open in the remaining trials. For two noise burst studies at 3T, subjects were asked to identify a tone presented 10-seconds after the end of each 30 second noise burst. Presented tones were either 220 or 440 Hz, and subjects were asked to press a button in response to either tone. Due to the short duration of the tone, fMRI responses to the tone were not modeled or analyzed specifically. Furthermore, the brief tone duration and long (20 second) duration between the end of the tone and beginning of the next noise burst suggests that the tone is unlikely to influence noise burst responses (Rohrbaugh et al., 1990). Consequently, these two tone-identification studies were analyzed in a manner identical to the other studies. Stimuli were delivered using a laptop running Presentation 0.76 (Neurobehavioral Systems) with an Echo Indigo 24-bit PCMCIA audio card (Echo Digital Audio Corporation, Carpinteria, CA) and a custom-built electrically-shielded electrostatic headphone system with frequency response to 20 kHz and acoustic noise attenuation of >30 dB above 800 Hz.

5.2.3. EEG Acquisition

EEG recordings were performed at 3 and 7T using a 24-bit electrophysiological recording system featuring low noise and high dynamic range to prevent saturation during imaging, with a sampling rate of 957 Hz and a bandwidth of DC to 500 Hz. Data were displayed, recorded, and integrated with stimulus triggers using data acquisition software written in the LabView development environment (National Instruments). For 3T recordings, EEG electrodes were placed in adjacent bipolar pairs along a coronal plane (M2→T8, T8→C6, C6→C4, C4→Cz, Cz→C3, C3→C5, C5→T7, T7→M1) using Ag/Ag-Cl electrodes featuring a plastic housing (Gereonics, Inc., Solana Beach, CA) bonded to carbon fiber wires ("Fiber-Ohm" wires with 7 ohms/inch resistance; Marktek, Inc., Chesterfield, MO) with conductive epoxy. For 7T recordings, EEG was recorded using a 32-channel EEG cap featuring resistive EEG leads made from conductive inks printed onto flex-circuit material (Vasios et al., 2005), with a referential montage featuring a single reference on the left mastoid (M1). ASSRs were estimated from Cz→M1 for both 3T and 7T studies, using a linear combination of adjacent channels Cz→C3, C3→C5, C5→T7, and T7→M1 for 3T studies. .

To provide a reference signal for outlier rejection, a set of motion sensors were constructed from Murata PKM11-4A0 piezo-electric sensors (Murata Electronics North America, Inc., Smyrna, GA), replacing soldered metallic leads with carbon fiber leads (Marktek) bonded with conductive epoxy. To maximize mechanical coupling to the motion and cardiac pulsation of the head, sensors were placed in the vicinity of the temporal artery, held in position either by tape, surgical netting, or the EEG cap material, with light pressure applied using small cushions placed between the head coil and the

subject's head. Motion sensor signals were acquired using the same amplification and acquisition system as the EEG.

5.2.4. MRI acquisition

For 3T studies (Siemens, Erlangen, Germany), functional MRI were acquired using clustered-volume acquisition, with cardiac gating at 3T. Functional MRI acquisitions were arranged according to a "Long-TR" auditory fMRI design, with 15-slice volume acquisition in 1 second and spaced ~9 seconds apart (4 mm thick, 1 mm skip, 3.1 x 3.1 mm in-plane resolution, 64x64 matrix, coronal orientation, TE = 30, 90-degree flip angle), allowing hemodynamic responses elicited by acoustic scanner noise to subside before the next volume acquisition (Hall et al., 2000;Hall et al., 1999). Anatomical MRI at 3T were acquired using a T1-weighted MPRAGE sequence (1.3 mm thick, 1.3 x 1 mm in-plane resolution, TR/TE = 2530/3.24 msec, 7-degree flip angle). Functional MRI at 7T (Siemens, Erlangen, Germany) were arranged similarly, with volume acquisition in 1 second and a 9 second TR, but without cardiac gating (3.1 mm thick, 1.15 mm skip, 3.1 x 3.1 mm in-plane resolution, 64x64 matrix, coronal orientation, TE = 20, 90-degree flip angle). Anatomical MRI at 3T were acquired using a T1-weighted MPRAGE sequence (1.3 mm thick, 1.3 x 1 mm in-plane resolution, TR/TE = 2530/3.3 msec, 7-degree flip angle).

5.2.5. Estimation of 40-Hz ASSR

ASSR amplitudes were computed in the frequency domain using multi-taper spectral analysis {Percival & Walden 1993 329 /id} (bandwidth = 0.5 Hz, time-bandwidth product NW = 2.14) from 4-second EEG windows $x_n(t)$ centered 4-seconds

prior to each volume acquisition (**Figure 5.1**). This arrangement reflects the widely-observed phenomenon that the BOLD hemodynamic delay from stimulus onset is approximately 4-seconds (Hall et al., 2000;Hall et al., 1999). Equivalently, fMRI BOLD signals represent neural activity predominantly from events 4-seconds prior to an fMRI volume acquisition.

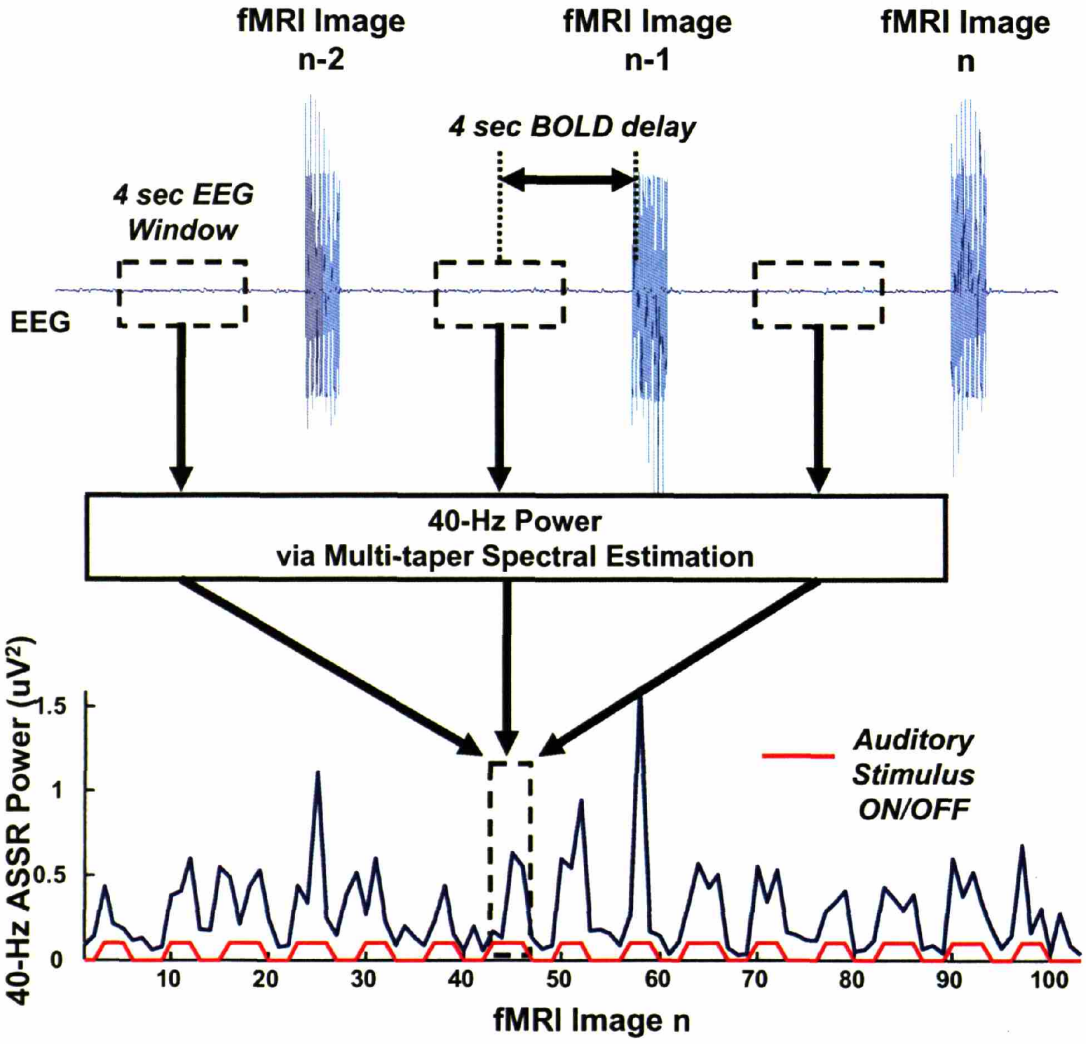

Figure 5.1. Estimation of 40-Hz ASSR power from segments of EEG between fMRI volume acquisitions.

For each window, power spectra were computed and averaged separately for stimulus ON and OFF conditions:

$$\begin{aligned} \bar{P}_{ON}(\omega) &= \frac{1}{N_{ON}} \sum_{StimulusON} P_n(\omega) \\ \bar{P}_{OFF}(\omega) &= \frac{1}{N_{OFF}} \sum_{StimulusOFF} P_n(\omega) \end{aligned}, \tag{5.1}$$

where $P_n(\omega)$ represents the power spectral estimate corresponding to the n-th EPI volume, and N_{ON} and N_{OFF} represent the number of EEG windows corresponding to stimulus ON and stimulus OFF conditions, respectively. In cases where EEG windows overlapped the transition from ON to OFF or vice-versa, the window was assigned to the condition with the majority of overlap with the window. To test for the presence of a 40-Hz response over the entire recording run, the power ratio $S(\omega)$ was computed:

$$S(\omega) = \frac{\bar{P}_{ON}(\omega)}{\bar{P}_{OFF}(\omega)}. \tag{5.2}$$

Under a null hypothesis where the EEG signal $x(t)$ is independent, identically-distributed $N(0,\sigma^2)$ Gaussian noise with no 40-Hz ASSR response, and with $P_n(\omega)$ estimated using a "simple" multitaper spectral estimate (Percival and Walden, 1993) with time-bandwidth product NW = 2, $S(\omega)$ is distributed as $F(2N_{ON}, 2N_{OFF})$. For the studies described here, $N_{ON} \approx 50$ and $N_{OFF} \approx 50$. Assuming a type I error of $\alpha = 0.01$, the null-hypothesis is rejected if $S(\omega)|_{\omega=40Hz} > 1.60$. Functional MRI analysis was not performed for datasets with non-significant 40-Hz ASSR power.

For each spectrum $P_n(\omega)$, the amplitude (square-root of power) at 40-Hz was computed to produce a 40-Hz amplitude time-series $a(n)$:

$$a(n) = \sqrt{P_n(\omega)}\,|_{\omega=40Hz}\,. \tag{5.3}$$

Power spectra for motion sensor signals $M_n(\omega)$ were computed from pre-EPI windows in a similar fashion. Power spectra for both the EEG and motion signals were plotted as time-frequency spectrograms and visually inspected for evidence of motion artifact: If, for a given epoch n, the EEG spectrum $P_n(\omega)$ contained a sudden increase in broad-band noise power compared to neighboring spectra (i.e., at times …, n-2, n-1, n+1, n+2,…, etc.) with a similar pattern in the motion spectrum $M_n(\omega)$, the given epoch *n* was marked as an outlier and censored from fMRI time series analysis (described below).

5.2.6. fMRI time series models

A natural choice for a time series model relating the 40-Hz ASSR to simultaneously recorded BOLD responses would be to use the 40-Hz amplitude time-series $a(n)$ as a regressor for each fMRI voxel time series $y(n)$:

$$y(n) = \mu + \sum_{i=1}^{q} \delta_i d_i(n) + \alpha a(n) + \varepsilon(n)\,, \tag{5.4}$$

where μ is the signal mean, the $d_i(n)$ are polynomial drift terms of order i with coefficients δ_i, α is the regression coefficient for $a(n)$, and $\varepsilon(n) \sim N(0,\sigma^2)$ is an independent, identically-distributed error term, and $q = 6$ is the maximum drift term order. We refer to this as the "ASSR model." Unfortunately, using $a(n)$ alone introduces a confound due to the ON-OFF pattern of the click or burst-train stimulus: The 40-Hz ASSR amplitude waveforms $a(n)$ are observed to contain spontaneous fluctuations in response amplitudes, but they also contain a mean response to the auditory stimulus whose time course is proportional to the stimulus indicator function $c(t_n)$,

which equals 1 when the stimulus is ON, and 0 when the stimulus is ON, at time points t_n corresponding to the n-th fMRI image. In the space of fMRI observations, this mean ASSR response is proportional to the standard block-paradigm response, which is modeled as a convolution * between the stimulus indicator $c(t)$ and the hemodynamic response $g(t)$:

$$\begin{aligned} b(t) &= g(t) * c(t) \\ g(t) &= (1-e^{-1/\tau})^2 (t+1) e^{-t/\tau};\ \tau = 1.5 \text{ seconds} \end{aligned} \tag{5.5}$$

To separately quantify the mean block-paradigm response and any fluctuation about that mean response, we decompose $a(n)$ into two parts: One representing the mean response $b(t_n)$ and one representing the fluctuation about that mean response $\tilde{a}(n)$:

$$a(n) = kb(t_n) + \tilde{a}(n), \tag{5.6}$$

We will refer to the term $\tilde{a}(n)$ as the "ASSR fluctuation," and we construct it as the orthogonal error after projecting $a(n)$ onto $b(t_n)$:

$$\begin{aligned} \tilde{a}(n) &= a(n) - kb(t_n) \\ k &= \sum_{n=0}^{N-1} a(n) b(t_n) / \sum_{n=0}^{N-1} b^2(t_n) \end{aligned}, \tag{5.7}$$

where N is the length of the fMRI time series. This decomposition is depicted in **Figure 5.2**. This yields the following time series model,

$$y(n) = \mu + \sum_{i=1}^{q} \delta_i d_i(n) + \tilde{\alpha}\tilde{a}(n) + \beta b(t_n) + \varepsilon(n), \tag{5.8}$$

which we refer to as the "ASSR fluctuation model," where $\tilde{\alpha}$ is the coefficient for the ASSR fluctuation, and β is the coefficient for the block-paradigm response. Because the ASSR fluctuation $\tilde{a}(n)$ is orthogonal to the block response $b(t_n)$, $\tilde{a}(n)$ represents signal components that are related to fluctuations in the ASSR amplitude, but *not* to the standard

block paradigm response $b(t_n)$. We introduce a final model, the "block response model," which is simply the standard block response:

$$y(n) = \mu + \sum_{i=1}^{q} \delta_i d_i(n) + \beta b(t_n) + \varepsilon(n). \tag{5.9}$$

We perform model estimation with ordinary least squares, which corresponds to the maximum-likelihood (ML) estimate under the stated Gaussian noise model. In cases where outliers are identified in the ASSR analysis from section 5.2.5, we omit those time-points from the model fitting procedure.

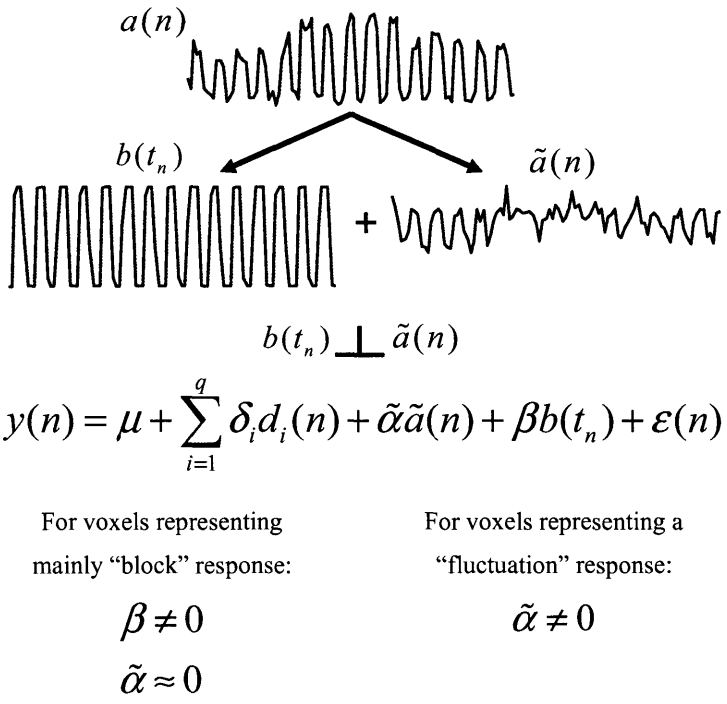

Figure 5.2. The ASSR fluctuation time series model. The 40-Hz ASSR amplitude time series $a(n)$ is decomposed into two components: One due to a time-invariant response to the fMRI block paradigm ($b(t_n)$), and another due to spontaneous endogenous fluctuations in the 40-Hz amplitude ($\tilde{a}(n)$). The coefficient $\tilde{\alpha}$ for the "fluctuation" term $\tilde{a}(n)$ represents the degree to which the fluctuations in 40-Hz ASSR are represented within a given fMRI voxel.

5.2.7. Model comparison

To compare the performance of these models, we compute Akaike's Information Criterion (AIC) voxel-wise for each model (Kitagawa and Gersh, 1996). For the independent, identically-distributed Gaussian noise model represented above, AIC is defined as:

$$AIC = N \log \hat{\sigma}^2 + 2p, \tag{5.10}$$

where p is the model order and $\hat{\sigma}^2$ is the ML estimate of the variance.

5.2.8. Data analysis schema

For each data set, the following schema was followed to analyze the data:

1. The power ratio $S(\omega)$ was computed, and if significant, fMRI analysis was performed.
2. ASSR amplitude time series $a(n)$ and ASSR fluctuation time series $\tilde{a}(n)$ were computed.
3. Model fit and AIC were computed for each fMRI time series model:
    a. Block response model
    b. ASSR model
    c. ASSR fluctuation model
4. AIC values for the ASSR and ASSR fluctuation models were compared voxel-wise against the AIC for the block response model:

$$\begin{aligned} \delta AIC(ASSR) &= AIC(ASSR) - AIC(block) \\ \delta AIC(FLUC) &= AIC(FLUC) - AIC(block) \end{aligned} \tag{5.11}$$

5. Activation maps were thresholded using F-values with P<0.001. Voxels that exceeded this threshold for the ASSR and ASSR fluctuation models with $\delta AIC < 0$ were considered to show a significant correlation with the ASSR or ASSR fluctuation, respectively.

5.3. Results

For the 16 subjects studied, a total of 31 15-minute EEG-fMRI runs were recorded. Out of those 31 runs, 19 resulted in a significant 40-Hz ASSR response as determined by the power ratio hypothesis test described in Section 5.2.5. **Table 5.1** shows the power ratio results for all subjects. **Figure 5.3** shows power ratio spectra $S(\omega)$ for three representative data sets for clicks and noise bursts at 3T and noise bursts at 7T.

Analysis of fMRI data revealed activity throughout the auditory system, including superior temporal gyrus (STG), Heschl's gyrus (HG), inferior colliculus (IC), and cochlear nucleus (CN), for each of the three models considered (block response, ASSR, and ASSR fluctuation). AIC values for ASSR and ASSR fluctuation models were lower than those for the block response model in these areas as well across multiple subjects. **Figures 5.4** through **5.8** show activation maps and time series fits from selected data sets at both 3 and 7 Tesla. The influence of modulatory effects are evident in the model fits shown in **Figure 5.5**, where there is a clear correspondence between increasing amplitude in the middle of the ASSR-based time series and the fMRI time series. **Figure 5.8** shows a similar correspondence, where both ASSR and fMRI time series show a decreasing amplitude with time.

Subject Number	MRI Field Strength	Stimulus	40-Hz ASSR Power Ratio	Eyes Open or Closed
3C1	3T	Click-train, 30sec	1.7492*	Open
	3T	Click-train, 30sec	2.0094*	Open
3C2	3T	Click-train, 30sec	2.3149*	Open
	3T	Click-train, 30sec	1.1405	Open
	3T	Click-train, 30sec, tone task	1.3643	Open
3C3	3T	Click-train, 30sec	2.7524*	Open
	3T	Click-train, 30sec	1.8563*	Open
3C4	3T	Click-train, 30sec	2.0692*	Open
	3T	Click-train, 30sec	2.0350*	Open
3B1	3T	Burst-train, 30sec	15.2033*	Open
	3T	Burst-train, 30sec	5.0299*	Open
3B2	3T	Burst-train, 30sec	1.0458	Open
	3T	Burst-train, 30sec	1.46	Open
3B3	3T	Burst-train, 30sec, tone task	2.4032*	Open
3B4	3T	Burst-train, 30sec, tone task	2.5272*	Open
	3T	Burst-train, 30sec, tone task	5.2232*	Open
7B1	7T	Burst-train, 30sec	2.0684*	Closed
7B2	7T	Burst-train, 30sec	23.1090*	Closed
7B3	7T	Burst-train, 30sec	1.1595	Open
	7T	Burst-train, 30sec	1.0013	Open
7B4	7T	Burst-train, 30sec	1.2315	Open
7B5	7T	Burst-train, 30sec	1.1680	Open
	7T	Burst-train, 30sec	3.5602**	Closed
7B6	7T	Burst-train, 30sec	1.5794	Open
	7T	Burst-train, 30sec	2.7557*	Closed
	7T	Burst-train, 30sec	2.3365*	Closed
7B7	7T	Burst-train, 30sec	1.8459*	Open
	7T	Burst-train, 30sec	5.3504*	Closed
	7T	Burst-train, 30sec	5.0675*	Closed
7B8	7T	Burst-train, 30sec	1.2527	Closed
	7T	Burst-train, 30sec	1.2592	Closed
	7T	Burst-train, 30sec	1.2408	Open

Table 5.1. 40-Hz ASSR power ratio for all subjects studied. 19 of 31 runs are significant with P<0.01. * = P<0.01

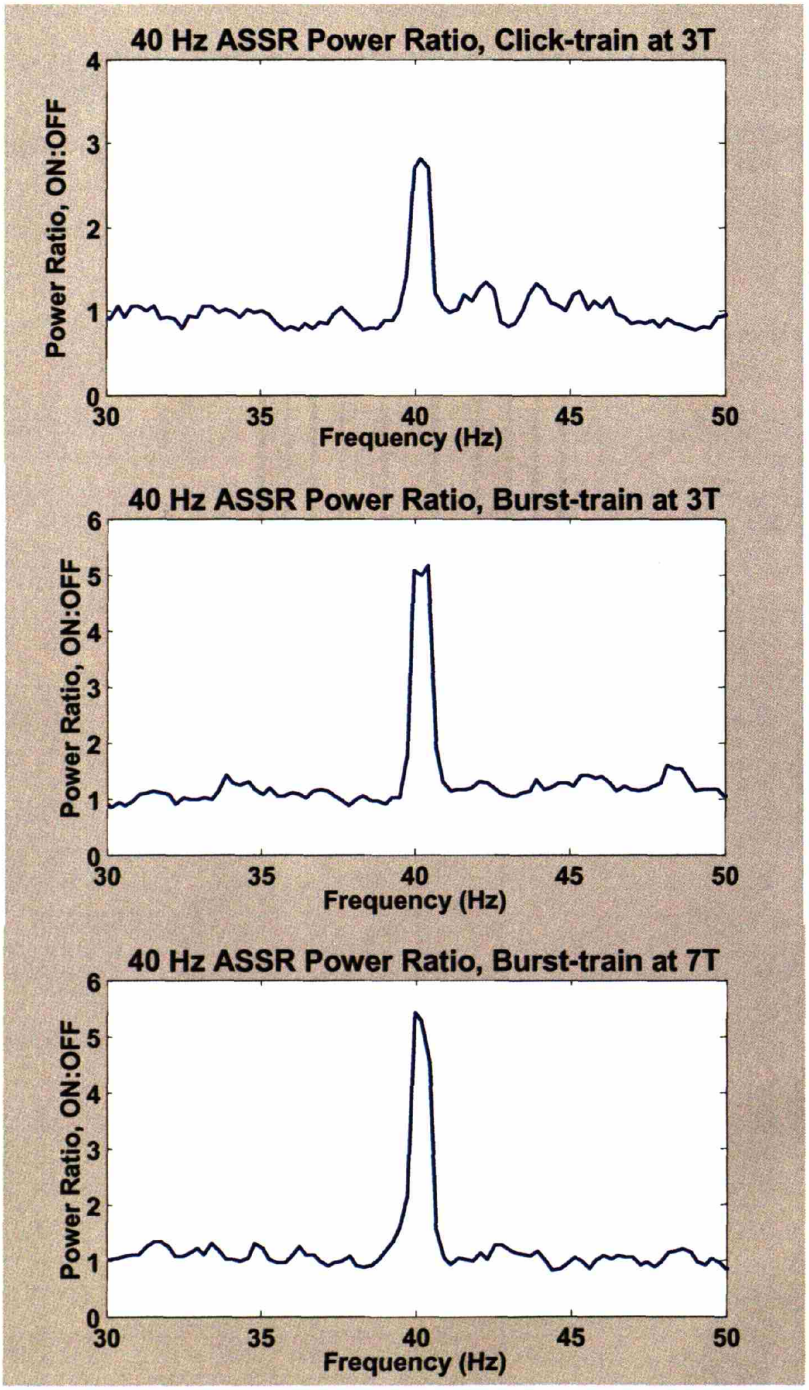

Figure 5.3. 40-Hz ASSR Power Ratios for 3T click-train, 3T burst-train, and 7T burst-train

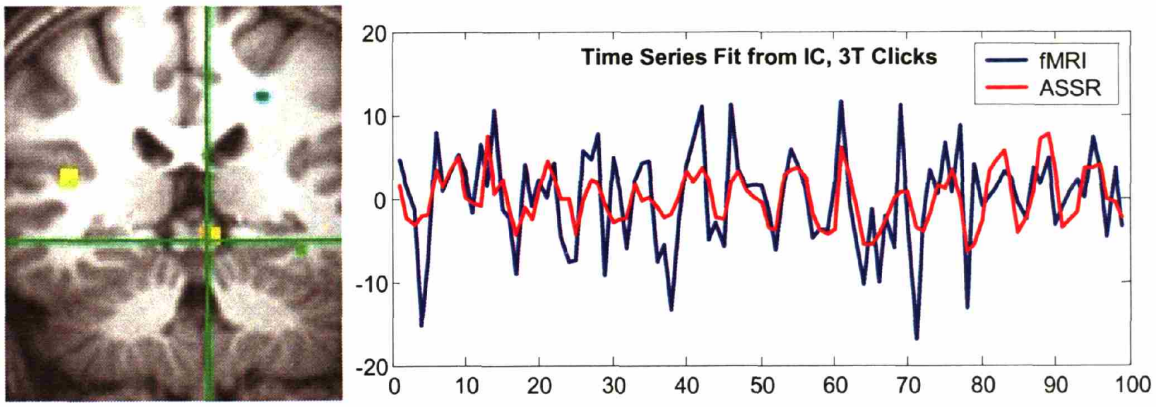

Figure 5.4. Activation map and time-series fit from inferior colliculus (IC) from 3T click-train study.

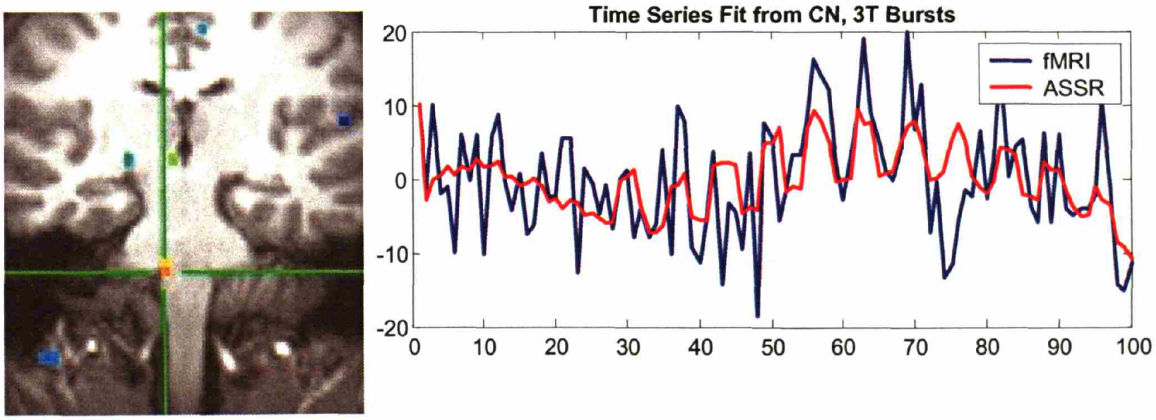

Figure 5.5. Activation map and time-series fit from cochlear nucleus (CN) from 3T burst-train study.

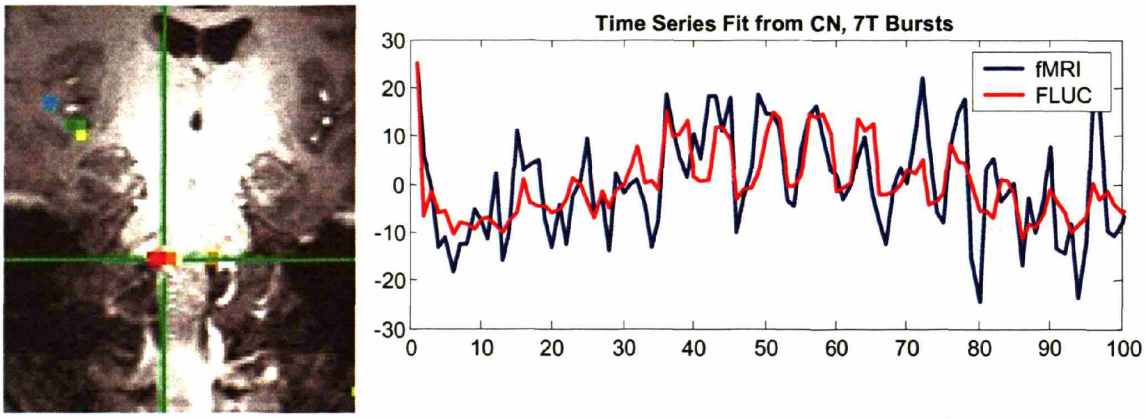

Figure 5.6. Activation map and time-series fit from cochlear nucleus (CN) from 7T burst-train study.

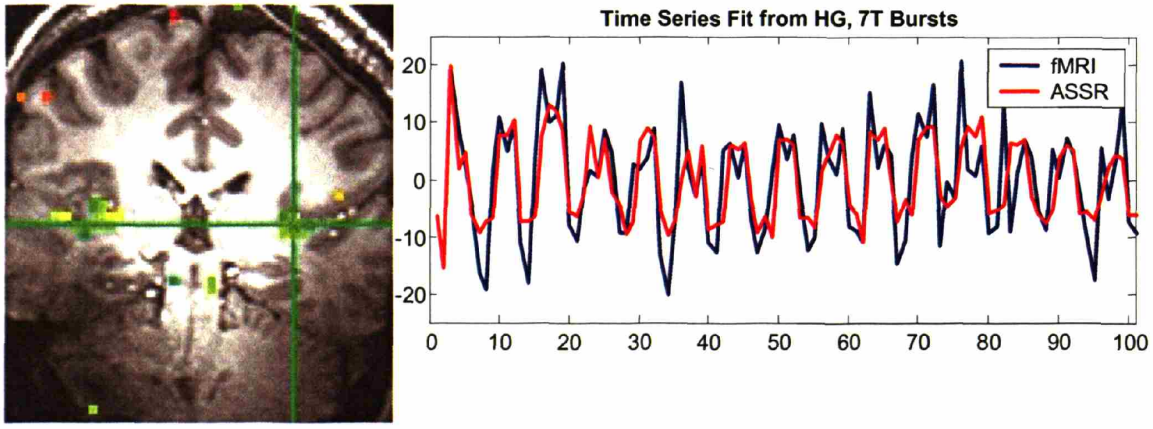

Figure 5.7. Activation map and time-series fit from Heschl's gyrus (HG) from 7T burst-train study.

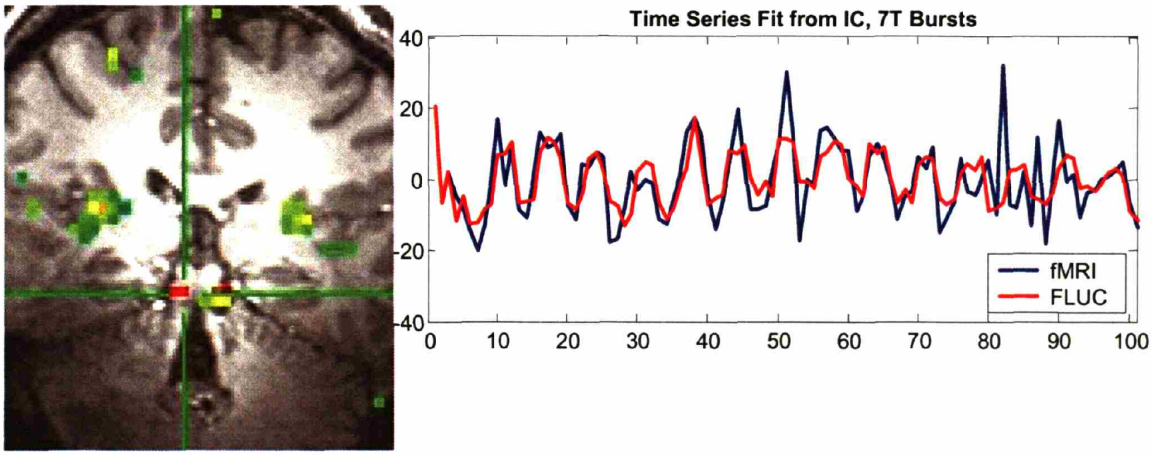

Figure 5.8. Activation map and time-series fit from inferior colliculus (IC) from 7T burst-train study.

In order to gain insight into how well these responses generalize across the whole cohort of subjects, a summary chart was constructed where cells of a table were color coded according to the presence or absence of activity within a given region for each subject (**Figure 5.9**). Significant block response activations were filled blue if active. Brain regions where the ASSR or ASSR fluctuation models were above F-value threshold and showed improved model fit relative to the block response were colored blue, while those that merely surpassed the F-value threshold were colored lavender. Inspection of this chart shows a coherent pattern of activation across subjects, including STG, HG, IC, and CN, but with little or no contribution by MGN.

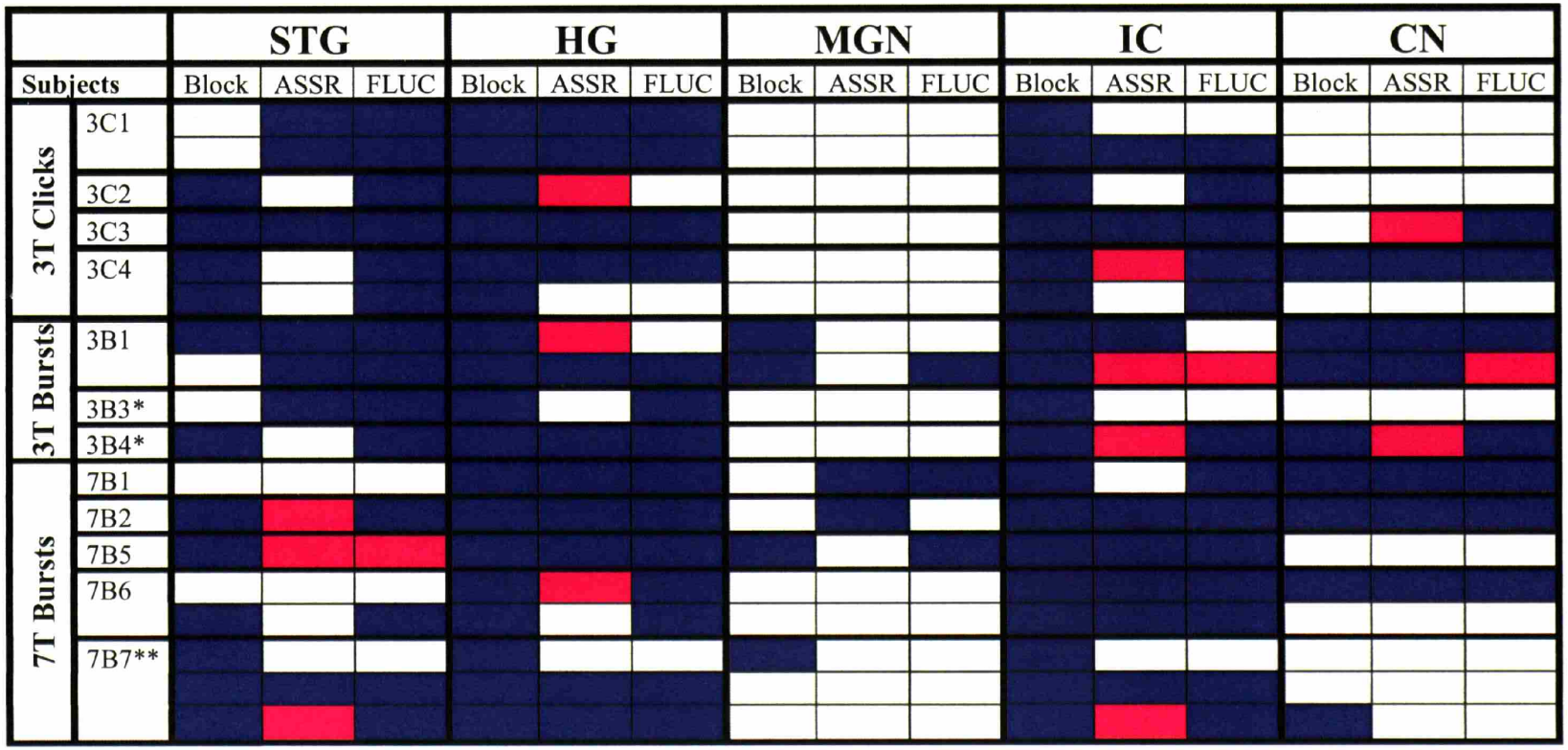

Figure 5.9. Auditory Pathway Activation Summary Across Subjects. Blue squares denote regions showing significant activation both in terms of F-test and AIC compared to block model, while lavender squares represent regions showing significant F-test results but inconclusive AIC relative to block model.

5.4. Discussion

We have demonstrated the ability to robustly record 40-Hz ASSR during simultaneous fMRI in both the 3 and 7 Tesla MRI environments, and have developed a paradigm for relating time-varying changes in the ASSR with fMRI. The simultaneous recordings of 40-Hz ASSR and fMRI described in this chapter reveal that spontaneous endogenous fluctuations in the amplitude of the 40-Hz ASSR are represented throughout the auditory system, from cortex to brainstem, suggesting that brainstem structures play an important role in generating the 40-Hz ASSR. The 40-Hz ASSR is reduced or eliminated by reductions in level of arousal (Picton et al., 2003), sleep (Cohen et al., 1991;Suzuki et al., 1994;Linden et al., 1985), and sedation or loss of consciousness under anesthesia (Plourde, 1996), but is not influenced by selective attention (Linden et al., 1987;Tiitinen et al., 1993) nor alerting nor orienting responses (Rohrbaugh et al., 1990), suggestiong that it may be a specific marker for arousal or consciousness. If the observed fluctuations in 40-Hz ASSR reflect spontaneous endogenous modulation of arousal or consciousness, these studies suggest that multiple levels of the sensory hierarchy are modulated by changes in consciousness. The involvement of auditory structures throughout the brainstem and cortex suggest that integration of sensory information across multiple hierarchical scales, including the earliest portions of the central nervous system, may constitute an important component of awareness or arousal.

Previous MEG studies attempting to localize the source of the 40-Hz ASSR have implicated cortical regions as a primary generator of this rhythm (Makela and Hari, 1987;Hari et al., 1989;Gutschalk et al., 1999). However, since these studies employed

MEG, they were limited in their ability to observe sources from deep structures, and were therefore biased towards cortically-based solutions. More recent EEG source localization studies suggest that the brainstem as well as cortical structures are involved in generating the 40-Hz response (Herdman et al., 2002), but do not identify the locus of structures involved in arousal or consciousness-related modulation of the 40-Hz response.

The EEG-fMRI recordings presented here reveal an absence of MGN involvement in arousal-related modulation of the 40-Hz ASSR. This finding is surprising given the critical role of the MGN as a sensory relay to the auditory cortex, yet is consistent with prior work in animal studies and human PET recordings. Recordings of auditory steady-state responses in rabbits analogous to the human 40-Hz ASSR comparing evoked potential latencies from depth electrodes in MGN and IC with those from surface EEG measurement suggest that IC plays a major role in generating the ASSR, while MGN does not (Hori et al., 1993). Human PET studies of the 40-Hz ASSR revealed activity in the auditory cortex and cerebellum, but not MGN. Neuro-anatomic models proposed to describe the influence of 40-Hz oscillations on cognition- and binding suggest a role for non-specific thalamic nuclei such as the intralaminar nuclei, and but do not address relay nuclei such as the MGN (Llinas and Ribary, 1993).

Neither fMRI signal-to-noise nor time-series modeling errors are likely to explain the absence of MGN activity. MGN activity is poorly observed in both 3T as well as 7T studies, where the signal-to-noise is larger by a factor of approximately 2. Un-modeled components of the BOLD stimulus response, such as the "ramp" function described in Harms, et al., (Harms and Melcher, 2003) could cause a reduction in estimation efficiency since those un-modeled components increase residual variance. Though

possible, this too is unlikely to explain the absence of MGN activity, since the ramp response is partially co-linear with the sustained block response, which would allow at least a partial representation of MGN ramp dynamics with a sustained block response alone. Furthermore, in these studies, stimulus "onset" and "offset" signal components prevalent in the STG and HG were not modeled, yet both regions possessed AIC-significant activity for ASSR and ASSR-fluctuation, despite the fact the neither the "onset" nor "offset" model components are well-approximated by the block response.

5.5. Conclusions

In this chapter we have established a simultaneous EEG-fMRI paradigm for studying the 40-Hz auditory steady-state response. We have demonstrated that time-varying ERP measurements can be made concurrently with fMRI, and that these time-varying measurements can be correlated with the fMRI BOLD signal at 3 and 7 Tesla. With this paradigm, we have shown that temporal fluctuations in the 40-Hz ASSR are represented throughout the auditory system from brainstem to cortex. If the observed fluctuations in 40-Hz ASSR reflect spontaneous modulation of arousal or consciousness, these studies suggest that multiple levels of the sensory hierarchy are modulated by changes in consciousness, and that integration of sensory information across multiple hierarchical scales, including the earliest portions of the central nervous system, may constitute an important component of awareness or arousal.

5.6. References

1. Cohen LT, Rickards FW, Clark GM (1991) A comparison of steady-state evoked potentials to modulated tones in awake and sleeping humans. J Acoust Soc Am 90: 2467-2479.

2. Goldman RI, Stern JM, Engel J, Jr., Cohen MS (2002) Simultaneous EEG and fMRI of the alpha rhythm. Neuroreport 13: 2487-2492.

3. Gutschalk A, Mase R, Roth R, Ille N, Rupp A, Hahnel S, Picton TW, Scherg M (1999) Deconvolution of 40 Hz steady-state fields reveals two overlapping source activities of the human auditory cortex. Clin Neurophysiol 110: 856-868.

4. Hall DA, Haggard MP, Akeroyd MA, Palmer AR, Summerfield AQ, Elliott MR, Gurney EM, Bowtell RW (1999) "Sparse" temporal sampling in auditory fMRI. Hum Brain Mapp 7: 213-223.

5. Hall DA, Summerfield AQ, Goncalves MS, Foster JR, Palmer AR, Bowtell RW (2000) Time-course of the auditory BOLD response to scanner noise. Magn Reson Med 43: 601-606.

6. Hari R, Hamalainen M, Joutsiniemi SL (1989) Neuromagnetic steady-state responses to auditory stimuli. J Acoust Soc Am 86: 1033-1039.

7. Harms MP, Melcher JR (2003) Detection and quantification of a wide range of fMRI temporal responses using a physiologically-motivated basis set. Hum Brain Mapp 20: 168-183.

8. Herdman AT, Lins O, Van Roon P, Stapells DR, Scherg M, Picton TW (2002) Intracerebral sources of human auditory steady-state responses. Brain Topogr 15: 69-86.

9. Hori A, Yasuhara A, Naito H, Yasuhara M (1993) Steady-state auditory evoked potentials (SSAEPs) in the rabbit. Contribution of the inferior colliculus. Electroencephalogr Clin Neurophysiol 88: 229-236.

10. Kitagawa G, Gersh W (1996) Smoothness Priors Analysis of Time Series. New York: Springer-Verlag.

11. Laufs H, Kleinschmidt A, Beyerle A, Eger E, Salek-Haddadi A, Preibisch C, Krakow K (2003a) EEG-correlated fMRI of human alpha activity. Neuroimage 19: 1463-1476.

12. Laufs H, Krakow K, Sterzer P, Eger E, Beyerle A, Salek-Haddadi A, Kleinschmidt A (2003b) Electroencephalographic signatures of attentional and cognitive default

modes in spontaneous brain activity fluctuations at rest. Proc Natl Acad Sci U S A 100: 11053-11058.

13. Linden RD, Campbell KB, Hamel G, Picton TW (1985) Human auditory steady state evoked potentials during sleep. Ear Hear 6: 167-174.

14. Linden RD, Picton TW, Hamel G, Campbell KB (1987) Human auditory steady-state evoked potentials during selective attention. Electroencephalogr Clin Neurophysiol 66: 145-159.

15. Llinas R, Ribary U (1993) Coherent 40-Hz oscillation characterizes dream state in humans. Proc Natl Acad Sci U S A 90: 2078-2081.

16. Makela JP, Hari R (1987) Evidence for cortical origin of the 40 Hz auditory evoked response in man. Electroencephalogr Clin Neurophysiol 66: 539-546.

17. Percival DB, Walden AT (1993) Spectral analysis for physical applications. New York: Cambridge University Press.

18. Picton TW, John MS, Purcell DW, Plourde G (2003) Human auditory steady-state responses: the effects of recording technique and state of arousal. Anesth Analg 97: 1396-1402.

19. Plourde G (1996) The effects of propofol on the 40-Hz auditory steady-state response and on the electroencephalogram in humans. Anesth Analg 82: 1015-1022.

20. Rohrbaugh JW, Varner JL, Paige SR, Eckardt MJ, Ellingson RJ (1990) Auditory and visual event-related perturbations in the 40 Hz auditory steady-state response. Electroencephalogr Clin Neurophysiol 76: 148-164.

21. Serafini G, Acra W, Scuteri F, Palmieri AM, Simoncelli C (1994) Auditory evoked potentials at 40 Hz (SSR40Hz) in post-trauma coma patients. Laryngoscope 104: 182-184.

22. Suzuki T, Kobayashi K, Umegaki Y (1994) Effect of natural sleep on auditory steady state responses in adult subjects with normal hearing. Audiology 33: 274-279.

23. Tiitinen H, Sinkkonen J, Reinikainen K, Alho K, Lavikainen J, Naatanen R (1993) Selective attention enhances the auditory 40-Hz transient response in humans. Nature 364: 59-60.

24. Vasios, C. E., Angelone, L. M., Purdon, P., Belliveau, J. W., and Bonmassar, G. EEG measurements at 7T Tesla using the ink cap. 13th ISMRM (submitted) . 2005.

Chapter 6
Conclusions and Directions for Future Research

6.1. Summary

In this thesis we have developed methods for multimodal neuroimaging with simultaneous EEG and high-field MRI. In Chapter 1 we analyzed the physiology and biophysics of the multimodal imaging problem to learn that simultaneous recordings of EEG and fMRI can make use of temporal correlations over a time-scale observable through fMRI to reveal dynamical networks that would be difficult or impossible to observe with EEG or MEG alone. This motivated two central issues to explore in this thesis: To develop a method for recording event-related potentials simultaneously with fMRI in a time-varying manner, and to develop methods capable of functioning at high field strengths such as 3 or 7 Tesla in order to maximize fMRI BOLD signal-to-noise. In Chapter 2 we reviewed the methodological challenges associated with simultaneous recordings, and established design goals for acquisition hardware and electrode systems that would limit EEG noise pickup, RF interference, and maximize study subject safety. In Chapter 3 we described the implementation of hardware and software systems for

EEG-fMRI data acquisition, display, and real-time signal processing. We developed a complete data acquisition system capable of recording 32 channels of EEG during fMRI with integrated external signals such as physiological monitoring and event triggers. The data acquisition software developed provides a platform for rapidly implementing real-time signal processing. We developed a novel high-fidelity auditory stimulus delivery system consisting of electrostatic headphones modified to provide up to 30dB of passive sound attenuation and electrical shielding to eliminate electromagnetic interference from the electrostatic headphone elements. In Chapter 4 we developed a method for removing ballistocardiogram artifact using adaptive noise cancellation techniques employing reference signals from a novel motion sensor system. Adaptive filter parameter estimation is accomplished with an EM algorithm that works rapidly on a short 17-second segment of baseline data. A coherence estimation algorithm based on multitaper spectral estimation is used as a diagnostic tool to select motion signals for use in adaptive filtering, and to identify badly placed or malfunctioning motion sensors prior to functional scanning. This adaptive filtering method outperforms the widely-used pulse artifact subtraction method by up to 600% and requires little or no manual intervention, performing identically well in 1.5, 3, and 7 Tesla MRI environments. In Chapter 5 we described a series of EEG-fMRI experiments designed to study spontaneous endogenous fluctuations in the 40-Hz auditory steady-state response (ASSR) by estimating the ASSR in a time-varying manner and relating ASSR time courses to fMRI BOLD signals. We demonstrated the ability to robustly record 40-Hz ASSR during simultaneous fMRI in both the 3 and 7 Tesla MRI environments. Analysis of fMRI data using 40-Hz ASSR amplitude time series as regressors revealed that spontaneous fluctuations in 40-Hz

ASSR amplitude are represented throughout the auditory system, from cortex to brainstem, suggesting that brainstem structures play an important role in generating the 40-Hz ASSR. If the observed fluctuations in 40-Hz ASSR reflect spontaneous endogenous modulation of arousal or consciousness, these studies suggest that multiple levels of the sensory hierarchy are modulated by changes in consciousness, and that integration of sensory information across multiple hierarchical scales, including the earliest portions of the central nervous system, may constitute an important component of awareness or arousal.

6.2. Directions for Future Research

The results of these studies suggest a number of avenues for future research and development. Refinements in data acquisition hardware and software can be made at many levels. If the problem of RF electrode heating is solved through the use of resistive carbon electrode and electrode lead materials, the number of EEG acquisition channels can be increased. Hardware improvements to enable rejection of gradient and RF artifacts from fully continuous EPI are a high priority. Synchronization of EEG acquisition hardware clocks to MRI hardware clocks could reduce the amplitude of gradient noise by reducing power in aliased components of the gradient waveform. Alternatively, if synchronized EEG fails to control gradient noise during continuous EPI, the EEG data can be sampled at a higher rate to reduce aliasing, and then downsampled after artifact correction. Real-time filtering and analysis modules can also be added to the existing software to add features such as real-time adaptive filtering and on-line ERP averaging.

The combined analysis of EEG and fMRI presented in Chapter 5 suggests a number of applications as well as options for improved modeling and analysis. The 40-Hz ASSR paradigm as presented in Chapter 5 could find immediate application in the study of sleep and anesthesia mechanisms, particularly since the changes in ASSR amplitude under these circumstances are very pronounced and are correlated with other behavioral and electrophysiological characteristics of sleep and anesthesia. The physiological interpretation of the ASSR fluctuations described in Chapter 5 could be greatly enhanced with concurrent estimates of alpha and beta power, which could be used to gauge the level of arousal or drowsiness. The 40-Hz ASSR is an example of a scalp potential that is correlated with a global brain state, and can be measured, as in these studies, from a single channel of EEG. Other ERP studies may require modeling and analysis that incorporates an EEG forward model in order to co-localize EEG and fMRI activity. The time-varying estimates of ASSR amplitudes performed in these studies are particularly effective because the ASSR is a periodic response that is well represented by the Fourier basis. A generalization of this for non-periodic ERPs would be to identify a basis set capable of compactly representing an ERP waveform of interest and using this basis to estimate ERP amplitudes in a time-varying manner. A time-varying analysis of non-periodic ERP/fMRI studies could find application in cognitive studies where time-varying changes in ERPs and their covarying fMRI responses could reflect learning or memory processes.